UNIVERSITA' DEGLI STUDI DI PAVIA
FACOLTA' DI SCIENZE MM.FF.NN.
DIPARTIMENTO DI FISICA NUCLEARE E TEORICA

A neutron autoradiography method to measure ^{10}B in biological samples applied to BNCT of osteosarcoma

Relatore:
Dr. Silva Bortolussi

Tesi di Laurea Magistrale di :
Ian Postuma

Anno Accademico 2010/2011

Contents

Introduction **3**

1 The Neutron Autoradiography **10**

The action of the etching . . . 14

Geometry of track development for constant V_t . . . 15

Geometry of track development for variable V_t . . . 16

Bulk etch rate and track etch rate . . . 17

1.1 Neutron autoradiography and BNCT . . . 18

2 Materials and methods **21**

CR-39 . . . 22

Thermal neutron flux measurements . . . 22

Preparation and irradiation of the samples . . . 22

Image acquisition system . . . 24

2.1 Preliminary work and analysis . . . 24

2.1.1 Image acquisition . . . 24

2.1.2 Image analysis . . . 26

2.1.3 Data analysis . . . 26

2.1.4 First conclusions . . . 27

2.2 Improvements and final set-up . . . 30

2.3 Image acquisition and analysis . . . 35

2.3.1 Repeatability check with a NIST sample . . . 37

3 Calibration of the QNCR Technique **38**

3.1 Final considerations . . . 48

4 Boron carrier analysis for BNCT **50**

4.1 Cell samples with BPA . . . 51

4.2 Cationic liposomes loaded with LCOB 52
4.3 Polymeric nanoparticles 58
4.4 Gold Nano Particles (AuNP) 59

5 Simulation with The Stopping and Range of Ions in Matter (SRIM) 62
5.1 TRIM 63
5.2 How TRIM Transports Ions in Matter 65
The Primary Stopping Number, L_0 66
The Barkas Correction, L_1 67
The Bloch Correction, L_2 69
Low Velocity Limit of the Bethe-Bloch Theory 70
Accuracy of the stopping power theory 70
The Stopping and Range in Compounds 72
5.3 The TRIM.DAT file 73
Charged particles transport in the analyzed samples 76
Comparison between tissue and liquid sample simulations. 78
5.4 Results and conclusion 81
Track etch rate V_t as a function of the Stopping Power 87

6 Conclusions 89

Bibliography 92

Acknowledgements 98

Introduction

The concept of Boron Neutron Capture Therapy (BNCT) was first introduced four years after the discovery of the neutron[1] by G.L. Locher, a biophysicist of the Franklin Institute at Pennsylvania [26]. The technique is based on the reaction ^{10}B(n,α)^{7}Li [2] which has a cross section of 3842 b at thermal neutron energies as it is shown in Figure 1.

The α particle and the recoiling ^{7}Li nucleus arisen from the capture, are high linear energy transfer (LET) particles. The range of these particles in tissue equivalent materials is shorter than 10 μm. This means that, if there is boron inside the cell, the particles produced by the neutron capture will deposit approximately all their energy inside the cell. Therefore, in order to have a therapeutic effect from BNCT, it is important to obtain a high concentration of boron inside the tumor and a much smaller one in the normal tissues. This can be achieved by using particular molecules that are able to convey boron atoms selectively in the tumor cells, exploiting active or passive absorption mechanisms. In order to assess a proper treatment plan, that is to deliver an effective irradiation with a substantial sparing of the healthy cells, it is necessary to know the boron concentration in each kind of irradiated tissue. In BNCT research many methods are used to measure boron concentration in biological samples. The most common one is Prompt Gamma Neutron Activation Analysis (PGNAA)[30, 39], a radio-analytic technique which exploits the 0.478 MeV γ ray that is emitted from the excited ^{7}Li in 93.9% of the capture reactions. With a facility dedicated to BNCT, it is usually possible to measure few ppms of ^{10}B in relatively large samples (0.5 cm^3) with irradiation times of some minutes. Anyhow, to measure low boron concentrations in small samples it is necessary to increase the measurement time. This technique is limited by the relatively high dimensions and the heterogeneity of the

[1] 1932 by J. Chadwick, Cambridge University

[2] The boron neutron capture in more detail:

$$^{10}B + n \implies \begin{cases} ^{7}\mathrm{Li} + \alpha & \mathrm{E_{Li}} = 1.01\,\mathrm{MeV};\ \mathrm{E}_\alpha = 1.78\,\mathrm{MeV}\ (6\%) \\ ^{7}\mathrm{Li}^* + \alpha + \gamma\,(0.48\,\mathrm{MeV}) & \mathrm{E_{Li}} = 0.84\,\mathrm{MeV};\ \mathrm{E}_\alpha = 1.47\,\mathrm{MeV}\ (94\%) \end{cases}$$

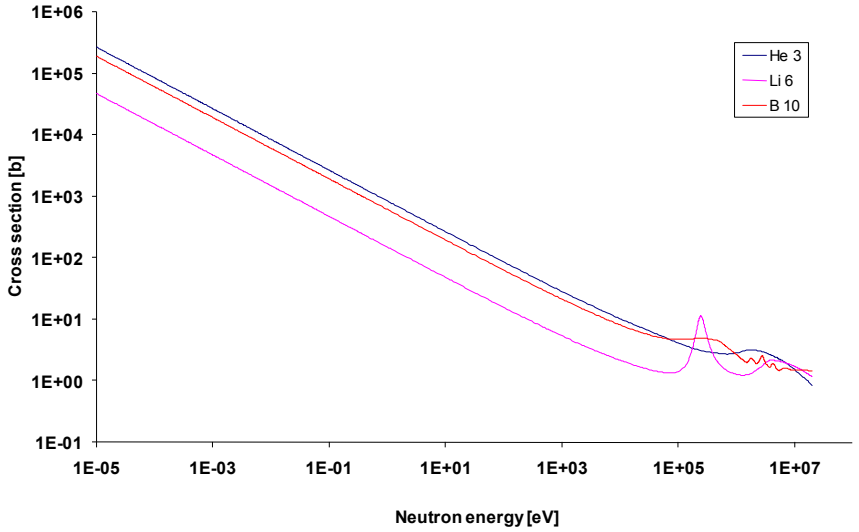

Figure 1: Neutron capture cross section of ^{3}He, ^{6}Li and ^{10}B.[48]

analyzed samples. In this case, the concentration that is obtained from the measurement procedure is an average value that cannot represent the uptake of the various cell fractions of the sample, such as viable tumor cells, healthy cells, necrosis, fibrosis and so on. The same problem is shared by other measurement methods such as ICP-AES (Inductively-Coupled Plasma-Atomic Emission Spectrometry), which allows measuring concentrations in the range 0.2–70 ng/g [36].

In brief, almost all boron analysis methods in biological samples are based on the $^{10}B(n,\alpha)^{7}Li$ nuclear reaction. Thus, alpha and lithium particles as well as the γ-rays released by the induced nuclear reaction are used for boron detection. The analysis can be done by various techniques like spectrophotometry, atomic spectrometry, radio-analytical methods and imaging techniques. In Pavia the techniques to detect boron are the Alpha Spectrometry[3] [1, 15](AS), and quantitative neutron capture radiography (QNCR). The imaging technique of QNCR is used for microscopic analysis of cell cultures and tissue cryosections. This autoradiography method detects the ionizing radiation of the boron neutron capture by registering the tracks on sensitive films. For QNCR, thin layers of cell cultures or tissue cryosections must be prepared. Then, these sections are mounted on charged particles sensitive films, irradiated in thermal neutron fluences and etched. For quantization, the tracks are scanned under a microscope and their density is related to a

[3]The Alpha Spectroscopy is a macroscopic boron measuring technique, where thin slices of tissue samples are irradiated in front of a Silicon detector that collects the charged particles produced by neutron interaction in the tissue. The spectrum is then analyzed and the boron content calculated.

calibration curve obtained by irradiating standard samples with known amounts of boron. The development of this technique will be discussed extensively in the following chapter of the thesis. One of the reasons of the implementation of QNCR in Pavia is to have an alternative to AS, that cannot be exploited to measure liquid samples because the irradiation must be performed under vacuum. Before being used as routine measurement method for all the samples, the results obtained by QNRC and AS must be accurately compared. Recently an international experiment is being performed on samples coming from CNEA, thanks to a collaboration with a group working at CAC (Centro Atomico Costituyentes, Buenos Aires) where also ICP-AES technique will be applied on the same samples. This method is based on an induced coupled plasma that produces excited ions which emit electromagnetic radiation at wavelengths characteristic of a particular element, allowing quantifying the the amount of a certain atom inside the analyzed sample.

This thesis if focused on the measurement of ^{10}B concentration in biological materials, in particular in Osteosarcoma cell samples obtained by culturing cells from UMR-106 line in presence of boronated substances. Different boron carriers were studied to test their ability to concentrate boron inside the tumor cells. Osteosarcoma is a tumor that still represents a challenge due to its high malignancy associated to the fact that it is most frequent in children and young population.

Osteosarcoma is the most frequent kind of primary bone tumor[46]. It is a malignant tumor of connective tissue within which the tumor cells produce osteoid cells. The statistical distribution of this tumor with age is roughly parallel to skeletal growth. Therefore it is most frequent in late childhood or early adolescence, reaching a peak of incidence of 25 cases per million persons at the age of 15 years[46]. On average, malignant bone tumors account for 3-5% of cancers diagnosed in children under 15 years of age[33] and 7-8% of those in adolescents aged 15-19 years in western populations[38]. Taking into account a 5-year survival rate, adolescents have a lower survival rate than children. Moreover, bones having the fastest rates of growth, such as the limbs bones, have the highest probability to be hit. When osteosarcoma appears much earlier than the second decade, or after the cessation of the skeletal growth, it is often associated with other osseous abnormalities, that can be due to genetic predisposition or can be correlated to ionizing radiation exposure[24]. Osteosarcoma is characterized by an infiltrative growth and lack of cleavage planes between healthy and neoplastic tissue. Both features act as important risk factors for local recurrence because they introduce a difficulty in the total removal of the malignancy during the surgery[16].

A common feature of osteosarcoma is the predisposition to produce variable amounts

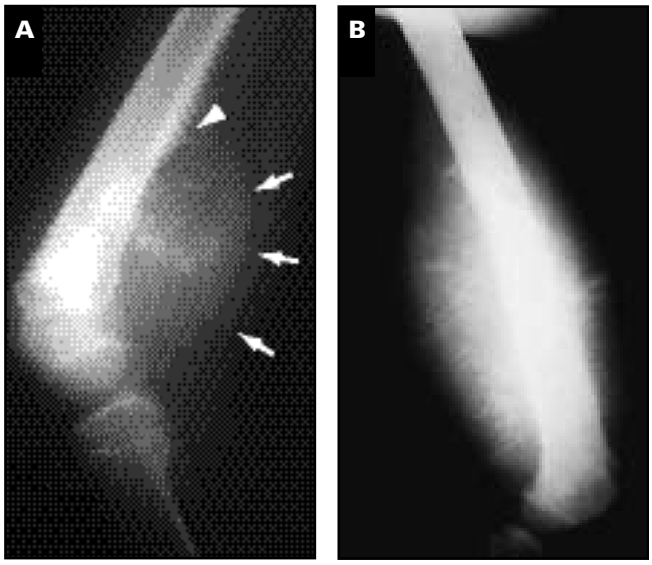

Figure 2: A, Lateral radiograph of the distal femur demonstrates typical radiographic features of osteosarcoma. Radiodense, cloudy bone lies within an ill-defined radiolucency of the femoral metadiaphysis. The arrows delimit a very large soft tissue mass containing bone matrix. B, Lateral radiograph in a different case demonstrating a very large extraosseous, radiodense mass that contains extensively interrupted periosteal "streamers," forming a "sunburst" periosteal reaction[24].

of cartilage matrix and fibrous tissue. Sometimes, the growth of the cartilage matrix and the fibrous tissue dominates the expansion of the tumor tissue. In these cases it can be a challenge to make the right diagnosis. Symptoms can vary from patient to patient, although the most frequent is pain, which can persist for weeks or months. On the other hand, the most common visible manifestation is a solid inflamed mass, that can cause the loss of function of the associated limb. Any of these symptoms should be cause of further clinical investigation. In most instances the diagnosis can be made from conventional radiographies, as shown in Figure 2.

Osteosarcoma can give rise to lung metastases, usually about 2 years after the first diagnosis, and this fact lowers sensibly the 5-years survival rate. A bad prognosis is very probable also in case of local reoccurrence of the tumor. Prior to 1970, amputation was the only surgical treatment available for osteosarcoma, and 80 % of patients died of metastatic disease mainly of the lungs [27]. These historical cases led to the conclusion that more than 80 % of patients without radiologic evidence of metastases at diagnosis had subclinical micro-metastases. This assumption was the basis for the adoption of chemotherapy protocols over the past four decades, which have led to a significant increase in the overall

survival rate [29].

With the introduction of *adjuvant chemotherapy* the 5-years survival rate was increased to 60%, although the cure rate is about 30%[34, 21, 13]. Adjuvant chemotherapy allows the neutralization of microscopic tumor masses left after the surgery, thus decreasing the probability of local recurrence or metastasis. Moreover, osteosarcoma is a radioresistant tumor and the conventional radiotherapy is used only for palliative purposes, although local irradiation with high doses in one fraction have been administered in some clinical trials [32, 47]. The result of the treatment, with chemotherapy and surgery, of non-metastatic osteosarcoma has reached a plateau. The 5 year disease free survival of $\approx 65\%$ can be expected. There is a need of new active drugs, but at the same time, different approaches to the disease have to be planned [17].

For all these reasons, there is place for a research dedicated to find and validate a new therapeutical approach to improve the clinical outcome of osteosarcoma. The selective targeting of tumor cells achievable by BNCT could be a valid option. Anyway BNCT would not be necessarily an alternative to surgery and chemotherapy, but an adjuvant treatment able to inactivate the tumor cells surviving the standard treatments and potential cause of recurrence and metastasis. Thanks to this possibility, the surgery itself may be less aggressive, with a substantial improvement of the patients quality of life.

Our expectations for the future are to improve the treatment of osteosarcoma with the alternative or integrative use of BNCT. This goal can be achieved with some adjustments in the administration ways of the boron carrier or by the use of new boronated compounds, in a way to meet the therapeutic requirements and hence offer a new curative option to a highly malignant disease.

The development of new boronated compounds effective in conveying ^{10}B atoms inside OS cells would help for the fulfillment of the objectives. It is in fact a common opinion among the BNCT scientific community that BNCT will be a routine treatment when new substances, more effective in the selective targeting of tumor cells, will be developed. To date, only two drugs have been used in clinical trials, boronphenylalanine (BPA) and sodium borocaptate (BSH).

In Figure (3) the BPA molecular structure is schematized. This drug is clinically used in BNCT since, till now, it has shown the best application characteristics[4] [4]; it is absorbed

[4]A good bornonated carrier should have the following characteristics: low toxicity for healthy tissue but high for tumor cells, an high selective absorption inside neoplastic tissue with an uniform distribution of the drug, the concentration inside the tumor mass should be $\approx$ 20-30 $\mu g/g$, the biological half-life of the drug should be short to achieve a rapid clearance from the blood and healthy tissue and as opposite the persistence inside the tumor should be long. Moreover the drug shouldn't be too hydrophobic nor too lipo-

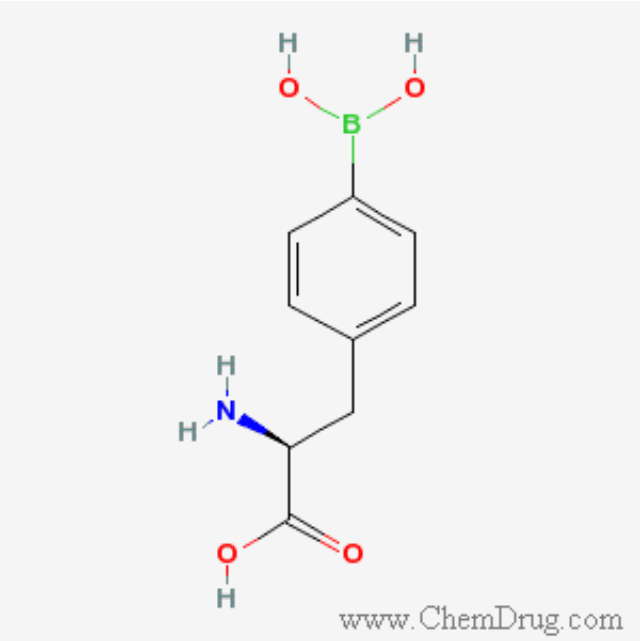

Figure 3: Molecular structure of boronphenylalanine. It's molecular structure is formed by a boron atom bound with an amino acid called phenylalanine.

by the cells through an active process and selectively internalized in tumoral cells [52]. The selectivity of BPA is one of the major advantages, since it permits to spare healthy tissue during the BNCT treatment. The uptake of BPA in the tumor is promoted by the increase of amino acid transport through the membrane of the tumoral cell. Although it is the most widely used BNCT drug [28] its major disadvantage is the low solubility in water, which is due to hydrogen bonds that tend to aggregates BPA into a crystalline structure [45]. Moreover higher concentration ratios between tumor and healthy tissue would allow shorter and more effective neutron irradiations.

The issues of finding a new drug and exploring the potentiality of BNCT for osteosarcoma are being addressed in Pavia by in-vitro and in-vivo studies. The work of this thesis was performed in the frame of a FIRB project (Futuro in Ricerca) funded by Italian Ministry of University and Research, dedicated to the feasibility study of BNCT application to limb osteosarcoma, mediated by new boron carriers developed at the University of Florence. In particular, the first measurements of boron uptake in osteosarcoma cells cultured in presence of different boronated substances were performed. The method mostly used to measure boron in tissues and cell cultures in Pavia is alpha spectrometry together with qualitative imaging by neutron autoradiography. In order to measure also liquid sam-

phobic so to facilitate the penetration inside the cellular membrane.

ples, a new quantitative technique based on neutron autoradiography was set-up. Solid-state nuclear track detector (SSNTD) called CR-39 [5] were used for this purpose. The science of SSNTD was born in 1958 when D.A. Young discovered the first tracks in a crystal of LiF [53], produced by the fission fragments of uranium that had damaged the crystal. The damaged regions are more active than the surrounding undamaged areas if exposed to a chemical attack. Therefore, by opportunely etching the SSNTD, the track dimensions in the etched material are opportunely increased and become visible. The map of the tracks is acquired by a microscope connected to a computer and the tracks are then counted using specific software.

This thesis is divided into 6 chapters: the first one is dedicated to the description of the autoradiography technique, the second to the material and methods used to achieve the optimal working conditions, while the third chapter deals with the calibration performed by standard tissue and liquid samples. In the fourth chapter the obtained calibration is then used to calculate the amount of boron in cell samples treated with different boron carriers, chapter five is dedicated to Monte Carlo calculations[6], finally in the sixth chapter conclusions and future developments are proposed. For a better comprehension of the text, it is pointed out that all the experimental values and their errors are expressed in the gaussian form : $v \pm \sigma$ where v is the mean of the gaussian distribution and σ its standard deviation.

[5] The CR-39 SSNTD was discovered by Cartwright et al.[11]. It is based on polyallyldiglycol carbonate

[6] A summary on the SRIM simulating technique can be found in Section (5.2).

Chapter 1

The Neutron Autoradiography

The neutron autoradiography is a non destructive technique that allows verifying the presence of nuclei like Li, B, N, O in samples deposited on the detector. It is also used to point out defects in materials. Our goal was to measure the concentration of ^{10}B inside samples of biological materials that can be solid (tissues or cells) or liquid (urine, blood). The neutron capture on ^{10}B produces directly ionizing particles, which are detectable by a sensitive film where the sample is directly deposited. This method is known as neutron induced autoradiography. During the irradiation, ionizing particles are produced like: photons, e^-, e^+, p, α and heavy charged ions. Hence, the film used as detector should be sensitive only to the radiation of interest.

The limit of this technique is the thickness of the sample that can be studied, which is proportional to the range of the particles that must be detected. Anyway, this can be an advantage since there is no need to use a collimated neutron beam. The thermal column of the Triga Mark II reactor is an excellent place for the autoradiography of biological samples, in fact they can be irradiated in an uniform thermal neutron field. The common neutron capture reactions and their characteristics are summarized in Table 1.1.

After the irradiation, the films must be etched in order to visualize the tracks produced by the ionizing particles in the detector. The etching parameters determine if different particles can be recognized on the basis of the dimensions of the tracks.

The autoradiography was used to analyze the concentration of ^{10}B inside the cell samples, obtained with different boron carriers. As the charged particles involved are protons, alpha and lithium ions, it was necessary to study how the tracks are formed inside the sensitive film, depending on the type of particles and on their energy as a function of the etching time. The track formation inside a SSNTD is based on the fact that heavy charged

Nuclear reactions	Cross section (barn) $E_n = 25\,meV$	Emitted particles Type	Proportion (%)	Energy (MeV)	Q Value (MeV)
$^{6}Li\ (n,\alpha)\ ^{3}H$	954	^{3}H α	100 100	2.73 2.05	4.8
$^{10}B\ (n,\alpha)\ ^{7}Li$	3842	^{7}Li α ^{7}Li α	6 6 94 94	1.78 1.01 0.84 1.47	2.8
$^{14}N\ (n,p)\ ^{14}C$	1.75	^{14}C p	100 100	0.042 0.584	0.63
$^{17}O\ (n,\alpha)\ ^{14}C$	0.23	^{14}C α	100 100	0.404 1.410	1.8

Table 1.1: Possible reactions that can be seen by the neutron capture radiography (NCR).

particles cause extensive ionization when they pass through a material [1].

An alpha particle ionizes almost all molecules close to its path. This primary ionizing process triggers a series of new chemical processes that result in the creation of free radicals and other chemical species. These species are grouped along the path of the charged particle, and this damaged zone is called a *latent track*.

If a piece of material containing latent tracks is exposed to some chemically aggressive solution, chemical reactions are more intense along the latent tracks. Aqueous solutions of NaOH or KOH are the most frequently used chemical solutions employed for this purpose. The overall effect is that the chemical solution etches the whole surface of the detector, but with a faster rate in the damaged region. In this way, a hole in correspondence of the track is formed, and it can be seen under an optical microscope. This procedure is called "detector etching" or track visualization, and the effect itself is called the "track effect". Only the dielectric materials show the track effect, since in conductors and semiconductors materials the recombination dominates and the tracks are unstable, thus preventing their clear visualization.[19].

The track effect inside a SSNTD is relatively straightforward. Even if there are many theories explaining the track formation mechanism, the damaging of the material can be basically reconstructed by describing the different stages of the particle interaction with the material. The first stage is known as "physical" phase, which lasts a few picoseconds. At this time, while slowing down, the primary ionizing particle creates ionizations and excitations close to its path. The secondary particles produced also deposit their energy and generate a series of other excitation and ionization. Some of these may go further away from the initial particle path creating the so-called delta rays. Excluding the delta rays, most ionizations and damaged molecules are created close to the particle track.

The second stage is the "chemical" phase, which lasts few microseconds. During this period of time the damaged area, where the particle has crossed the SSNTD, gets back to chemical equilibrium. The excited molecules interact to produce new chemical species, producing an inhomogeneity in the material, where the etching solution interacts in a stronger way compared to the undamaged detector areas. However, it is difficult to say which chemical species are produced and the nature of the damage is not entirely known, although some theories have been developed in order to understand these processes[3].

The track structure inside the material depends on the type of the particle and on its

[1] For example: an alpha particle with 1.5 MeV creates about 40.000 ion pairs in tissue equivalent material. Since the range of those alpha particle is about 10 μm it means that 4 ion pairs on average are created per nanometer..

energy. The only particles that can produce a track in the SSNTD are heavy charged particles, that interact mostly through the Coulomb force with the electrons of the material. The collisions with the atomic nuclei and the loss of energy through bremsstrahlung or Cherenkov radiation can be neglected. Taking into account only the interactions with the atomic electrons, it is known that for every excitation the primary particle looses on average ≈ 30 eV [31], that is 10^{-5} to 10^{-6} times the particle energy (assuming that the particle is in the MeV region). Thereafter, the slowing down of the particle can be considered as continuous, and it can be described by the stopping power $\frac{dE}{dx}$, where dE is the energy lost in the distance dx. The first expression of the stopping power was given by Bohr [7] and was a classical treatment of the particle interaction with a free electron, taking into account an impact parameter and the classical radius of the atom. Later on, the stopping power expression was modified, firstly by Bethe [5], who introduced the quantum effects, and in a second moment by Bloch, who added the relativistic effects [6]. Hence, the final well-known Bethe-Bloch expression for the stopping power was given as:

$$-\frac{dE}{dx} = \frac{Z^2 e^4}{4\pi\varepsilon_0^2 m_0 v^2} N \left[\ln \frac{2 m_0 v^2 W_{max}}{\bar{I}^2 \left(1-\beta^2\right)} - 2\beta^2 - \delta - U \right] \tag{1.0.1}$$

Where Z is the charge of the incident particle, v its velocity, $\beta = v/c$, m_0 the rest mass of the electron, N the number of electrons per unit volume, $\bar{I}$ the average excitation potential of electrons in the stopping material, W_{max} the maximal value of transferred energy of electron, δ the correction for polarization of the material and U takes into account the non-participation of inner electrons in the collision. The stopping power given in the above equation takes into account only the collisions with the electrons, neglecting the ones with the nuclei.

Although Bethe-Bloch stopping power formula is widely used, there is a strong limitation to its applicability since further corrections have to be taken into account. This aspect will be treated in Section (5.2). One of the most important corrections must be made at low energies, where the ion can capture electrons from the material, therefore changing the amount of energy deposited per unit path. This event can be considered in the Bethe-Bloch equation by introducing an effective charge Z_{eff}. This is not the real charge Z_1 of the particle, since it can assume non integer values, but it represents the mean charge that a bunch of particles have at a certain energy. By means of the effective charge, the stopping power theory can be better fitted to the experimental values[23].

Nowadays,softwares are available for the calculation of the stopping power and the range of charged particles in different media. One of the most widely used is SRIM (Stop-

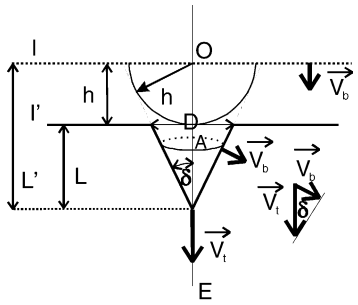

Figure 1.1: Geometry of the track development. The incident angle is normal with respect to the detector surface, and V_t is constant.

ping and Range of Ions in Matter), a Monte Carlo transport code developed by Ziegler et al. [55].

The action of the etching

As previously stated, the detectable particles are the heavy charged particles, that have straight line trajectories inside the matter, since the most probable interaction is with the atomic electrons. Thus, the etching of the SSNTD can be described considering that the damage occurs along a straight line. To date, there are many theories that describe the physical aspect of the track formation. However, none of them manages to explain exhaustively the track formation in a way to classify different particles with parameters connected to the damage of the SSNTD. The problem of the track development during the etching will be thus treated in its geometrical aspects.

Starting the geometrical description from the easiest case, the incident particle is assumed to enter under normal incidence with respect to the detector surface, as shown in Figure (1.1). In this figure, I is the initial detector surface, I' is the surface after the etching, V_t is the etch rate along the particle trajectory (track etch rate), V_b is the etch rate of the undamaged regions of the detector (bulk etch rate), O is the entrance point and E is the end point of a particle in the detector material, and $OE = R$ is the particle range in the detector material. The distance between I and I' is equal to h, i.e., the thickness of the layer removed by etching, L' is the total distance traveled by the etching solution along the particle track, and L is the track depth.

The track development is characterized by two parameters: the bulk etch rate V_b and the track etch rate V_t. These quantities describe the development of the etching during a period of time t. It can be assumed that tracks development is analogous to wave propa-

gation. Just as Huygen's principle, stating that each point in the wave front is the source of a new spherical wave, each point on the surface of the detector can be assumed to generate an "etching" front with radius $h = V_b \cdot t$. This happens all over the surface, except in the direction of the particle path, where the etching progresses with the rate V_t. Moreover, the track develops only when the ratio V=V_t / V_b is higher than 1. This follows from the fact that the etch rate of the undamaged material should be less than the etch rate along the track of the particle. As shown in Figure 1.1 the local development angle δ can be defined as:

$$\sin\delta = \frac{1}{V} \tag{1.0.2}$$

where the track develops forming a cone. The wall of the cone will expand with the same etching rate of the bulk, in the direction parallel to the wall surface.

Geometry of track development for constant V_t

Recalling Figure (1.1) and the analogy between track development and wave propagation, according to the Huygen's principle, the track development for normal incidence can be considered in two dimensions, where the track depth L is given by:

$$L = (V_t - V_b)\, t \tag{1.0.3}$$

where t is the etching time. Moreover, it can be seen that:

$$\tan\delta = \frac{D}{2L} = \frac{h}{\sqrt{L'^2 - h^2}} \tag{1.0.4}$$

by combining the previous equations, the diameter of the track opening is given:

$$D = 2h\sqrt{\frac{V-1}{V+1}} \tag{1.0.5}$$

If $V \gg 1$, from the previous equations :

$$D \cong 2h \tag{1.0.6}$$

Based on EQ. (1.0.6), an indirect method for bulk etch rate measurements was developed. If the track etch rate is very large, which is the case when heavy ions or fission products are used for the irradiation, the removed layer is directly related to the track-opening diameter

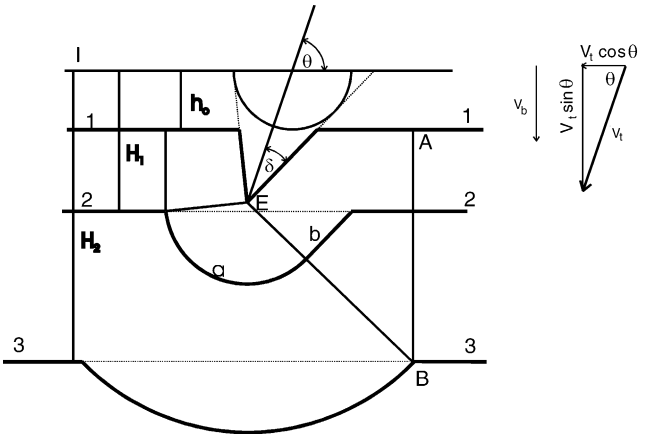

Figure 1.2: Phases of track development for oblique incidence.

which is easily measurable. Since $h = V_b t$, it is easy to calculate V_b.

Once the etchant has reached the end of the track, point E in Figure (1.1), the etching progresses in all directions with the same rate V_b, and the corresponding track becomes "over-etched". A sphere is now formed around the point E, and the shape of the track becomes a cone jointed with a sphere. With prolonged etching, the spherical part is enlarged and the conical part becomes smaller and smaller. Finally, if the etching lasts sufficiently long, the whole track will become spherical. The contrast of a spherical track is lost and the track might be seen with difficulties or might even become invisible.

In the cases studied in this thesis, normal incidence is not a real condition, the particles generated during the neutron irradiation of the sample are uniformly distributed on the entire solid angle. In these conditions the track opening becomes elliptical. The ellipse is characterized by its major axis D and its minor axis d. These two parameters are important characteristics of a track opening for oblique incidence. If the track is over- etched, the post-etching surface might cut both the elliptical and spherical parts of the track wall. In this case, the track-opening contour is a complex curve that consists of an ellipse and a circle jointed at some points. With prolonged etching, the spherical part of the track wall, and thus the circular part of the track opening, are enlarged. Finally, the track becomes totally spherical and the opening becomes completely circular.

Geometry of track development for variable V_t

In the previous section the theoretical approach of track growth for a constant V_t was considered. In the real case V_t is variable in most cases, thus the track wall cannot be de-

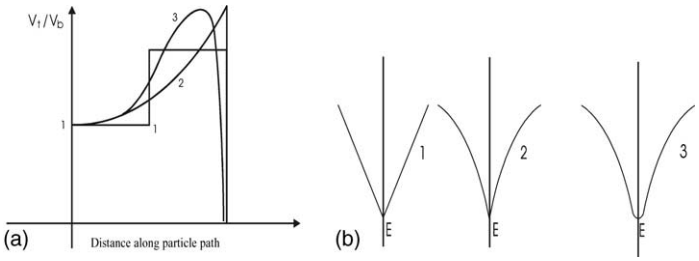

Figure 1.3: (a)Variation of the V_t function along the particle path: (1) $V_t = constant$;(2) V_t is variable with maximum at the end of the particle path; (3) V_t is variable with the maximum before the end of particle path (this is the realistic situation). (b) Track profiles for the cases (1), (2) and (3), respectively.

scribed as a regular cone anymore, and the track is now a semi-conical surface as shown in Figure (1.3). The cross-section between the post-etching detector surface and the track is now more complex than a simple ellipse, depending on the removed layer, the range of the particles and V_t. The description of this situation is beyond the purpose of this thesis, a deepening of these concepts can be found in the article by Nikezic et al. [31].

Bulk etch rate and track etch rate

The bulk etch rate V_b is the rate at which the undamaged surface of the detector is removed by the etching. Due to the chemical reaction between the etching solution (etchant) and the detector material, some molecules of the detectors are removed even if there is no track. The final effect is the removal of a layer of material from the detector surface.

For the CR-39 films used in this work, the V_b measurement, was done by irradiation with a ^{252}Cf source at a short distance and etched for the following times: 30, 45, 60, 70 and 80 min, in a 6.25 N NaOH solution at 70 °C [2]. The etching solution was prepared mixing 99.0 % purity NaOH with pure water. After etching, CR-39 films were washed out with cold water in order to remove the etchant solution from the detector surface. Finally the tracks were analyzed and V_b were determined by Eq. (1.0.6). The complete analysis and results have been published in the article by Gadan et al. [20]. The results showed that, the track diameter increased with the etching time for the whole considered time range, and a linear response with a constant bulk etch rate of $V_b = (1.64 \pm 0.02)\mu$m/h was obtained.

[2]This characterization was performed by Ing. M.A. Gadan (CNEA, Argentina) during his research period in Pavia.

The track etch rate V_t is the rate of detector etching along the particle track. For normal incidence a track is formed when $V_t > V_b$ although for an oblique incidence of the particle, a track is formed when $\cos\theta > V_b/V_t$, where θ is the angle between the track and the normal to the detector surface. For this thesis V_t was not calculated, since there are different particles interacting with the SSNTD, having their own V_t depending on their linear energy deposition in the CR-39. For our purposes it is sufficient to know that the V_t depends on the energy deposition of the ionizing particle, therefore from Eq. (1.0.5) the diameter of the tracks depends from the energy deposition of the ionizing particle.

1.1 Neutron autoradiography and BNCT

The autoradiography can be very useful in BNCT, since it allows visualizing the distribution of the boron concentration inside the samples. Although the process of image development and data acquisition can be time consuming, there is the advantage of measuring concentrations of the order of a few $\frac{\mu g}{g}$. Another benefit is the low cost of the process compared to other techniques like prompt gamma neutron activation analysis or ICP. This is due to the low cost of the CR-39 sensitive film and the possibility of irradiating a number of samples in short irradiation times (at least in facilities like the thermal column of TRIGA reactors, as the one at the University of Pavia).

In Pavia, this technique was exploited as a method for qualitative imaging of the boron biodistribution in tissues [42, 1]. The irradiation and the etching parameters were set as to obtain darker areas due to higher track density in correspondence of higher boron concentration zones. The obtained images were compared with histological preparations of tissue sections contiguous to the ones used for autoradiographies. In this way it was possible to verify if the tumor nodules visible in the histological glass matched with the darkest zone in the autoradiography images. It was a qualitative way to demonstrate the selective uptake of boron in tissues.

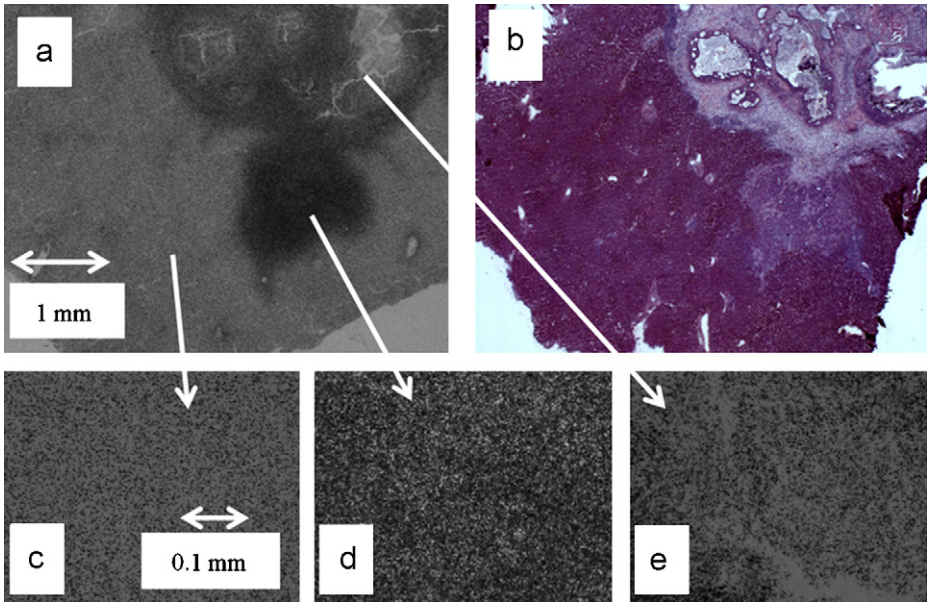

Figure 1.4: Comparison between two images of a sample coming from a tumor nodule of first patient treated by the TAOrMINA method: (a) neutron radiography and (b) histological image. In the neutron radiography the boron distribution seems to be rather uniform in the healthy tissue (c), and quite irregular in the tumor area. (d), (e). In (d) darker zones correspond to an almost 100% presence of tumor cells, and in (e) lighter areas are filled with necrotic cells or with the tumor disseminated through healthy hepatocytes.

Recently, this technique was exploited to set-up and calibrate a quantitative measurement of boron concentration, irradiating and etching the detectors in a way that the tracks remain separated and countable. The first part of this thesis work was dedicated to a study of the best parameters for the irradiation and the etching in order to reach the best working conditions for both in liquid and solid samples. An example of neutron autoradiography for boron quantification is shown in Figure 1.5.

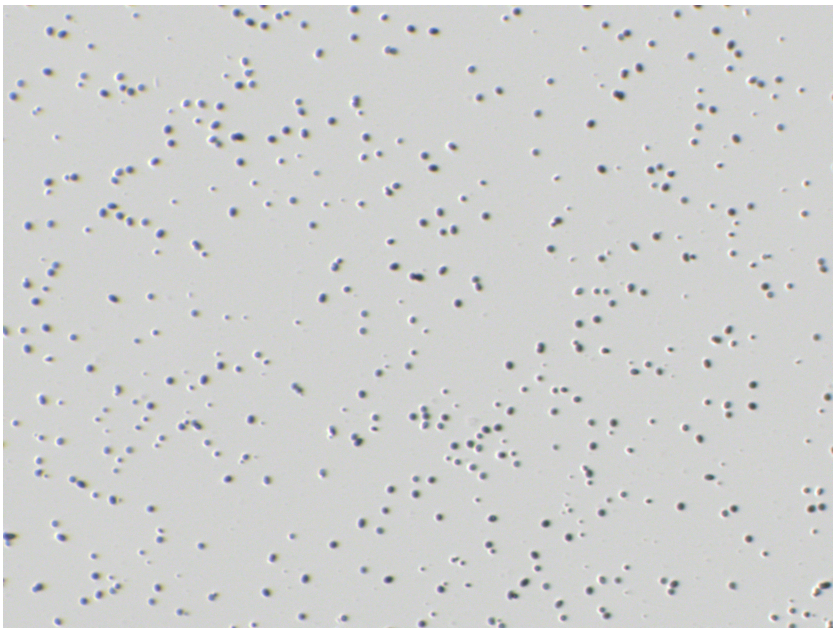

Figure 1.5: This image is an example of the tracks that form from the irradiation of a 30ppm tissue standard on a CR-39 SSNTD. The picture represents an area of 0.2961 mm^2.

Chapter 2

Materials and methods

For boron measurement by neutron autoradiography a calibration curve expressing the track density as a function of boron concentration must be assessed. The track density obtained for the samples can then be directly compared with the curve. The first step was to perform measurements using tissue and liquid standards with known boron concentration in order to obtain two calibration curves, expressed as density of tracks [$tracks/mm^2$] versus boron concentration in ppms. Standard liquid and tissue samples with known boron concentration are used as reference.

It is very important to note that it is necessary to obtain proper calibration curves for each kind of sample that must be measured. In fact, the stopping power of the charged particles depends on the material that they cross. For this reason, the calibration for solid biological tissues was performed using liver tissue reduced to a cell suspension. In this way, the track density obtained by irradiation of a tissue section, can be related to this calibration curve, because the stopping power of alpha particles is the same. Therefore, it is important to use tissue calibration when measuring tissues, water solution calibrations when measuring liquids, and so on. Another characteristics of standard samples should be an easy and reproducible preparation. The tissue standards were obtained from a mixture of cells and a solution of BPA fructose in different fixed proportions. The liquid standards are solutions of distilled water with boric acid. These standards are homogeneous to the biological samples that must be measured for BNCT research: aqueous solutions containing new boronated formulations for the quantification of boron in the molecules, biological liquids as urine, dry cell samples and sections of tissues.

The preliminary results obtained using these standards were published in January 2012 [20]. Afterwards, new efforts were devoted to improve the quality of the analysis and to in-

crease the accuracy of the results. In the following sections the first calibrations obtained will be described, then, an account of the evolution of the system, both from the instrumental point of view and concerning the setting of the parameters will be presented.

CR-39

The sensitive films used for neutron autoradiography were rectangular polyallyldiglycol carbonate (PADC) CR-39 film detectors from Intercast Europe manufacturer, with a 75 × 25 mm^2 area and a 1 mm thickness. As discussed in the previous chapter, a critical parameter for the image development is the bulk etch rate, that was previously characterized by irradiation with fission fragments and etching in a 6.25 N NaOH solution at 70 °C [20].

Thermal neutron flux measurements

Before the irradiation of the standard samples, in order to characterize the two irradiation positions for liquid and solid samples, the thermal neutron flux was measured, by means of copper foil activation. For the liquid samples, copper foils were positioned inside four holes, for each CR-39 position, filled with water and irradiated in the same position as for the real measurements. After irradiation, the foils were taken off the facility and their activity was measured by a germanium detector. The neutron flux determination for the tissue samples, was carried out using the same method as for liquid irradiation facility, by positioning copper foils in representative points of the CR-39 irradiation facility. The thermal neutron flux measured in the liquid irradiation facility with the reactor operating at 250 kW was $(7.2 \pm 0.3) \times 10^8$ n/cm^2·s. The thermal neutron flux measured in the solid sample irradiation facility with the reactor operating at 250kW was $(1.37 \pm 0.08) \times 10^9$ n/cm^2·s. From these results, the neutron flux was renormalized at the different reactor powers as it is stated in Table (2.1).

Preparation and irradiation of the samples

The liquid standards consisted of water solutions of ^{10}B at 5, 10, 20, 25, 50 and 100 ppm. About 1 ml of each solution was poured on CR-39 films, using the device constructed on purpose for the irradiation of liquid samples (see Figure 2.1), that allows irradiating 4 films a time with 4 samples each. The device with the liquid samples was irradiated at the end of the thermal column of the TRIGA Mark II reactor, operating at 10 kW for 30 min, receiving a neutron fluence of $(5.2 \pm 0.2)\ 10^{10}\ n/cm^2$ [20].

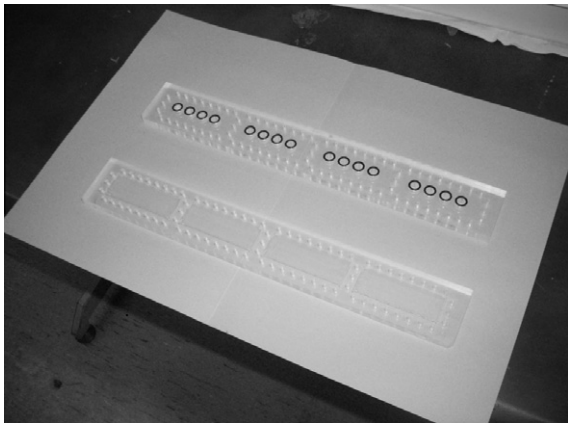

Figure 2.1: Liquid samples irradiation facility. This facility allowed pouring 1 ml of solution in sealed holes below which CR-39 films were positioned. This device hosted four CR-39 films, and for each film four holes for liquid samples were available. In this way it was possible to obtain films in which up to four different concentrations were simultaneously present.

The solid samples for the tissue calibration were obtained mixing a cell suspensions of rat healthy liver with BPA-HCl, at different boron concentrations. Briefly, cell suspensions were obtained by mechanically treating the liver tissue with a potter homogenizer. The tissue inserted into the tube was pressed until its complete disaggregation. Then the obtained cell suspensions were divided into five aliquots, centrifuged to eliminate the water excess, and weighted. A boronophenylalanine–HCl (BPA–HCl) solution at 500 ppm of ^{10}B was added to each cell fraction in order to obtain the reference boron concentrations of 5, 10, 25 and 50 ppm. The concentration values were then recalculated on the basis of the true weights of each prepared sample; the error associated to the concentration values is of the order of 0.5%. Finally, the samples were frozen in small cylindrical rods at -80 °C. Slices of 60 μm were obtained using a Leica cryostat and were deposited on CR-39 films, which were then irradiated at the end of the thermal column with the reactor operating at 1 kW for 30 min [1], receiving a neutron fluence of (0.98 ± 0.06) 10^{10} n/cm^2[20]. The solid biological samples were irradiated in a facility made up of two plexiglass slides positioned vertically at the end of the thermal column. This facility allows the irradiation of up to thirty CR-39 films positioned at different heights at the same distance from the reactor core[2].

[1]The initial irradiation was performed with a reactor power of 5 kW. But, due to the fact that it was necessary to increase the etching time to enlarge the tracks size, the power was successively reduced to 1 kW to prevent tracks overlap.

[2]The thermal neutron flux is almost homogeneous in the vertical and transversal directions at a fixed

Sample	Power (kW)	irradiation time (min)	Fluence (n/cm^2)	etching time (min)
Liquid	10	30	$(5.2 \pm 0.2)\ 10^{10}$	45
Tissue	5	30	$(4.9 \pm 0.3)\ 10^{10}$	45

Table 2.1: Starting working conditions.

Image acquisition system

The experimental set up for the Image acquisition is composed by a *microscope* [3] connected to a *lamp* [4] and a *joystick* [5]. The microscope has an integrated camera connected to a PC and, initially, the program LAS (Leica Image Acquisition) V3.7 was used to acquire the pictures. As it will be described in the next chapters, a new program called Image Pro Plus 7.0 has been selected to acquire images, this helped to improve the acquisition and analysis method.

2.1 Preliminary work and analysis

The preliminary step was to demonstrate the possibility to obtain a proper calibration to measure the quantity of boron inside liquid or tissue samples. The initial conditions of irradiation and etching are listed in Table 2.1. After the irradiation and the etching, the procedure consisted of 3 steps: *image acquisition*, *image analysis* and *data analysis*. Each step will be described in the relative section.

2.1.1 Image acquisition

The maximum possible zoom, corresponding to a picture of 0.2961 mm^2 area was set. As a consequence, the lamp was set to the maximum luminosity, to keep a high contrast between the background and the interesting points in the picture. With the same criterium, the indicated values of *exposure, gain, gamma* and *sharpness adjustment* were selected. A *shadow correction* (corresponding to a background subtraction) was applied since there was a inhomogeneous light field altering the quality of the picture.

distance from the core [43].

[3] microscope : LEICA MZ16A

[4] lamp : LEICA CLS150X

[5] joystick : PRIOR OPTISCAN II

Name	Characteristics	Picture
Microscope	Lens zoom 1.0x Digital zoom 115.0x	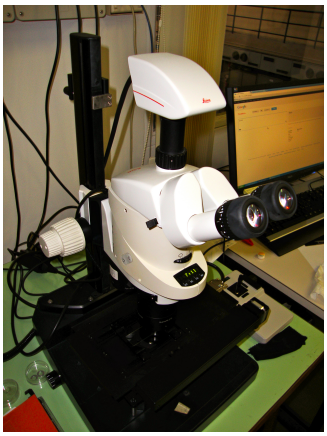
Lamp	Luminosity 6 (max) Filter 6 (no filter	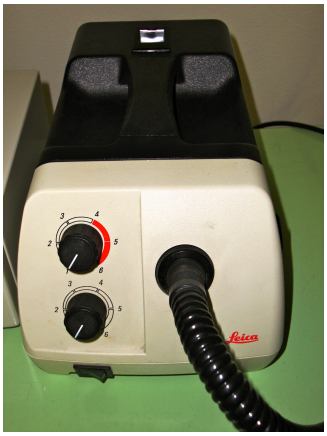
Acquisition program	Exposure 17.6 ms Gain 1 Gamma 0.54 Shadow correction on Sharpness adjustment robust	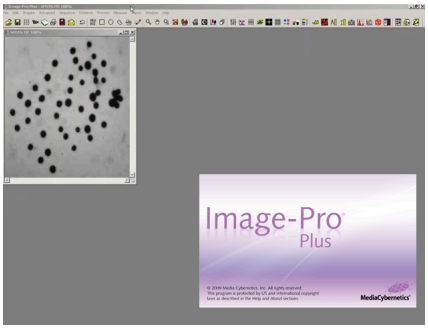

Table 2.2: Instrument setup.The specified parameters were optimized for a good definition of the tracks in the pictures.

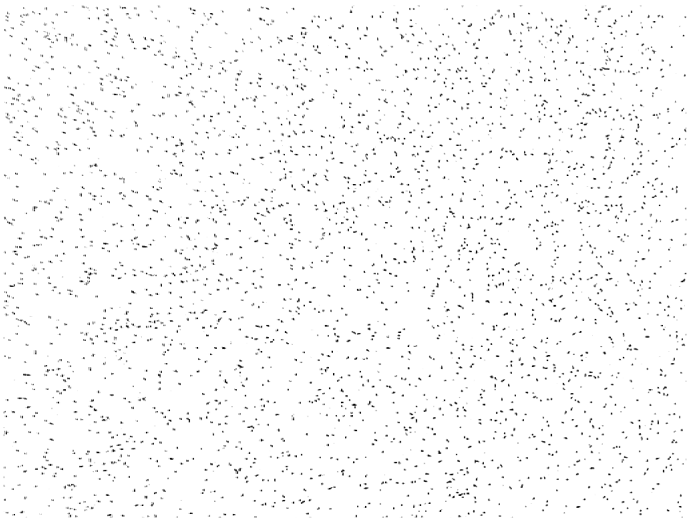

Figure 2.2: Picture sample of a tissue with 50ppm of ^{10}B.

2.1.2 Image analysis

Once the images had been acquired, the program *Image-Pro analyzer 6.3* was used to classify the objects (the dark points visible in Picture (2.2)). The analysis process started with the binarization of the images using the gray scale histogram. Once all the interesting points were set to black and the background to white, a built-in code was used to count the number of black objects. Moreover, for each object, the program calculated some user-defined parameters: in our case, the *minimum diameter* [6] and the *area* [7] were used to characterize and select the interesting points to count. For the area, a threshold was imposed equal to 1 pixel: this means that the objects with area smaller than the threshold, clearly due to dirt or artifact left in the background after the binarization, were removed from the count. Another threshold for objects too large was imposed, that could be caused again by dirt or to CR39 irregularities. Although they are rare, in comparison to the small objects in the background, it is important not to count them. The minimum diameter was used as a trigger for the counting system, as explained in the next section.

2.1.3 Data analysis

Eventually, the data obtained from Image-Pro analyzer 6.3 were analyzed, using the ROOT framework [37] to plot and fit the data. The first step was to select the range of minimum

[6] Length of shortest line joining two points of an object's outline and passing throught the centroid.
[7] Area of the outlined object.

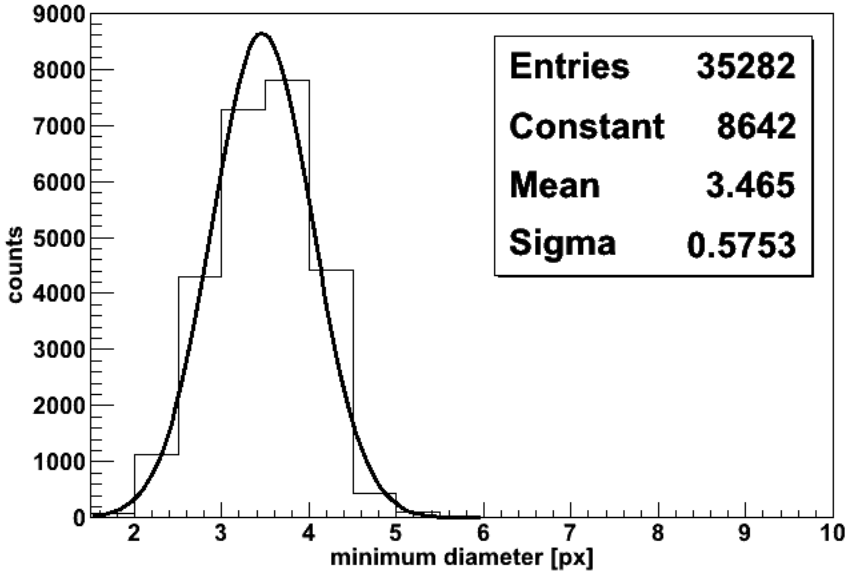

Figure 2.3: Histogram of the minimum diameters of the objects of all the images collected for one particular sample.

diameters of interest. To do this, the minimum diameters were plot as an histogram, using the objects of all the pictures of a certain sample (Figure (2.3)).

The distribution of the minimum diameters has a gaussian shape, and a gaussian fit was applied to select a *range* of minimum diameters to be $[\mu - 3\sigma\,,\,\mu + 3\sigma]$ [8] , assuming that all those objects correspond to α particles.

The number of α particles in that range was thus counted in each picture, and used to build another histogram, as the one in Figure (2.4), from which the mean number of objects per picture (that is, the mean track density at a given concentration value) and its associated error were obtained. Finally, the mean track density was plotted against the concentration values and the calibration curve was obtained both for liquid and for tissue standards, as shown in Figure (2.5) for the liquid and in Figure (2.6) for the tissue.

2.1.4 First conclusions

The calibrations obtained show a good linearity, that would allow boron measurement in samples analogous to the standard employed. The slope error, for both liquid and tissue samples, is about 10%, which is quite high. Anyway, this first analysis taking into account

[8] Where μ represents the medium value of the gaussian fit while σ is the standard deviation of the fit.

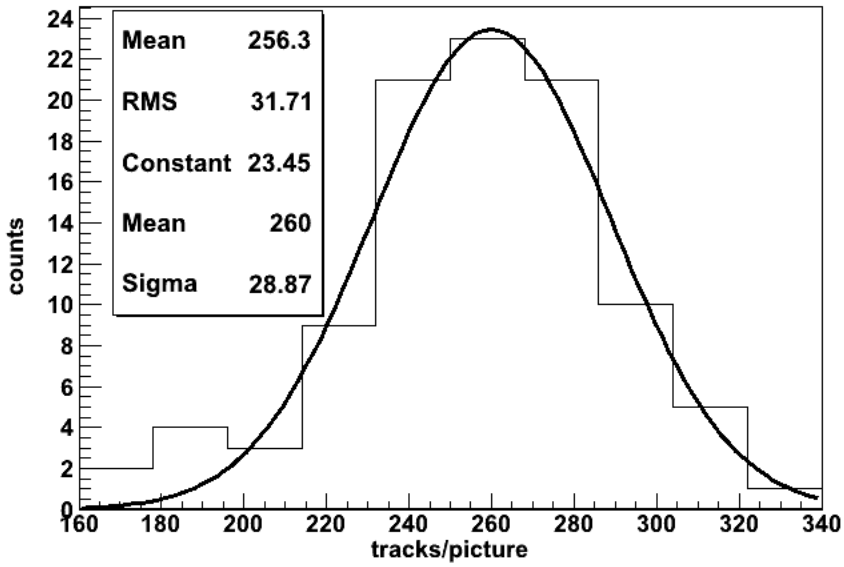

Figure 2.4: Histogram of the number of objects per picture with minimum diameter in the selected range of minimum diameter.

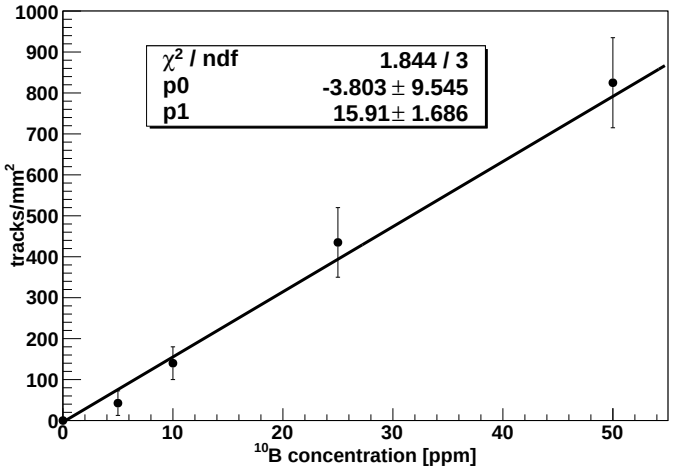

Figure 2.5: Calibration curve for the liquid sample. Where p0 represents the y-intercept of the line, while p1 is the slope.

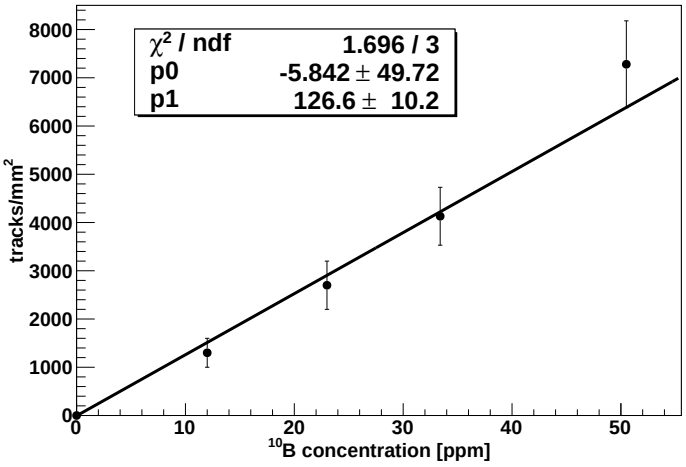

Figure 2.6: Calibration curve for the Tissue sample.Where p0 represents the y-intercept of the line, while p1 is the slope.

only two parameters (area and minimum diameter of the tracks), provides a quite reliable measurement method.

A further consideration must be made, considering the dry to fresh mass ratio of the samples. The tissue sections, in fact, lose their water content soon after the cut. Tissues different than the calibration samples, although with similar composition, could lose water in different percentages. Therefore, when calculating boron concentration in a sample by comparison with the calibration curve, the results must be renormalized by the ratio between the water loss in the calibration samples and in the actual sample. Our tissue samples have a dry to fresh mass ratio of 0.15 ± 0.01 measured using a high precision scale [20]. The dry to fresh mass ratio can also be calculated by the ratio between the tissue slope and liquid slope, since the stopping power in water and dry tissue is very similar. Taking also into account the difference in fluence, from the calibration curves that we obtained the slope ratio is 0.133 ± 0.017, in good agreement with the measured value: this is another hint that this first method was correct for ^{10}B concentration measurement.

However, the study of the set-up was further deepened, in order to decrease the error on the slope, and thus to improve the precision of the measurements. Moreover, the goal was to determine a better trigger on the tracks shape and area for the image analysis, in order to recognize the different particles interacting with the SSNTD. Another disadvantage of the described measurement conditions is that, with an etching time of 45 minutes, the inhomogeneity of the CR39 is still visible and appears as dark objects on the pictures

Figure 2.7: An example picture with dark objects in the background.

(see Figure 2.7). This factor can sensibly alter the image analysis and thus the result of the measurement.

2.2 Improvements and final set-up

In order to accomplish the requirements listed in section (2.1), the tracks on the pictures had to be better characterized. 45 minutes of etching were not enough to identify and separate tracks generated by different particles, since the morphological parameters of the analyzed object were below the limit resolution of the instrument. Hence, the first step was to find an etching time that would sufficiently expand the tracks. In this way, new characterizing parameters could be introduced. To monitor the evolution of the tracks on the SSNTD, pictures of a portion of detector were taken at different etching times. Some of those pictures can be seen in Figure 2.8, Figure 2.9 and Figure 2.10.

The first aspect to be noted is that the tracks enlarge with increasing etching time as expected. In a second instance, focusing on the difference between large and small tracks, two well defined populations of tracks appear on the CR39 as the etching time increases. Another important feature is that the tracks tend to assume a circular shape. This shape can become a trigger to select only single tracks thus improving the track selection in a way that anomalous artificial objects are left out the counting mechanism. Last but not

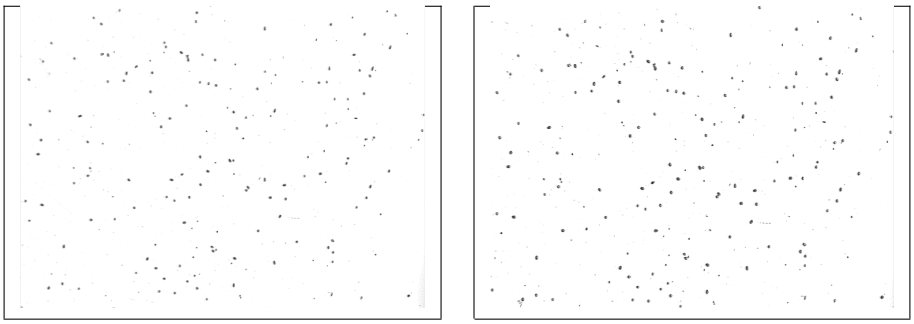

a) b)

Figure 2.8: Picture a) has been taken at 90 minutes of etching, while picture b) has been taken at 120 minutes.

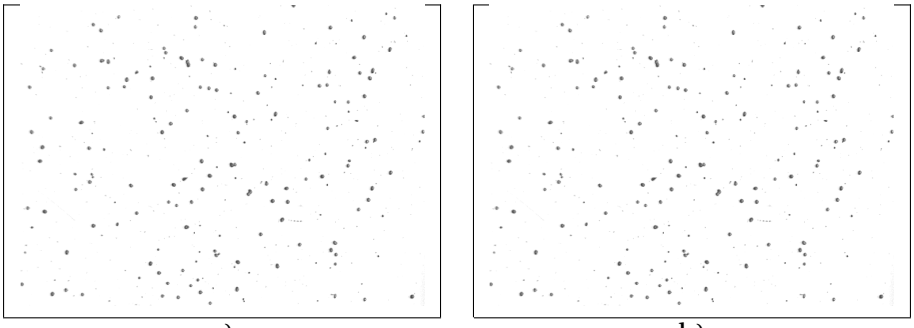

a) b)

Figure 2.9: Picture a) has been taken at 150 minutes of etching, while picture b) has been taken at 180 minutes.

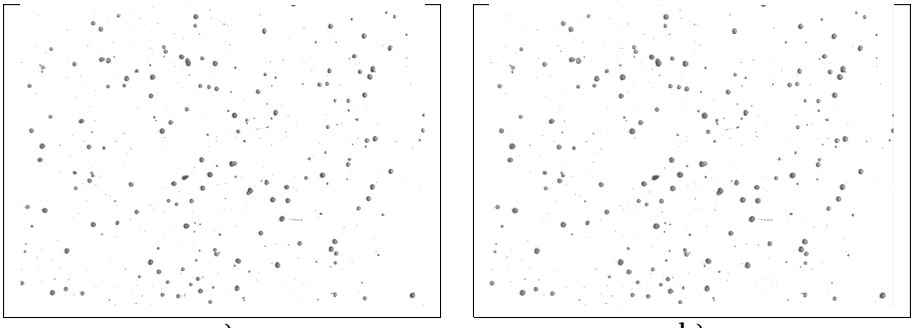

a) b)

Figure 2.10: Picture a) has been taken at 210 minutes of etching, while picture b) has been taken at 240 minutes.

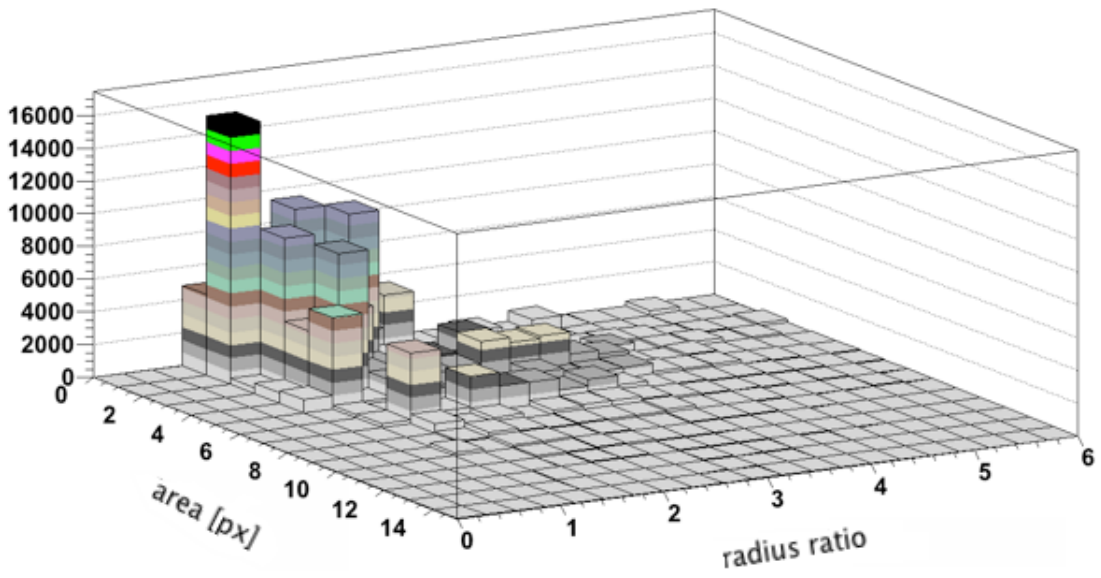

Figure 2.11: Lego plot for 45 minutes of etching of a tissue sample of 50 ppm of ^{10}B.

least, with rising etching time, the artificial objects due to CR-39 inhomogeneities as the ones evidenced in Figure 2.7 disappear.

It is important to compare some track parameters at different etching time. An irradiated tissue sample was taken and etched for 45, 90 and 135 minutes. At each step, random pictures were taken with LAS and analyzed with Image Pro 6.3. This time a new parameter has been considered, which is the radius ratio. This quantity defines the degree of roundness of the analyzed object, when the radius ratio is ≈ 1 it means that the objects are nearly round, while if the ratio is > 2.5 they tend to assume a non circular shape.

To better visualize the characteristics of the tracks, lego plots were built to compare the different etching times results. These plots sre shown in Figure (2.11) for 45 minutes, Figure (2.12) for 90 minutes and Figure (2.13) for 135 minutes.

Analyzing Figure (2.11), no correlation between area and radius ratio can be established. The data accumulate in an area between 1 and 6 pixels, while the radius ratio ranges from 1 to 4. This suggests that the previous image analysis (Section 2.1.2) did not perform a proper track selection. In fact, only the total number of tracks were counted, without a distinction of the particles causing the tracks. Nevertheless, a linear dependence of the total track density from the boron concentration was established, despite the presence of protons from neutron capture in nitrogen.

With 90 minutes of etching, Figure (2.12) the images show that most of the data form a peak in an area between 10 to 25 pixels (track area) and between 1 and 2.5 radius ratio. This

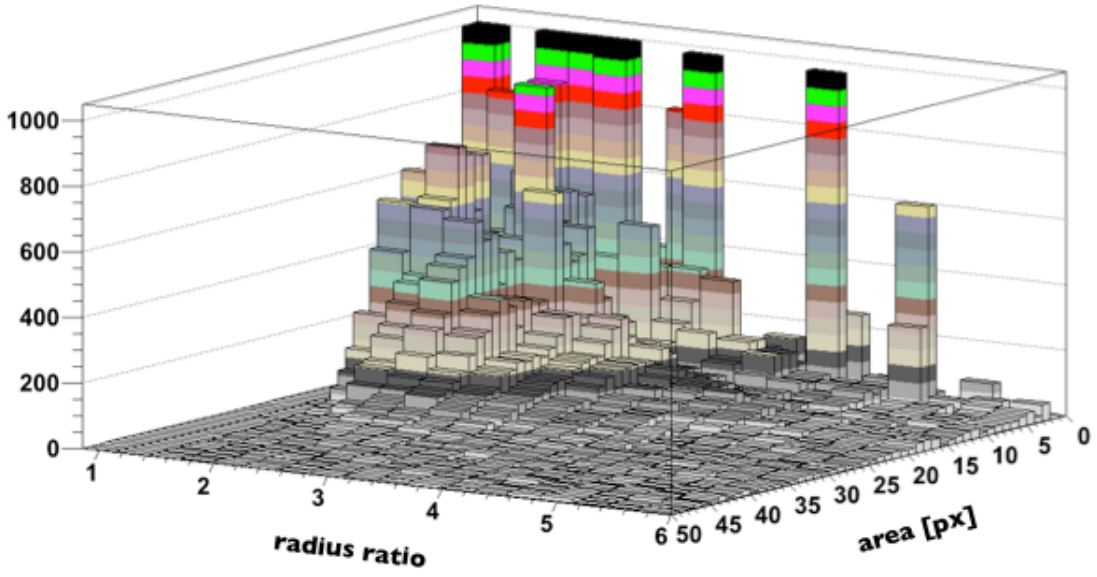

Figure 2.12: Lego plot for 90 minutes of etching of a tissue sample of 50 ppm of ^{10}B.

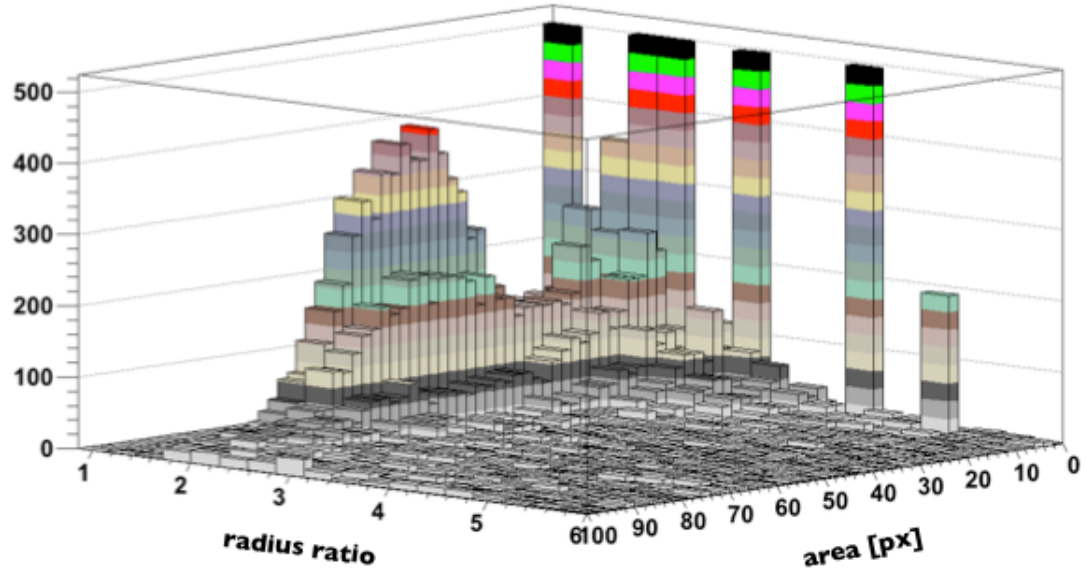

Figure 2.13: Lego plot for 135 minutes of etching of a tissue sample of 50 ppm of ^{10}B.

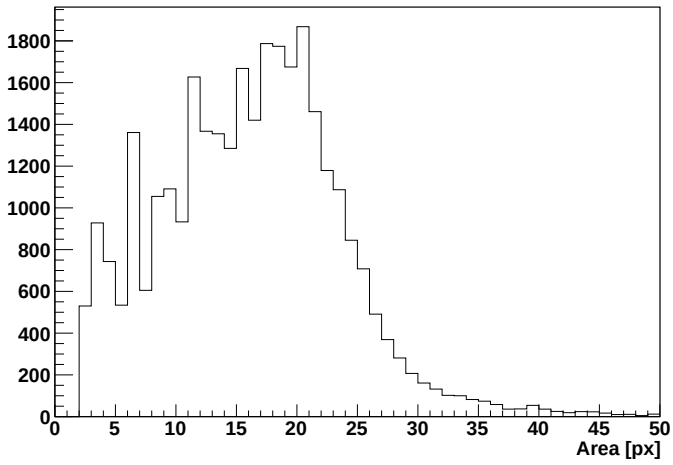

Figure 2.14: This histograms represents a two dimensional section of the lego plot (Figure 2.12). Only data with a radius ratio within 1 and 2.5 was selected.

means that there are similar objects on the picture and that they can be distinguished from artificial background entities, by triggering on the area and on the radius ratio. A clearer view is given by Figure (2.14) which is a section of the lego plot seen in Figure (2.12) with a trigger on the radius ratio between 1 and 2.5. In this histogram the peak of tracks that have an area of about 20 pixels is visible. Anyhow the peak is not well defined, and further etching is needed to improve the resolution.

Finally, the 135 minutes etching lead to the Figure (2.13), where a very defined peak can be seen, which ranges from 40 to 60 pixels in area and between 1 and 2 in radius ratios. In a further analysis, triggering on radius ratios from 1 to 2.5 and selecting areas larger than 1 pixel, two separate peaks can be distinguished. These two peaks are plotted in a two dimensional histogram in Figure (2.15). In this way, a useful working point was found, where the peak at areas of approximately 50 pixels could be recognized as the one due to alpha particles. The peak at areas of about 10 pixels could be due to proton or alpha and lithium particles with lower stopping power [9].

At last a consideration must be done regarding the overlapping tracks. From Figure (2.8) to Figure (2.10), the evolution of the tracks with increasing etching time can be followed, and it is clear that the tracks tend to overlap with increasing etching time. Especially those films with etching time higher than 180 minutes, have many of those multiple events. Therefore, if the same irradiation conditions must be kept for the liquid samples,

[9] This statement will be better discussed in Chapter (5), where the results of the simulations with SRIM will be described.

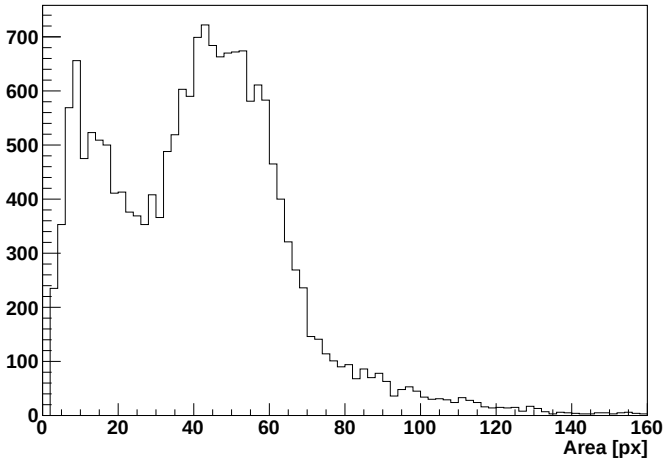

Figure 2.15: This histograms represents a two dimensional section of the lego plot (Figure 2.13). Only data with a radius ratio within 1 and 2.5 was selected.

Sample	Power (kW)	irradiation time (min)	Fluence (n/cm^2)	etching time (min)
Liquid	10	30	$(5.2 \pm 0.2)\ 10^{10}$	125
Tissue	1	30	$(0.98 \pm 0.055)\ 10^{10}$	125

Table 2.3: Working conditions.

the etching time must be less than 180 minutes to avoid overlapping tracks. On the other hand, the tissue samples, already at 135 minutes of etching, present overlapping conditions. This can be noticed in Figure (2.15) from the important tail of events that goes from 70 pixels onwards. Moreover, the difference in track density between liquid and tissue samples is due to the dry to fresh mass ratio. To equal the working condition, the ratio between the neutron fluence delivered to the tissues and to the liquid samples must equal the ratio of the fresh to dry mass. For simplicity, the liquid samples were irradiated with a reactor power of 10 kW, while the reactor power for the tissue sample was set to 1 kW. In table 2.3 is reported the summary of the new working conditions.

2.3 Image acquisition and analysis

Before moving to the calibration chapter, an improvement to the image acquisition system must be described. Image Pro Plus 7.0 was chosen as image acquisition and analysis program. This not only improved the image quality but also improved the acquisition

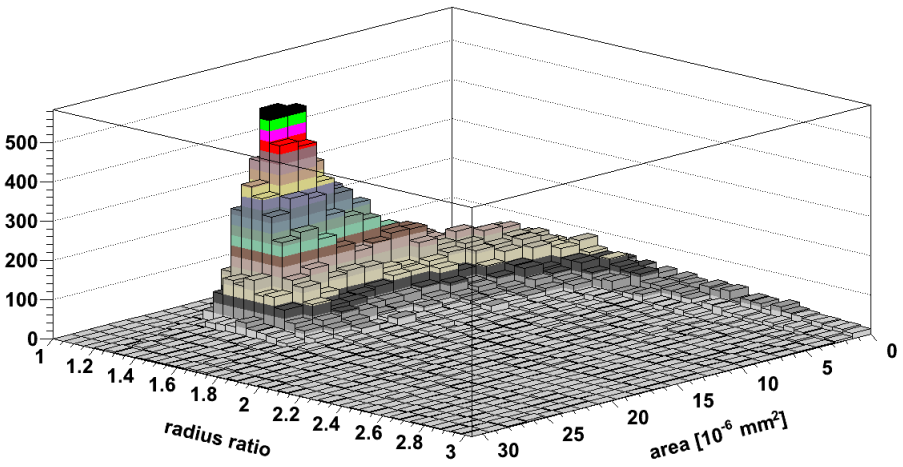

Figure 2.16: This is the lego plot of a liquid sample with 50 ppm of boron obtained with the new image acquisition system. Comparing it with Figure 2.13 it can be seen that the artificial 1 pixel objects disappear, making the low pixels range much cleaner. Another visible improvement is that the objects tend to be more circular, this is a index of the quality of the binarization.

mechanism by implementing an automated acquisition system, the Prior Optiscan stage, on which the CR-39 is positioned, was connected to the PC with a RS-232 cable. The automatization of the stage was not the only advantage: by giving the magnification of the microscope as an input to Image Pro Plus 7.0 the area of the tracks are automatically converted in mm^2. As a general consequence the overall quality of the system was improved and the image acquisition time was decreased, making it possible to have more statistical points, therefore decreasing the statistical error. Figure (2.16) is an example of this statement.

Once the images have been acquired, Image Pro Plus 7.0 performs some operations on the picture. The first one is the background subtraction to eliminate the inhomogeneities. Subsequently, the contrast of the picture is enhanced, in a way to darken the tracks of the particles. This step is done with the same parameters for all the analyzed pictures, since the acquisition conditions are the same.

The last step of the image analysis corresponds to the counting of the objects, by a counting function of Image Pro called *Count/Size*, where the objects are selected depending on their color. For the purpose of the analysis only dark objects are selected, the range of the selected gray scale is fixed for all the analyzed pictures. Finally, before the counting of the objects starts, the interesting parameters of the dark objects have to be selected. As

previously said, the calibration of the quantitative autoradiography is based on the *radius ratio* parameter and the *area* of the tracks. The fist one is important since it selects only circular shapes, while the latter parameter characterizes the energy deposition inside the CR-39 of the ionizing particle. From each analyzed picture a file is created where for each track on the picture the area and the radius ratio are stored. These files are then analyzed with a ROOT program, this analysis is discussed in the next chapter where the calibration is presented.

2.3.1 Repeatability check with a NIST sample

Concerning the final measurement result it is important, to prove that the irradiation working condition do not vary from the calibration conditions. Therefore, a standard sample purchased at NIST[10] consisting of a silicon wafer with a superficial boron atoms implantation, was put in a fixed position on a CR-39 outside the tissue sample and liquids holders. The track density obtained from the NIST standard provides a reference for the working conditions. For the analysis of the NIST autoradiography, the SSNTD is then etched as described in the previous section. While the graphical analysis is treated in the next chapter.

[10]National Institute of Standards and Technology's, Gaithersburg and Maryland, USA.

Chapter 3

Calibration of the QNCR Technique

Having obtained the propper working conditions, the next step was the improvement of the data analysis. The trigger was set as follows: a range of track areas from 0 to 40 $\times 10^{-6} mm^2$ was selected and only the objects with a radius ratio between 1 and 2.5 were kept. For each sample, all the tracks were plotted in a single histogram, showing the distribution of the selected objects area, Figure (3.1) shows this step for the liquid samples while Figure (3.2) shows the same results for the tissue samples.

Following the results of Chapter 5, all the tracks with an area larger than a certain threshold value are generated by the energy deposition of alpha and lithium ions. By observing Figure (5.17) and comparing it with Figure (5.18), the threshold value should be in the range that goes form 0 till 25 $\times 14^{-4} mm^2$. To make careful selections it is better to impose this threshold value to be near the peak given by the alpha and lithium particles. This way the protons are excluded from the calculations, thus only events coming form the neutron capture in boron are counted. Following these considerations the threshold value was set to 10 $\times 10^{-4} mm^2$. In addition, it can be said that if the response of the SSNTD depends only on the Stopping Power, and not the type of particle, $\approx$ 70% of the tracks with an area larger than the threshold are alpha particles. While the remaining 30% is due to the lithium ions. For smaller areas the contribution of the particles depend on the type of sample, for liquids the tracks are equally distributed between alpha and lithium ions. For the tissue, the proportions vary with concentration of boron, since the amount of alpha and lithium ions tracks depend on the concentration of ^{10}B in the tissue, while the quantity of protons is constant.

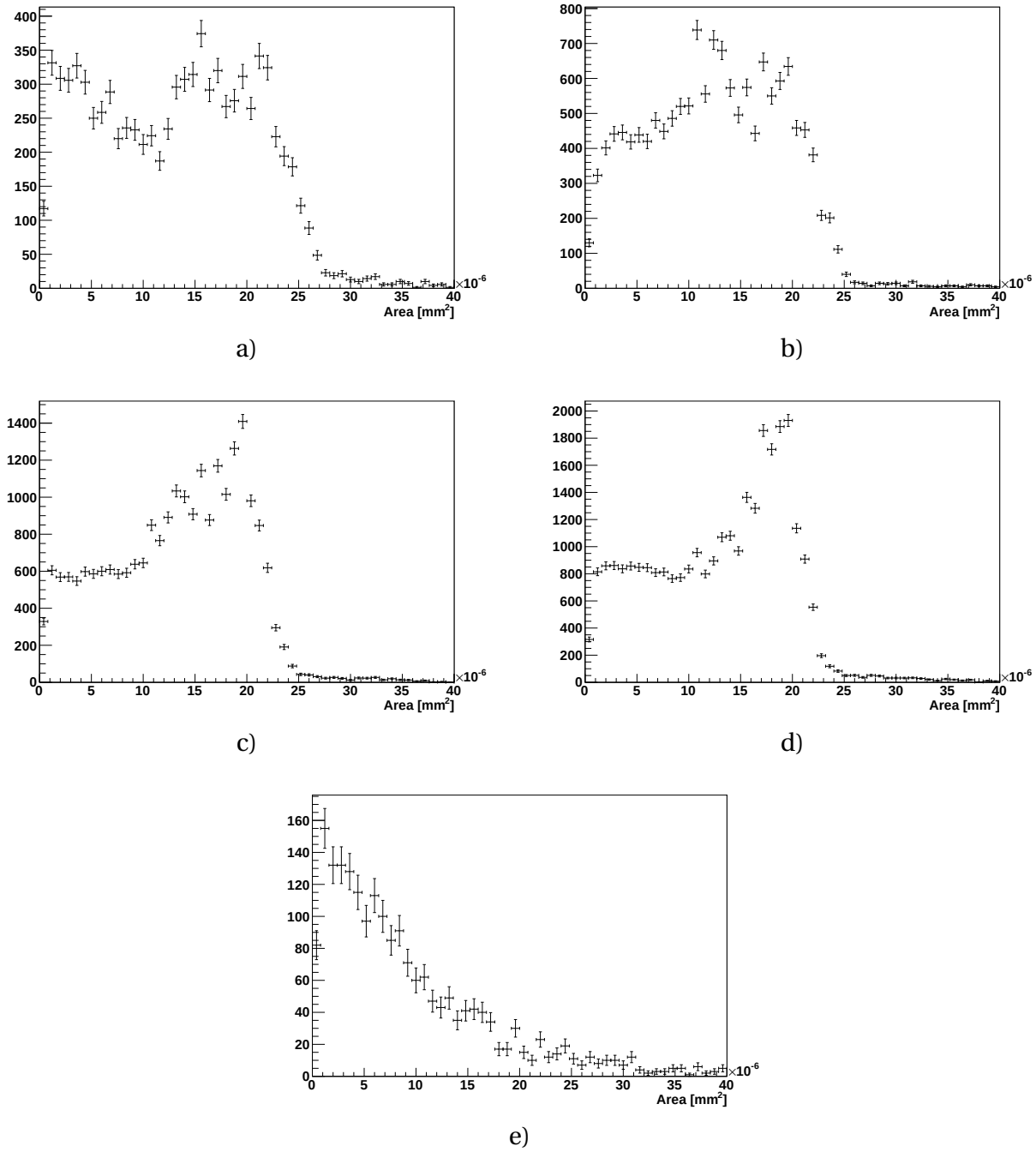

Figure 3.1: Area distribution histograms for the liquid sample, for each sample 100 pictures have been take. Where figure a) represents the histogram at 10 ppm, b) at 20 ppm, c) at 30 ppm, d) 50 ppm and e) 0 ppm.

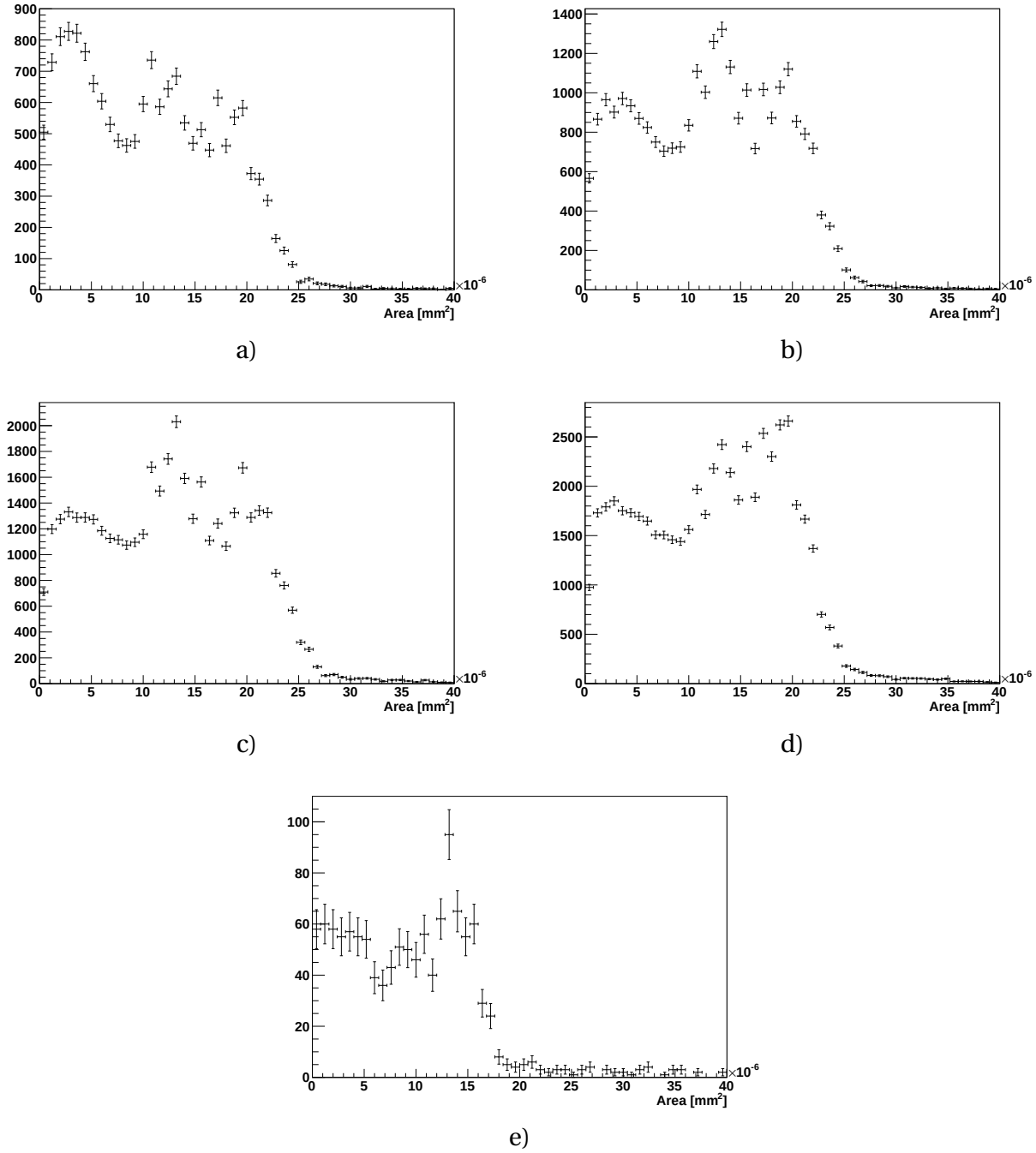

Figure 3.2: Area distribution histograms for the tissue sample, for each sample 100 pictures have been take. Where figure a) represents the histogram at 10 ppm, b) at 20 ppm, c) at 30 ppm, d) 50 ppm and e) 0 ppm.

The threshold value is then used to determine, for each sample, the number of tracks per picture that have an area larger than 14 $\times 10^{-4} mm^2$. The result is then plotted in an

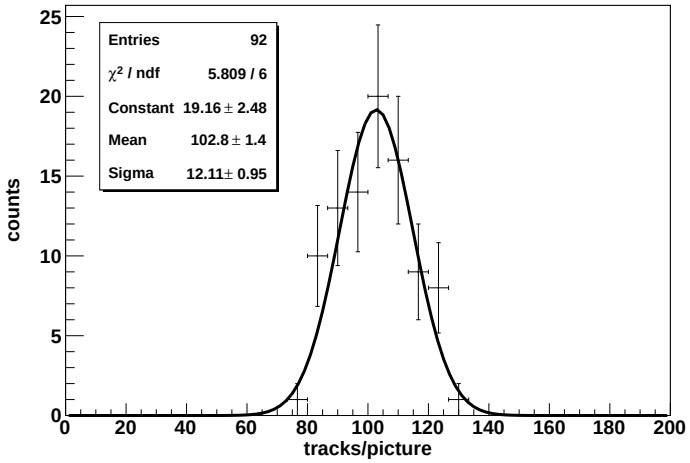

Figure 3.3: Tracks per picture of a liquid sample with 25 ppm of boron.

histogram giving the distribution of tracks per picture. This value should then be proportional to the boron concentration in the irradiated samples. This distribution is then fitted by a gaussian function, following the Central Limit Theorem since the number of random variables are more than 50 for each sample. Figure (3.3) represents the outcome for a liquid sample with 25 ppm of boron, while Figure (3.4) the outcome for a tissue sample with 30 ppm of boron. The same was also done for all those tracks that have an area value below the threshold parameter, Figure (3.5) is an example of the number of tracks with an area below $\times 10^{-4} mm^2$, this can be useful to estimate the amount of nitrogen present in the analyzed samples.

Tissue calibration curve

Figure 3.4 shows the fitted histogram of tracks per picture. In Table (3.1) the results of the mean value of the fitted gaussian curve are summarized. The calibration[1] result is shown in Figure 3.6, the slope error is $\approx$ 8% which is an improvement compared to the former calibration. In addition, Figure 3.11 describes the evolution of the track areas with values below the threshold, and also in this range of areas the tracks increase with the boron concentration. From Figure (3.11) it can be seen that in the number of counted tracks increase linearly with boron concentration, and that there is a non zero value for samples with 0

[1]The calibration has been done by following the results shown in Table (3.1) for the values above threshold, where the track counted at 0ppm are considered as background, hence it is subtracted from the other results.

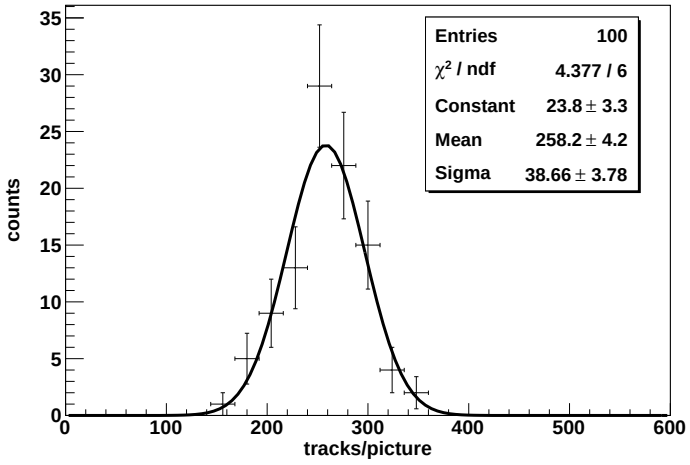

Figure 3.4: Tracks per picture of a tissue sample with 30 ppm of boron.

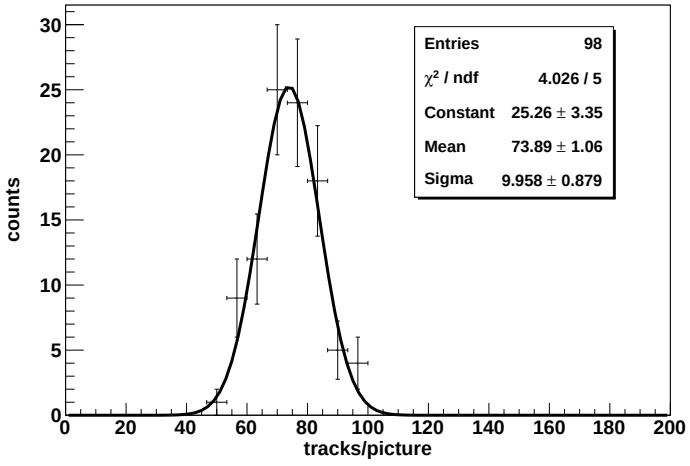

Figure 3.5: Tracks per picture, below the threshold value, of a liquid sample with 30 ppm of boron.

Sample	Number of track below the threshold per picture	error	Number of track above the threshold per picture	error
10 ppm	80	11	86	16
20 ppm	105	16	165	29
30 ppm	146	18	259	39
50 ppm	204	24	347	45
0 ppm	7	3	6	3

Table 3.1: Results from the analysis of the standard tissue samples.

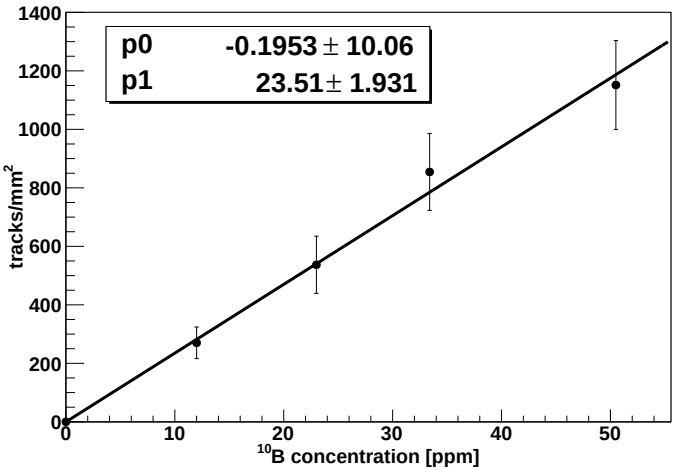

Figure 3.6: Tissue calibration curve. Track evolution for areas bigger than the threshold value.

ppm of boron. This value is possibly due to protons coming from the neutron capture on nitrogen atoms.

In Figure (3.8) and Figure (3.9) the analysis of the tracks due to standard sample from NIST are shown for the irradiation of the tissue.

Liquid calibration curve

The same process as for the solid samples was performed for the liquid ones. The result can be seen in Table 3.2 and in Figure 3.10. The slope error has remarkably improved to an uncertainty of ≈ 6%.

Also during the irradiation of the liquid samples, a reference NIST was positioned inside the thermal column. The analysis follow the same conditions of the other samples, so the results of this autoradiography are shown in Figure (3.12) and Figure (3.13).

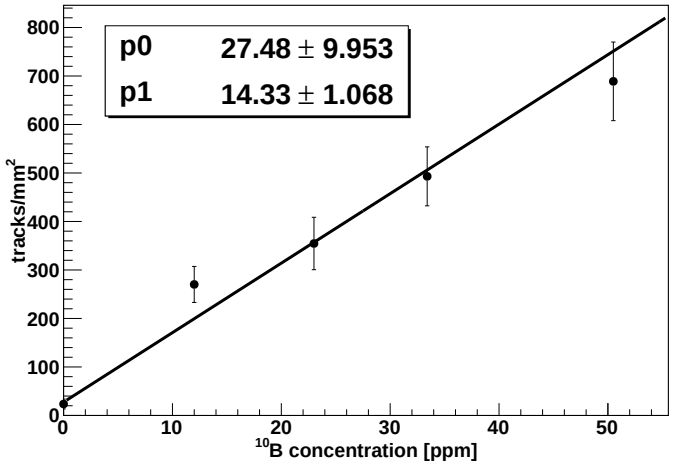

Figure 3.7: Tissue calibration curve. Track evolution for areas below the threshold value.

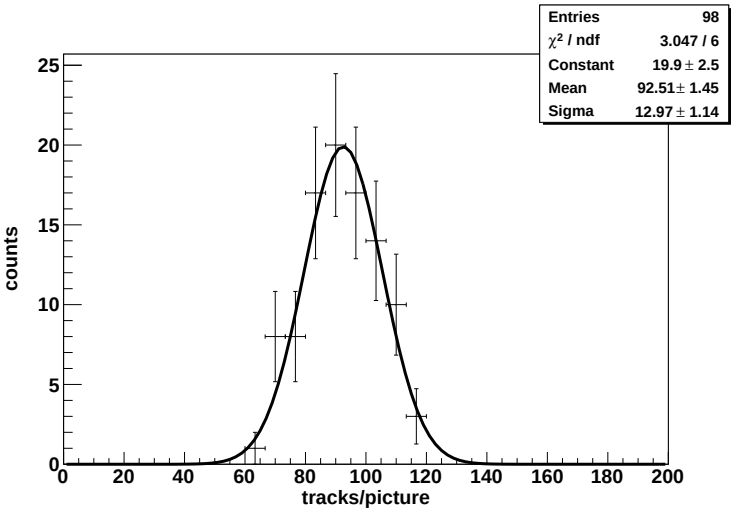

Figure 3.8: Number of tracks in the NIST sample, of the tissue irradiation, for area values above the threshold value.

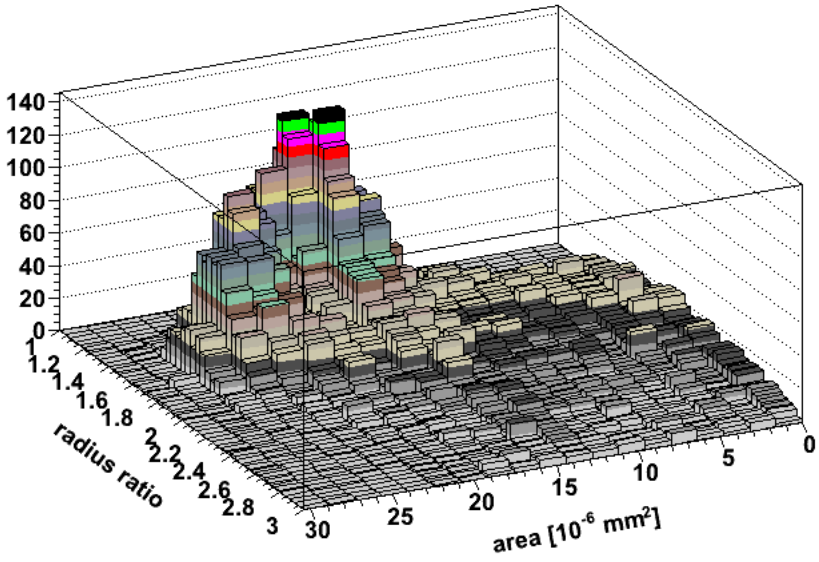

Figure 3.9: Nist autoradiography for tissue samples, the Figure shows a lego plot showing the distribution of the tracks accordingly to area and radius ratio.

Sample	Number of track below the threshold per picture	error	Number of track above the threshold per picture	error
5 ppm	25	7	33	6
10 ppm	30	9	56	8
20 ppm	56	9	96	13
25 ppm	54	10	102	12
30 ppm	74	10	120	15
50 ppm	103	20	194	23
100 ppm	154	26	388	31
0 ppm	18	5	1	1

Table 3.2: Results from the analysis of the standard liquid samples.

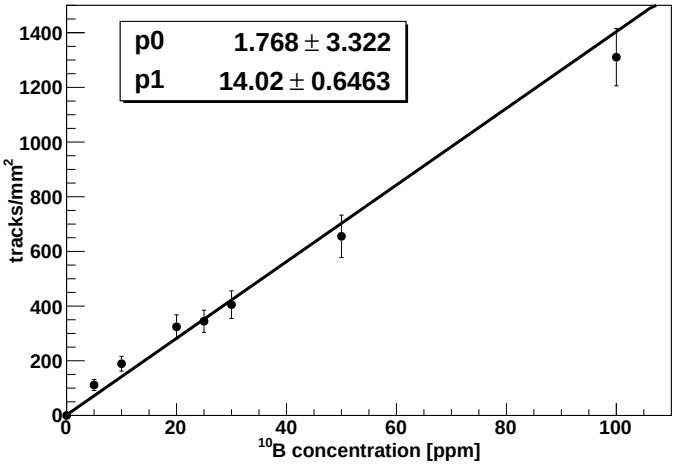

Figure 3.10: Liquid calibration curve. Track evolution for areas bigger than the threshold value.

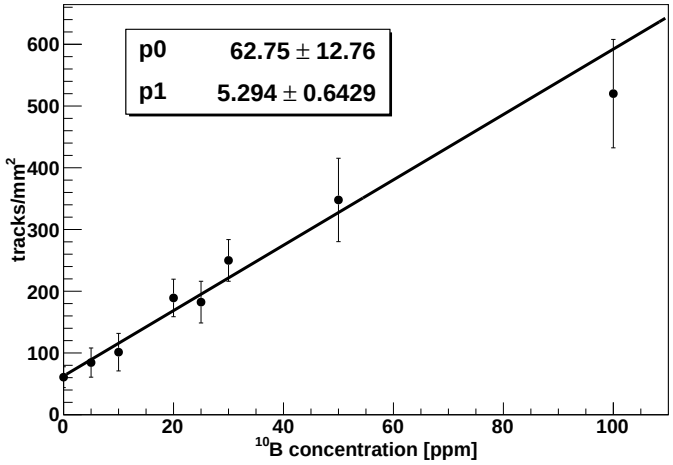

Figure 3.11: Liquid calibration curve. Track evolution for areas below the threshold value.

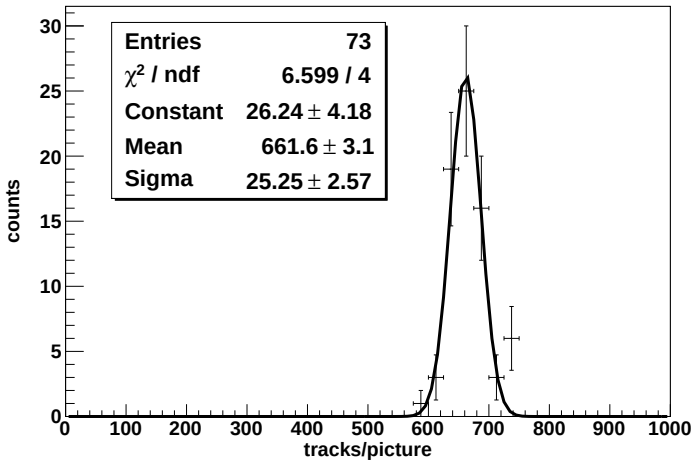

Figure 3.12: Number of tracks in the NIST sample, of the liquid irradiation, for area values above the threshold value.

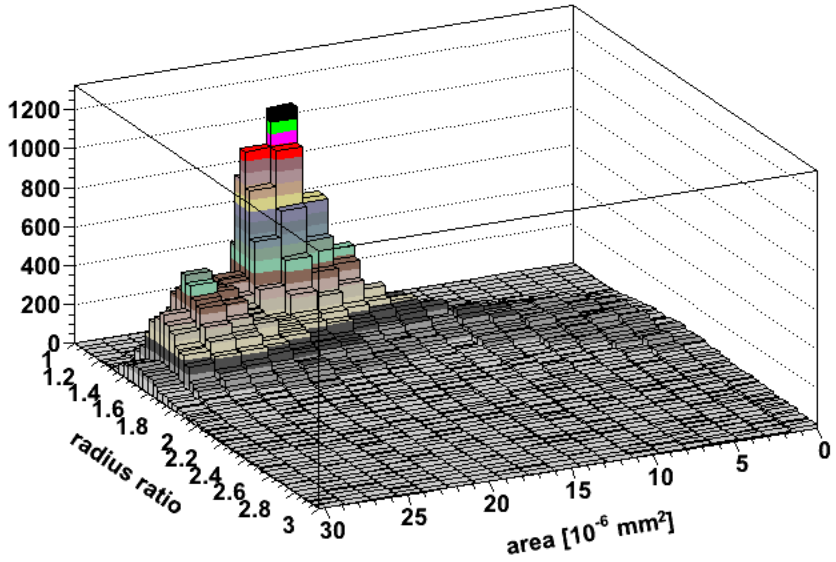

Figure 3.13: NIST autoradiography for liquid samples, the Figure shows a lego plot with the distribution of the tracks accordingly to area and radius ratio.

3.1 Final considerations

To conclude, the calibration obtained for both liquid and solid samples is very precise and the linearity in the whole range of concentrations tested is excellent. With the new calibration, the dry to fresh mass ratio obtained from the calibration curve slope ratio is 0.135 ± 0.013[2], that is in good agreement to (0.15 ± 0.01) obtained from the measurement with the digital scale. In the next chapter these calibration curves are used to measure boron concentrations in cells cultured in presence of new boronated formulations in order to thest their effectiveness in conveying boron.

The autoradiography of the NIST sample allows normalizing the working conditions, that can be different from the ones at the time of the calibration samples irradiation, for ex. due to power fluctuation. The reference values that are used for normalizing are 311 ± 44 $tracks/mm^2$ for the tissue and 2230 ± 85 $tracks/mm^2$ for the liquid.

An interesting result can be deduced from Figure (3.11), where the intercept with the y-axis should represent the number of protons reaching the SSNTD. This value is related to the amount of nitrogen in the tissue. From the simulations in Chapter 5, the number of protons transmitted by the solid sample are ≈ 65 tracks/mm^2. Since the detector is not 100% efficient most of those protons will not be revealed, an estimation of the detector efficiency can be done by comparing the experimental results to the simulated ones, therefore an efficiency of $\approx 50\%$ can be expected. So the number of detected protons should be ≈ 33 tracks/mm^2, that is in agreement with the experimental value of ≈ 27 tracks/mm^2.

A final consideration must be done about the error bars of the calibration curve. The error associated to each value is the standard deviation of the data over the entire sample. A smaller error could have been considered, given by the standard deviation of the mean. Anyhow the latter was discarded, and the standard deviation of the mean was preferred, since it gives the chance to estimate the micro-distribution of boron within the sample. In fact, a broader the distribution means that the pictures taken for one sample were not uniform. This value is of interest for BNCT since the uniformity of ^{10}B bio-distribution in tumor and in normal tissue plays a crucial role for the outcome of the irradiation. Therefore, with autoradiography it is possible to estimate the *in-vivo* micro-distribution of boron in tumor and healthy tissue. This is an important parameter for the therapeutic efficacy of BNCT, since radiobiological studies revealed wide variations in boron content, providing tissue response data that could not be explained on the basis of gross boron content alone.

[2]A correction factor, calculated in the simulation Chapter 5, for the thickness of the tissue sample was considered in the calculation of the dry to fresh mass ratio.

In subsequent studies, it was proven that boron targeting homogeneity is important for BNCT success, even if the absolute tumor boron concentration is lower [43].

Chapter 4

Boron carrier analysis for BNCT

The autoradiography technique (QNCR) is important for the future developments of BNCT, where new carriers and boron distribution inside the tissue must be studied. The advantage of QNCR is that concentration measurements of ^{10}B can be performed for both liquid and tissue samples, and that the homogeneity of the boron distribution can be investigated. Another important characteristic is its simplicity associated to a fast achievement of the result. Therefore, autoradiography was implemented in Pavia for the BNCT project on Osteosarcoma, for which new carriers are being tested. In the following section, results for *Liposomes*, *polymeric nanopartcles* and *gold nanoparticles* are exposed, these should be interpreted as some preliminary measurements needing future developments. The outcome of the experiments with new carriers are compared with the results of BPA, that was used as a reference since it is the drug presently used for clinical BNCT, giving an idea of which new drugs has a promising future. These experiments were performed on UMR-106 rat osteoblastic carcinoma cells, cultured in presence of the boronated formulations for 4 hours, after that the cells were centrifuged and deposited on mylar films.

As it is the first time that the QNCR technique is used in Pavia, before employing it as a self standing boron measuring method, it is important to compare the results to the ones of alpha spectrometry (AS). Therefore, the experiments with BPA and Liposomes were performed with both QNCR and AS (Section (4.1) and Section(4.2)), showing that the outcomes are in good agreement. Moreover, through a collaboration with a group working at CNEA[1] (Argentina), samples of healthy rat liver treated with BPA (following a routine administration protocol.) were sectioned to be measured by QNCR and AS in PV and by ICP-AES, ICP-MS and QNCR with different films in Buenos Aires. Although the project

[1] The analyzed samples were prepared by Dr. Agustina in Portu.

is in an early stage, Table (4.1) shows that all the cited techniques are consistent for ^{10}B concentration measurements.

Technique	Sample 1 Boron (ppm)	Sample 1 error (ppm)	Sample 2 Boron (ppm)	Sample 2 error (ppm)
ICP-OES	19.1	0.7	20.7	0.8
ICP-MS	23	1	22	3
QNCR Arg	21	2	21	2
AS	26	4	25	3
QNCR Pavia	18.5	2	23	2

Table 4.1: Comparing techniques for boron concentration measurements.

In the following sections the autoradiography technique calibrated in chapter (3) is applied to samples of cells treated with the new formulations. To simplify the exposures of the results, this chapter is divided in subsections. In each subsection the results are exposed in tables followed by the description of the samples and the discussion of the result.

4.1 Cell samples with BPA

The molecular structure of BPA was shown in the Introduction Chapter. As already stated, this boron carrier is the most widely used in BNCT, therefore the first step to study new molecules is to have a comparison with the absorption due to BPA, which becomes a reference for the new carriers tested.

The UMR-106 cell cultures were exposed to 80 μg/g of BPA. In Table (4.2) the results of the QNCR and AS boron measurements are compared. As shown, the results are compatible for all the analyzed samples. An observation can be made on the difference between the two measuring techniques: for the samples containing < 5ppm the relative error of QNCR results is higher, while for those samples containing > 20 ppm the relative error of AS becomes greater.

Table (4.2) reports an experiment of boron absorption after the administration of d,l-BPA and l-BPA. Since cells do not absorb d-BPA, one expects that the concentration in cells exposed to the d,l-BPA is half the one in cells exposed to l-BPA. This is in fact compatible with the result shown.

Sample	Autoradiography Boron (ppm)	error (ppm)	AS Boron (ppm)	error (ppm)
UMR-CTR	3.7	1.3	2.9	0.4
UMR-d,l-BPA	24	2.7	20	3
UMR-l-BPA	40	4	46.5	6.5

Table 4.2: Results of BPA absorption in UMR cells, obtained by QNCR and AS. CTR stands for control cells, where the quantity of boron is measured in cells not exposed to BPA. The l and d before BPA stand for levorotatory and dextrorotatory correspondingly. The values were corrected taking into account the difference in dry to fresh mass ratio between the standard samples (used in the calibration) and the one of the cell samples.

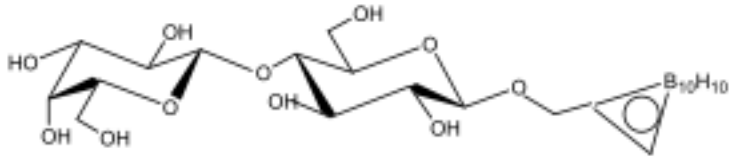

Figure 4.1: Schematic view of *o*-closocarboranyl β-lactoside.

4.2 Cationic liposomes loaded with LCOB

In this section a new boron compound of carborane[2] derivative is employed, namely, *o*-closocarboranyl β-lactoside[3] (LCOB) shown in Figure (4.1). This drug is transported to the cell by a liposome, which is a common vehicle used in medicine (Figure (4.2)), consisting of a vesicle composed by a lipid bilayer, the same as the cell membrane. For this reason liposomes are easily absorbed by the cells. Cationic liposomes were selected because they had already showed the best uptake properties in previous studies [2]. Table (4.3) and Table (4.4), show the results of boron concentration measurements in two different experiments using cationic liposomes charged with LCOB.

Table (4.3) refers to the experiment where cells were exposed to cationic liposomes charged with LCOB, where the initial boron concentration in the medium of culture was 2.4 μg/g. From the results of Table (4.3), it can be stated that the control cells (CTR) and cells contain only liposomes (CTR+LIPO) have the same boron concentration. The samples treated by boronated liposomes (LIPO-LCOB) samples contain $\approx 20 \pm 1.3$ μg/g of

[2]A carborane is a cluster composed of boron and carbon atoms.
[3]The LCOB carboranes are synthesized at the University of Piemonte Orientale, Italy.

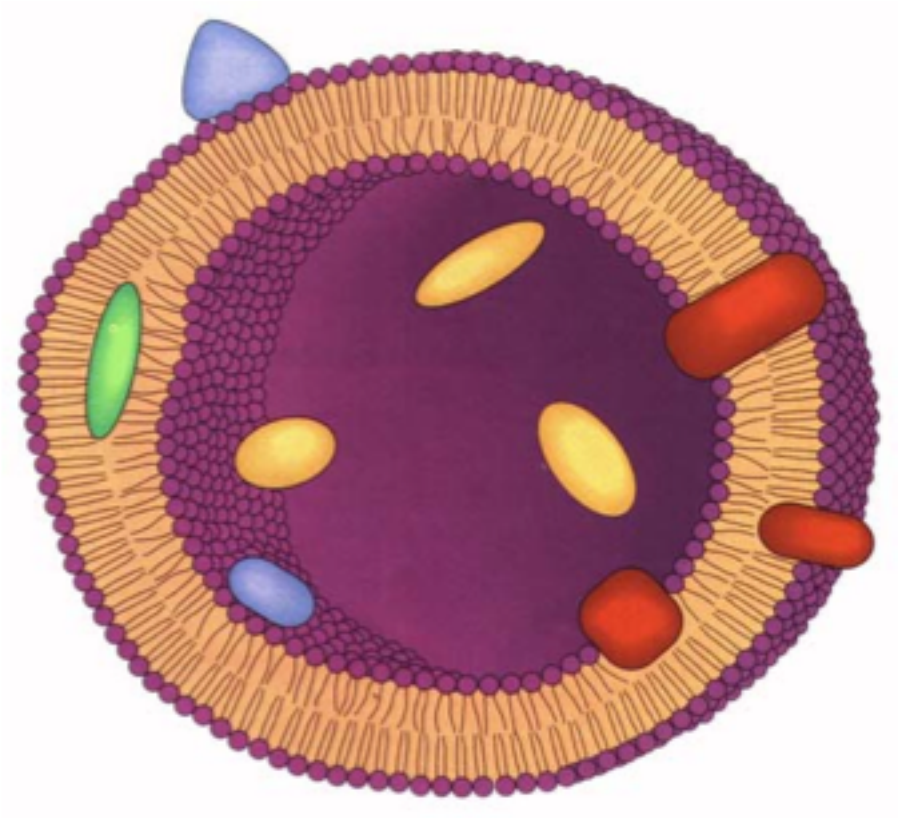

Figure 4.2: The structure of a Liposome, where it is shown how the molecules are carried: hydrophilic molecules are entrapped into the aqueous core of the liposome (yellow); hydrophobic molecules are encapsulated into the lipid bilayer (green); other molecules, with a more complex chemistry, are adsorbed onto the membrane surface with possible partial intercalation in the bilayer (red); a chemical bond between molecule and lipids (blue) is also possible [25].

Sample	Autoradiography Boron (ppm)	error (ppm)	AS Boron (ppm)	error (ppm)
CTR-1	3.7	1.3	4.9	0.7
CTR-2	3.2	1.3	5	0.8
CTR+LIPO-1	3.5	1.3	5.1	0.8
CTR+LIPO-2	3.7	1.3	5.8	0.9
LIPO-LCOB-1	19.1	1.3	19	3
LIPO-LCOB-2	19.1	1.3	26	4
LIPO-LCOB-3	21.3	1.3	28	4

Table 4.3: Results of boron concentration measurement by AS and QNCR. Where CTR stand for cells not exposed to liposomes or LCOB, CTR+LIPO are those cell cultures exposed only to liposomes and LIPO-LCOB are those cultures exposed to liposomes charged with LCOB. The number after each name corresponds to a different sample.

boron. This means that the cells have absorbed and concentrated boron[4]. The results of QNCR for the three samples treated with LCBO are compatible with each other, while AS results present a higher variation. This variation might be due to a not uniform distribution of ^{10}B, this hypothesis is supported by boron imaging obtained by qualitative autoradiography. In Figure (4.3) it can be seen that on the borders of the sample there is a higher concentration of tracks. The pictures for the QNCR analysis were taken in the center of the sample, not taking into account the area next to the border. This is confirmed by LIPO-LCOB-1 sample that does not show the border inhomogeneity, and the result from QNCR and AS are compatible. To investigate this issue more deeply, pictures on the border were taken for QNCR, confirming that the mean boron concentration is higher in this region. For the LIPO-LCOB-2 sample the border has a mean boron concentration of 30 ± 3 ppm while the centre has a concentration of 20 ± 2 ppm. Therefore, the weighted average over the area of boron results to be ≈ 23 ppm which is more compatible with the result of AS.

Table (4.4) refers to the experiment where cells were exposed to cationic liposomes charged with LCOB, where the initial boron concentration was 1.66 μg/g.

[4]The concentration of boron in the initial condition is calculated by taking into account the mass of the cells plus the one of culture. After 4 hours the cells are separated from the culture, therefore the final concentration corresponds to the amount of boron inside the cells.

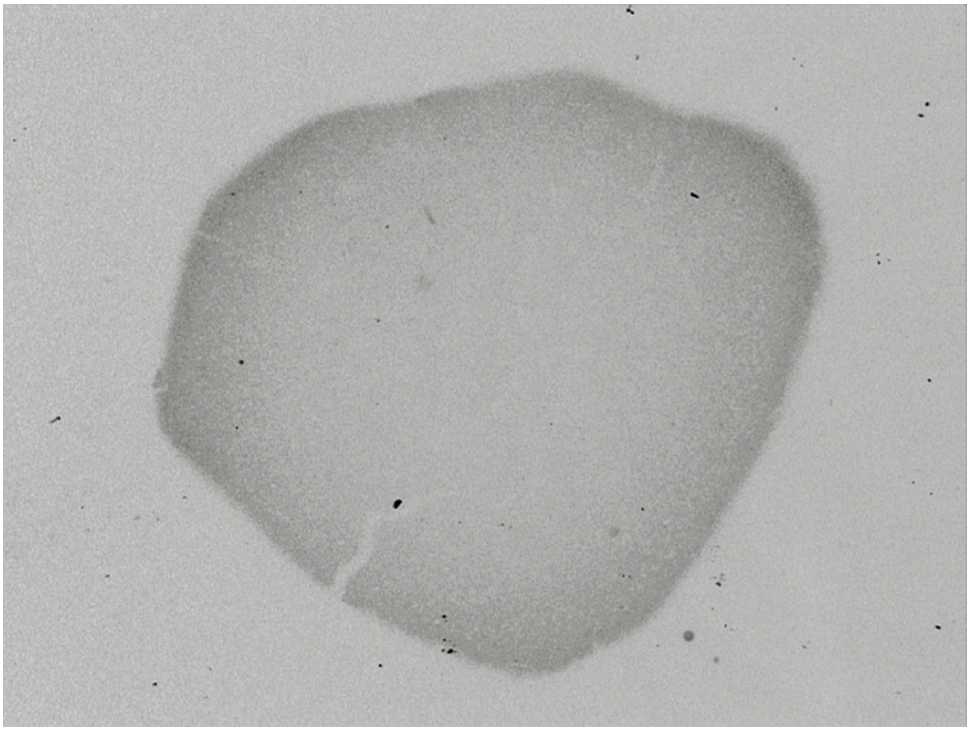

Figure 4.3: Picture of a sample of cells treated with boronated liposome developed for qualitative autoradiography, showing border inhomogeneity.

Sample	Autoradiography Boron (ppm)	error (ppm)	AS Boron (ppm)	error (ppm)
CTR	2	1.3	1.3	0.2
CTR+LIPO	2	1.3	0.8	0.1
LIPO-LCOB-1	10.7	1.3	12	2
LIPO-LCOB-3	18	5	11	2

Table 4.4: Results of boron concentration measurements with AS and QNCR. CTR stand for cells not exposed to liposomes, CTR+LIPO are cell cultures exposed only to liposomes and LIPO-LCOB are cultures exposed to liposomes charged with LCOB. The number after each name corresponds to a different sample.

As before, from the results of Table (4.3), it can be stated that the CTR and CTR+LIPO cells contain the same amount of boron. The results for LIPO-LCOB samples are practically identical with eachother when measured by AS, while for QNCR there is a difference. It can be seen that the QNCR of LIPO-LCOB-3 shows an higher concentration with an associated relative error of $\approx 30\%$ due to non-uniform distribution. This error is much higher than in uniform samples, which is $\approx 10\%$. To better understand this result, a qualitative autoradiography picture was obtained: the image is reported in Figure (4.4), that clearly shows a darker spot on the sample. New quantitative pictures were thus taken in the low and high track density areas, the results are listed in Table (4.5). By averaging over the two areas, the mean boron concentration in the sample is 8 ± 2 ppm, which is compatible with the result of AS.

area	Boron (ppm)	Error(ppm)
Low track density area	7	1
High track density area	17	3

Table 4.5: Results for boron measurements in different areas of the CR-39.

As a conclusion it can be said that the results of the experiments with cationic liposomes charged with LCOB are very promising, in fact the cells not only absorb boron but they concentrate ≈ 10 times the boron present in the extracellular environment. Usually the uptake factor in the cell cultures is 0.5 for BPA, thus liposomes with LCOB show an effectiveness 50 times higher than BPA, at least in these preliminary measurements.

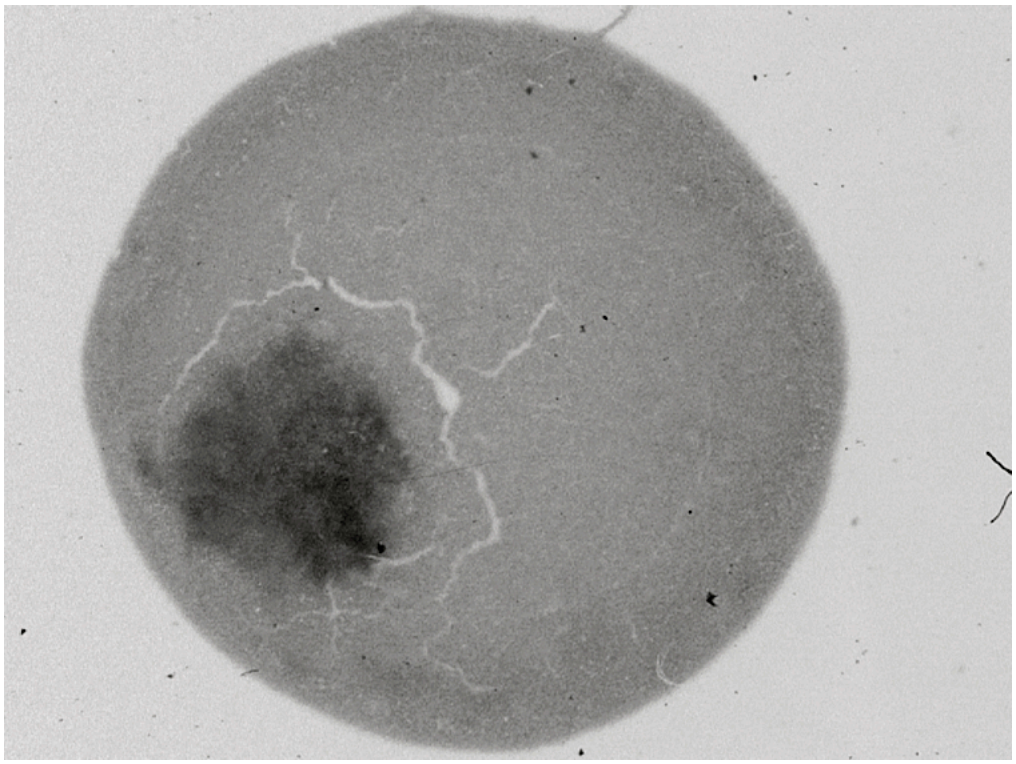

Figure 4.4: Qualitative autoradiography of a cell sample treated with liposomes loaded with LCBO, showing an inhomogeneity of boron distribution.

4.3 Polymeric nanoparticles

The polymeric nano particles are synthesized at the University of Piemonte Orientale, and are composed by polyethylenoxyde-polycaprolactone with carborane units covalently bound to the PCL block (PEO-b-PCL) as shown in Figure (4.5). This polymer is composed by polycaprolactone (PCL), a biocompatible molecule which is already used in several biomedical applications, showing an excellent biocompatibility. The other section of the polymer is composed by polyethylene-oxide (PEO), which is used to prevent the interactions with cytokines, thus prolonging the circulation time in vivo. When PEO-b-PCL is dissolved in water it shows an aggregation into nanosized micelles (10-30 nm), therefore those polymers are called nano particles. In this experiment the cells were exposed to the polymeric nanoparticles, with an initial boron concentration of 1.27 μg/g.

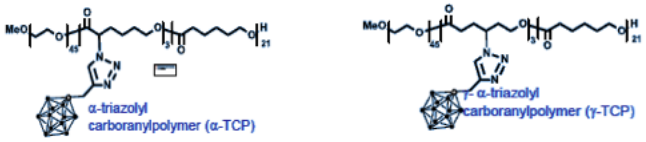

Figure 4.5: Polymeric nano particles structure.

Sample	Autoradiography Boron (ppm)	error (ppm)
CTR-1	4	1.3
CTR-2	5.3	2
ALPHA-1	6.7	1.3
ALPHA-2	6.7	3.3
BETA-1	4	1.3
BETA-2	3.3	1.3

Table 4.6: Results of QNCR in UMR-106 cells, where the CTR sample was exposed to the polymer without boron, while the ALPHA and BETA samples are cell cultures exposed to two different formulation of PEO-b-PCL polymers.

Table (4.6) shows that it is not possible to establish any difference between the samples not exposed to PEO-b-PCL and the ones exposed to these nanoparticles. Therefore, nothing can actually be concluded from these results, only some suppositions can be made, about the synthesizing process and the PEO-b-PCL and carborane binding. Something

could have gone wrong during the cell culture or maybe an insufficient drug dose was administered to cell cultures. To exclude that the polymeric nano particle lost boron before the administration to cells, 1 ml of water containing nanoparticles was irradiated in the liquid samples holder. The results of the QNRC are shown in Table (4.7). It resulted that the Alpha polymeric nano particle contain boron. Further analysis must be performed to exclude or consider these nanoparticles for their use in BNCT.

Sample	Autoradiography Boron (ppm)	error (ppm)
PEO-PCL	0.85	0.65
ALPHA	167	7

Table 4.7: The results of liquid samples containing nanoparticles autoradiography. The PEO-PCL sample corresponds to the nano particle without carborane, while the ALPHA sample is a polymer bound to a carborane.

4.4 Gold Nano Particles (AuNP)

Gold nano particles are generally considered as innovative and promising drug vectors. In particular Gold has been selected since it is an inert metal, which is an important condition for biomedical applications. The nano particles are functionalized at the University of Firenze with an O-carborane (OCB).

The result of the autoradiography analysis for osteosarcoma cells exposed to AuNP are shown in Table (4.8). From the outcome of the QNCR it is clear that the cells absorbed boron: the formulation named Gold1 concentrated 12.4 ± 2.5 ppm of ^{10}B, while the one named Gold2 concentrated 15 ± 5 ppm of ^{10}B. Nevertheless an experimental problem arose: when the cells were removed from the culture medium and centrifuged, it was not possible to separate them from the AuNP still present in the medium. In order to quantify the amount of boron remained in the cell pellet UMR-106 cultures were exposed to AuNP only for few minutes and then separated from the medium in the same way as before. The results of this experience are shown in Table (4.9): ^{10}B concentration of 7.7 ± 1.5 ppm was measured in Gold1 and a concentration of 3.7 ± 1.5 ppm was measured in Gold2. As the cells were exposed to AuNP only for few minutes, it is likely that the measured boron is attached to the cell pellet but not internalized. Thus this concentrations should be taken into account to when analyzing the results in Table (4.8), that in this way would show that only Gold2 differentiated from the control samples

Sample	Autoradiography Boron (ppm)	error (ppm)
Gold1-1	13.3	4
Gold1-2	11.5	1.3
Gold2-1	14	3.2
Gold2-2	16	6.7

Table 4.8: Results for the Autoradiography of UMR-106 cells exposed to nanoparticles for 4 hours. Gold1 and Gold2 are two different gold nanoparticles formulations, while the second number represents two different samples. CRT cells were measured in the previous the previous irradiations, showing a ^{10}B concentration of 3.4 ± 1.3 ppm of ^{10}B

Sample	Autoradiography Boron (ppm)	error (ppm)
Gold1-1	9.3	1.3
Gold1-2	6.2	2
Gold2-1	4	1.3
Gold2-2	3.5	2

Table 4.9: Results for the Autoradiography of UMR-106 cells exposed to nanoparticles for few minutes. Gold1 and Gold2 are two different gold nanoparticles formulations, while the second number represents two different samples.

This very preliminary experiment evidenced the need to set-up a suitable system to treat the cells after the administration of AuNP, that for their nature are quite different from the carriers studied before.

In conclusion, the most effective carrier appears to be liposomes charged with LCOB, at least in these exploratory tests.

Chapter 5

Simulation with The Stopping and Range of Ions in Matter (SRIM)

In the calibration chapter, Figure (3.1) shows the area distribution of the tracks left by the ionizing particles on the CR-39 after the etching. As shown in Chapter (1), the diameter of the track is a function of the track etch rate which depends on the damage of the particle in the SSNTD. Therefore the area of the track is a function of the energy deposition (which is a parameter that quantifies the damage) along the trajectory of the particle. In order to understand how the stopping power distribution of the transmitted particles affects the area distribution of the tracks, some simulations were performed.

The Stopping and Ranges of Ions in Matter (SRIM) is a free program developed by Ziegler [55].Inside SRIM there is an application called *Transport of Ions in Matter* (TRIM), which has a user friendly interface that allows setting up a simulation of ion transport in matter. TRIM can be used to calculate the stopping and range of ions with energies that go from 10eV/amu to 2GeV/amu. To simulate the transport of ions in matter TRIM uses a quantum mechanical treatment of ion-atom collisions. This calculation is made very efficient by the use of statistical algorithms which allow the ion to make jumps between calculated collisions and then averaging the collision results over the intervening gap [23]. During the collisions, the ion and the atom have a screened Coulomb collision, including exchange and correlation interactions between the overlapping electron shells. The ion undergoes long range interactions creating electron excitations and plasmons within the target. These are described by including a description of the target's collective electronic structure and interatomic bond structure when the calculation is setup. The charge state of the ion within the target is described using the concept of effective charge, which in-

cludes a velocity dependent charge state and long range screening due to the collective electron sea of the target. TRIM accepts complex targets made of compound materials with up to eight layers, each of different materials. It calculates both the final 3D distribution of the ions and also all kinetic phenomena associated with the ion energy loss: target damage, sputtering, ionization, and phonon production. All target atom cascades in the target can be followed in detail.

For this thesis, TRIM was employed to compute the mean stopping power of the ionizing particles, generated in the irradiated samples, and reaching the surface of the SSNTD.

The transport of $protons$, $alpha$ and Li ions was simulated in water and dry organic tissue, reproducing the ionizing particles that arise during the irradiation of the samples, due to neutron capture in boron and nitrogen, other interaction can be neglected. $Protons$, $alpha$ and Li ions from neutron capture reactions have well defined energies and are emitted isotropically in all directions. Before proceeding with the simulation description, the next chapter will introduce the TRIM interface and its most interesting characteristics.

5.1 TRIM

The TRIM interface is shown in Figure 5.1, the first input parameter is the type of TRIM calculation (top right corner). Since the physical system that will be simulated has a stochastic nature, the correct field to select is *Various Ion Energy / Angle / Positions*. This option allows the calculation of TRIM with ions starting at various energies, or with varying trajectory angles to the target surface, or starting at various depths in the target. This option requires the file TRIM.DAT for the initial ion energy, trajectory and starting position. This file must be generated using an external Monte-Carlo code that will be reported below. Alongside the *Various Ion Energy / Angle / Positions* option the *Ion Distribution and Quick Calculation of Damage* was selected. Although there is a more detailed calculation option, for the purpose of the simulation the Quick calculation is enough, since the quantities Final distribution of ions in the target, Ionization energy loss by the ion into the target, Energy transferred to recoil atoms, Backscattered Ions and Transmitted Ions are correctly calculated also with this option.

The next input data is the Ion name, mass, energy and incidence angle. For the purpose of this simulation, there is no need to specify the ion name, mass and incidence angle, because those parameters are defined in the TRIM.DAT file, selected in the TRIM

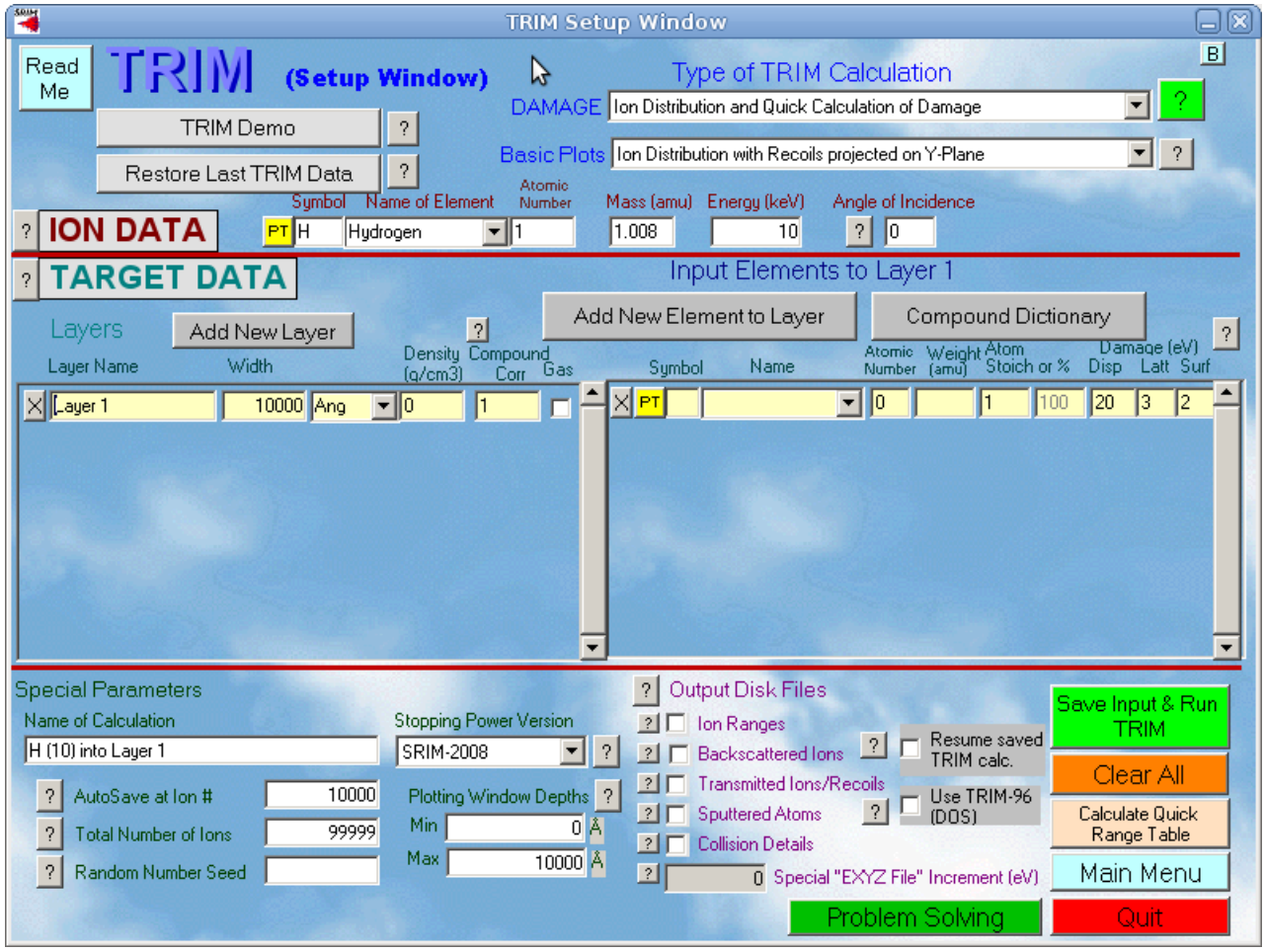

Figure 5.1: The TRIM Setup Window is used to input the data on the ion, target, and the type of TRIM calculation that is wanted.

Calculation option. The only data that must be filled is the maximum energy of the ion, even if the actual energy of the transported particle is always defined in the TRIM.DAT file.

After the Ion definition, the following input is the target description. Up to 8 layers can be defined, that can be made up of a compound or a single atom material. A simple way to define a layer is by searching in the compound dictionary. In addition to the compound stoichiometry, this table provides typical densities and also binding information. For many light compounds, especially hydrocarbons, this bonding information are later used to make significant corrections to the stopping powers. For the simulation under study the selected compounds were: Water(iquid), CR39(solid) and dehydrated tissue.

Before starting the TRIM simulation by clicking on the *Save Input and Run TRIM* button, some calculation parameters and output files options must be defined. Default parameters were selected for the calculation parameters, on the other hand, for the *Output Disk Fles*, the box corresponding to *Transmitted Ions/Recoils* was checked. This activates the data files for individual ion statistics so that the information about the kinetics of every Transmitted ion are recorded.

5.2 How TRIM Transports Ions in Matter

Ions in TRIM are transported following the Bethe-Bloch stopping power formula:

$$-\frac{dE}{dx} = \frac{kZ_2}{\beta^2} Z_1^2 \left[L_0(\beta) + Z_1 L_1(\beta) + Z_1^2 L_2(\beta) \right] \tag{5.2.1}$$

where k is a constant multiplication factor defined as $k = \frac{4\pi e^4}{m_e c^2}$, where e is the charge of an electron, m_e is the mass of an electron and c is the velocity of light. While $\beta = \frac{v}{c}$ is the relativistic particle velocity where v is the particle velocity, Z_2 is the target atomic number and Z_1 is the particle charge. The latter function between square brackets is also called the *Stopping Number* $L(\beta)$. This term will contain all the corrections of the basic two-particle energy process. The L_0 term contains all the corrections factors of the *Fano* formulation (Equation 5.2.2). The second term L_1 usually called the *Barkas Correction* and the third term L_2 called *the Bloch Correction* will be discussed later in this section.

$$L_0 = \ln \frac{2m_e c^2 \beta^2}{1-\beta^2} - \beta^2 - \frac{C}{Z_2} - \ln\langle I \rangle - \frac{\delta}{2} \tag{5.2.2}$$

C/Z_2 is the *shell correction* for the target atom, $\langle I \rangle$ is the *mean ionization energy* of the target atom and $\delta/2$ is the *density effect correction*..

The Primary Stopping Number, L_0

The stopping number term, L_0, contains the largest corrections to the basic high-energy stopping power formula. The Shell and mean ionization corrections have been evaluated empirically as a single term by rearranging Equation 5.2.1:

$$\ln\langle I\rangle + \frac{C}{Z_2} = \ln\frac{2m_e c^2\beta^2}{1-\beta^2} - \beta^2 - \frac{S_{exp}\beta^2}{kZ_2Z_1^2} - \frac{\delta}{2} + Z_1L_1 + Z_1^2L_2 \tag{5.2.3}$$

where S_{exp} is the experimentally measured electronic stopping power. This approach has the advantage of isolating the two factors in the Bethe-Bloch equation which require extensive theoretical models. The importance of this approach is for the interpolation of stopping powers to targets with little experimental data. If the summed terms could be directly obtained from experimental data, then these can be used to interpolate for stopping powers of similar targets without experimental data. This technique was fist used by Ziegler to extract the summed correction terms in order to normalize stopping calculations for targets without data, or to extrapolate to energies without experimental data [54].

In Figure 5.2 The upper graph shows experimental data for the stopping of H ions in a target of silver, Ag(47), from 26 papers. The data has been reduced using Eq. 5.2.3, so the plot indicates the summed terms of $\ln\langle I\rangle + \frac{C}{Z_2}$ as a function of ion energy, MeV/u. The curved line shows the summed corrections, while the straight line indicates the calculated value of $\langle I\rangle$= 351 eV, using the *Local Density Approximation*. The value of <I> can be empirically determined by moving the curve vertically until it fits the data. The lower figure shows the summed corrections adjusted by increasing the fitted value of $\langle I\rangle$ to 491 eV from the original 351 eV. The theoretical curve agrees well with the data, and can be used to extrapolate to higher energies with confidence. The line called "1% Stopping" in Figure 5.2 is the amount that shell and mean ionization corrections modify the basic Bethe-Bloch stopping power. At 10 MeV/u, the shell correction modifies the stopping power by about 6%, while at 100 MeV/u the correction is 1% .

Before moving on with higher order correction the last term in Eq. (5.2.2), $\frac{\delta}{2}$, is the density effect correction. This is important when the kinetic energy of the particle exceeds its rest mass. Therefore it is way out the interesting range of energies for the simulations that were done. Anyhow this term is also complicated to calculate since it involves the dielectric constant of the material and there is no simple relationship between its magnitude and the target atomic number. In general this correction is larger in lighter atoms,

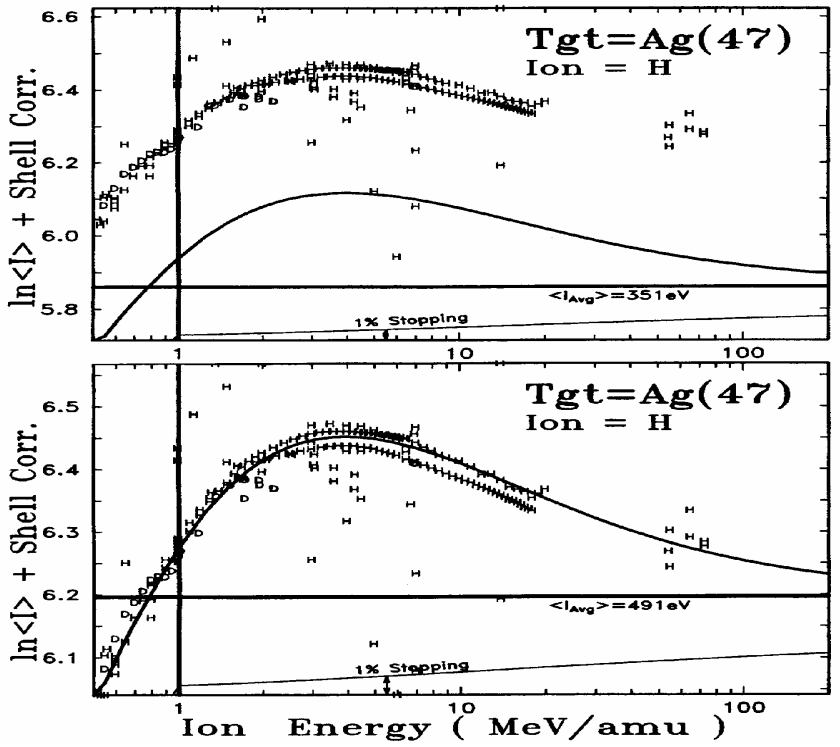

Figure 5.2: $\ln\langle I\rangle + \frac{C}{Z_2}$ Corrections for Ag. (from [55])

while gas targets have no density correction [55].

The Barkas Correction, L_1

If the shell and mean ionization corrections for particles heavier than protons must be calculate, the Barkas correction term and possible neutralization of the particle have to be considered, as in Figure 5.3. This high order correction term was stimulated by two kinds of experimental evidences which highlighted inadequacies in the Bethe-Bloch equation. The first evidence was the discovery of different ranges for particles at the same velocity and in the same target, whose only difference was that one had a positive charge and the other had a negative charge. This was a shocking result, since the Bethe-Bloch stopping power dependence from the particles charge is proportional to Z_1^2. Therefore there should be no difference between positive or negative charged particles. Another experimental evidence showed errors in the scaling of stopping powers for particles at the same velocity and in the same target, whose only difference was the amount of charge. Accordingly to the Bethe-Bloch equation, a particle with charge +2 should have four times the stopping

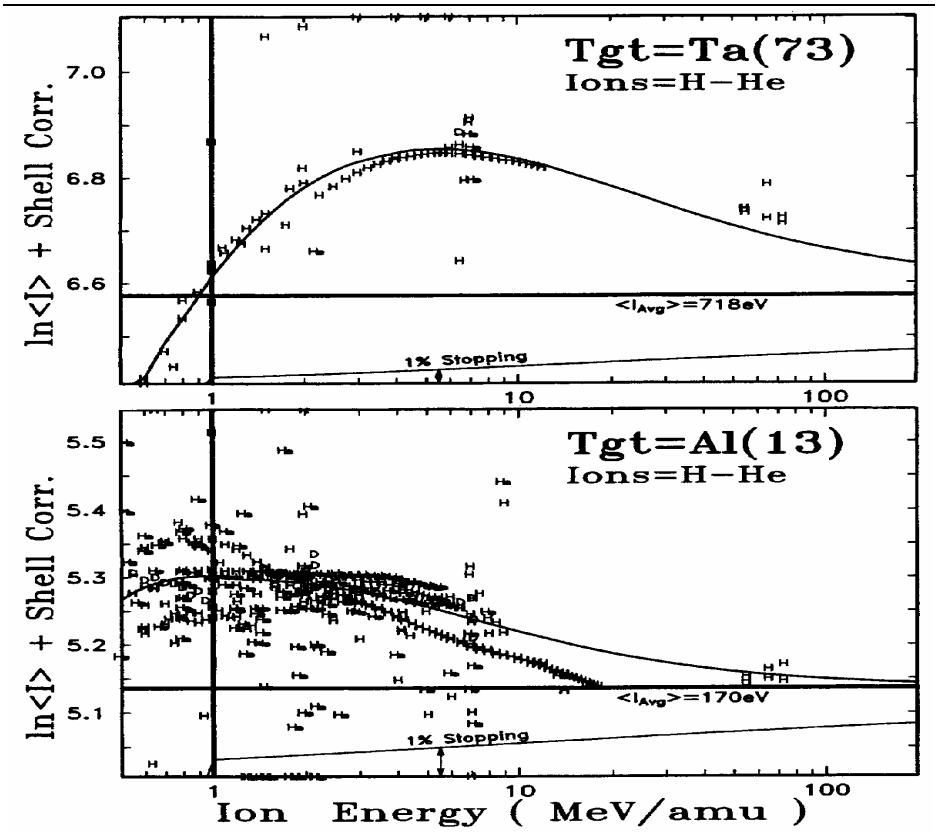

Figure 5.3: $\ln\langle I\rangle + \frac{C}{Z_2}$ Corrections with both H and He for Ta(73) and Al(13). If needed, it is possible to include experimental data from heavier ions than H in order to establish an empirical value of $\langle I\rangle$. The figures shows experimental data for the stopping of both H and He ions in a target of tantalum, upper figure, and in aluminum, lower figure, in a manner similar to that in Figure 5.2. The data has been reduced using Eq. 5.2.3, so the plot indicates the summed terms of $\ln\langle I\rangle + \frac{C}{Z_2}$ as a function of ion energy, MeV/u. (from [55])

of a similar particle with charge +1. However, the stopping of +2 charged particles was discovered to exceed the one expected.

Thus the Barkas effect depends on the charge sign and charge magnitude of the particle. The sign difference was suggested by Barkas. Positive projectiles tend to pull electrons towards their trajectory, while negative particles tend to repel them. This effect becomes apparent near the maximum of the energy loss (about 1MeV/amu fow light particles), while their negligible at high velocities, since the target electrons do not have the time to move. Concerning the charge magnitude effect, particles with a higher charge will pass through a slightly higher density of target electrons compared to singly charged particles, and the stopping power is higher than expected. The Barkas effect is important for low energies. It is caused by target electrons responding to the approaching particle, and slightly changing their orbits before any energy loss interaction occurs. Anyhow for energies $\ll$1 MeV/u, the Barkas effect is difficult to isolate in experiments because of the onset of neutralization of the ion. That is, at low velocities (about 0.6 MeV/u) the ion will begin to pick up electrons which will cause it's charge to be partially shielded, causing any target polarization effects to be overshadowed by more dominant changes in the particle/target interaction. In conclusion, the Barkas correction may be calculated using a large database of experiments. The experimental stopping power may be reduced using Eq. 5.2.4 to extract the Barkas correction for every element with data.

$$Z_1 L_1(\beta) = \frac{S_{exp}\beta^2}{k Z_2 Z_1^2} - L_0(\beta) - Z_1^2 L_2 \tag{5.2.4}$$

Otherwise the Barkas correction term, $Z_1 L_1$ may be estimated using:

$$Z_1 L_1 = \frac{L_{low} L_{high}}{L_{low} + L_{high}} \tag{5.2.5}$$

where $L_{low} = 0.001E$ and $L_{high} = \left(1.5/E^{0.4}\right) + 4500E^{1.6}/Z_2$

The Bloch Correction, L_2

The Bloch term arises from the separation of the impact parameter into two regions. For small impact parameters, Bloch considered the interaction to be that of free particles, as Bohr had done before. However, for large impact parameters, he showed that high-order terms were also necessary, in particular the Z_1^4 term. The correction is more important at high particle velocities, while at low velocities the Bloch correction provides the transition

to the classical stopping power formula. Bitchsel has proposed a simple parametrization of the Bloch correction which accurately fits a wide range of high velocity stopping data:

$$Z_1^2 L_2 = y^2 \left[1.202 - y^2 \left(1.042 - 0.855 y^2 + 0.343 y^4\right)\right] \tag{5.2.6}$$

where $y = Z_1 \alpha / \beta$ and $\alpha = 1/137$.

Low Velocity Limit of the Bethe-Bloch Theory

At low velocities, the particle may capture electrons from the target and partially neutralize its nuclear charge. The Bethe-Bloch equation, in all its forms, requires a constant particle charge. Thus a lower limit to its applicability is necessary. Bohr suggested that the electron orbital velocities would be the critical parameter. Later evidence supported the Bohr view that one could estimate the particle's charge neutralization by assuming it to be stripped of all electrons whose classical orbital velocities were less than the ion velocity. This concept was later formalized form by Northcliffe as:

$$\frac{Z_1^*}{Z_1} = 1 - exp\left[\frac{-v_1}{v_0 Z^{2/3}}\right] \tag{5.2.7}$$

where Z_1^* is the statistical net charge on the partially neutralized ion. At high velocities, $Z_1^* / Z_1 = 1$ when the ion is fully stripped. This expression is useful in the analysis of heavy ion stopping data, but it is not considered accurate for low mass ions. The term statistical net charge (or effective charge) is sometimes defined as the charge state required to reduce the calculated Bethe-Bloch stopping to the experimental stopping values. The implication is that it accounts for the partial neutralization of some of the ions, or it compensates for polarization of the target electrons. Clearly, a proton cannot have a charge of 0.9 units. But this value can reduce, measured low velocity proton stopping powers, averaged over many protons, to the calculated value because of partial neutralization of some of the protons. However, a more reasonable interpretation is that the Bethe-Bloch theory is being used beyond its limits, and that this term is just a fitting parameter.

Accuracy of the stopping power theory

In Figure 5.4 the various contributions towards the stopping of protons in aluminum are plotted. All contributions are shown as a percentage of the total stopping number, L. The contribution ordinate exceeds 100% because some of the terms are negative. The primary

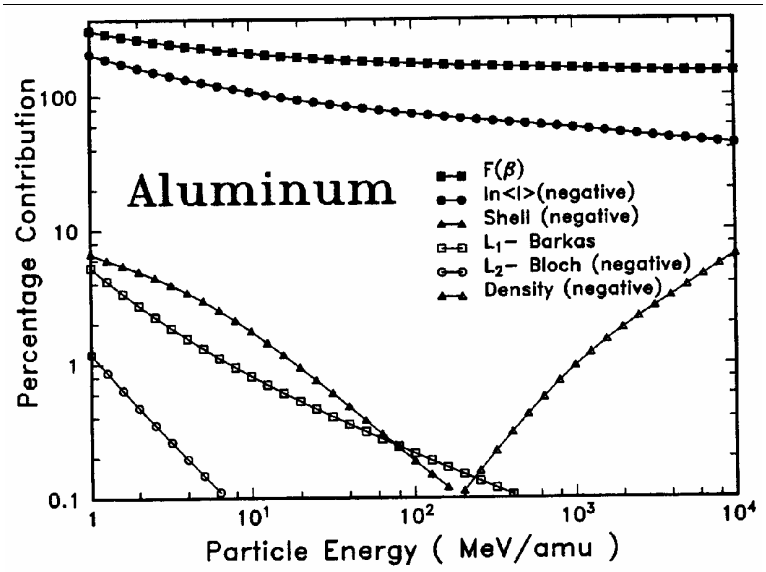

Figure 5.4: Contribution of various stopping corrections for AL(13).

stopping contribution arise from the original Bethe-Bloch equation (where the Barkas and Bloch corrections were non considered), where $F(\beta)$ is:

$$F(\beta) = \ln \frac{2m_e c^2 \beta^2}{1-\beta^2} \tag{5.2.8}$$

The correction terms which are important to low energy stopping are the shell correction, C/Z_2, the Barkas correction, L_1, and the Bloch correction, L_2. The Bloch correction contributes less than 1% to the stopping at all energies. For very high energies, the only significant correction term is the density correction, $\delta/2$, which contributes less than 1% for energies below 1 GeV/u.

What can be seen in Figure 5.4 is that all the corrections to the original Bethe-Bloch formula are theoretical concepts corrected to fit experimental data. Thus a question might arise about, How accurately the stopping powers can be calculated. In Figure 5.5 the experimental/calculated values for the stopping of He ions in nickel targets are shown. There is a significant spread of experimental data beyond the 1% accuracy. For nickel targets, data from 30 papers shows agreement only to about ±3%. However, this spread may be due to different experimental conditions. Studies have shown that metal films prepared by different methods (rolling, evaporation, sputtering, etc.) may have significantly different texture, which is defined as the degree to which the crystalline grains are aligned along a common axis. Hence, some of the observed variation in stopping powers may actually

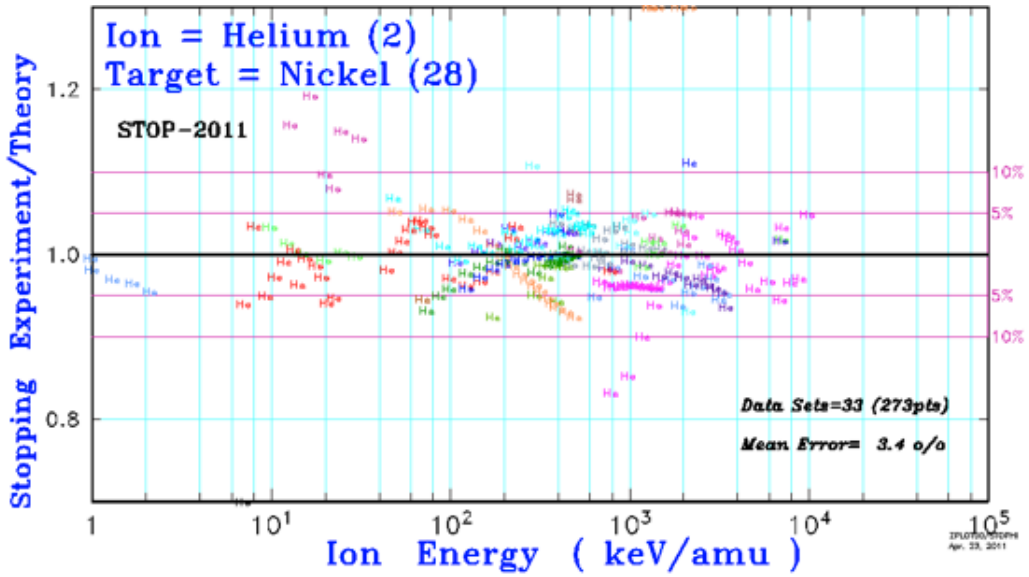

Figure 5.5: Calculated Accuracy for the stopping of He ions in nickel.

be "real", i. e. due to structural differences in the targets and not just due to experimental errors.

Finally, it should be emphasized that chemical binding effects (usually called CBE) and physical state effects (PSE) are well know to cause changes in stopping powers. For water targets in gaseous vs. solid targets, the PSE can reach 30% for low energy light ions, < 50 keV/amu. These effects are estimated to change stopping powers by less than 1% for ions with energies above 10 MeV/amu. For energies from 1-10 MeV/amu, both CBE and PSE may cause a few percent change in stopping powers, especially for light target atoms, Z_2 < 10.

The Stopping and Range in Compounds

An easy way to calculate stopping power in compounds is the *Bragg Rule*, that allow estimating it by linear combination of the stopping powers of the individual elements [50]. The accuracy of Bragg's rule is limited because the energy loss to the electrons in any material depends on the detailed orbital and excitation structure of the matter, and any differences between elemental materials and the same atoms in compounds will cause Bragg's rule to become inaccurate. Further, any bonding changes may also alter the charge state of the ion, thus changing the strength of its interaction with the target medium.

Other approaches have been introduced to estimate the stopping power in compounds,

one of those is the Core and Bond approach (CAB). The CAB suggested that stopping powers in compounds can be predicted using the superposition of stopping by atomic "cores" and then adding the stopping due to the bonding electrons. The core stopping power could be easily calculated following the Bragg's rule, while the chemical bonds would consider the correction of the compound stopping power. The correction from the bonding electrons depend on the chemical nature of the compound. As an example, hydrocarbons could have single, double and triple bonds between two carbon atoms. Each of this bonds contribute to the stopping power in a different way, as show in Figure 5.6.

SRIM uses this approach to generate corrections between Bragg's rule and compounds containing the common elements in compounds: H, C, N, O, F, S and Cl. These light atoms have the largest bonding effect on stopping powers. Heavier atoms are assumed not to contribute to stopping because of their bonds. The Compound Dictionary in TRIM contains the chemical bonding information for about 150 common compounds. The CAB approach that SRIM uses has been tested on more than 100 compounds, from 162 experiments. SRIM correctly predicts the stopping of H and He ions in compounds with an accuracy of better than 2% at the peak of the stopping curve, ≈125 keV/u. Finally, for compounds with heavy target elements, SRIM simply uses the Bragg Rule to calculate the stopping power, as shown in Figure 5.8.

5.3 The TRIM.DAT file

In the Section 5.1 the TRIM.DAT file has been introduced as necessary to simulate ions with various energies, with various angles of incidence and possibly starting at various depths. In this section there will be a description of the file layout and an illustration of the Monte-Carlo code used to generate it.

Figure 5.9 explains all the characteristics of the TRIM.DAT file. The first ten lines are comment lines, while line 8 is a description of the TRIM simulation which will be written in the output file. After the 10 comment lines there are the input data, grouped in 9 columns every line. The first column is reserved for the event name, which must be five characters long. Following the name, there is the atomic number of the transported ion during the TRIM calculation followed by the energy expressed in eV. The next three values give the position inside the previously defined layer in ångström. While the last three are the direction cosines, which define the initial momentum vector of the simulated Ion.

The generation of the TRIM.DAT file can be easily achieved by using a Monte-Carlo

Stopping due to atomic CORES :

Target Atom	Stopping Power
H	0.000
C	6.145
N	5.859
O	5.446
F	5.431
S	32.735
Cl	28.795

Stopping due to atomic BONDS :

Hydrogen Bonds		Carbon Bonds		Other Bonds	
(H-H)	9.590	(C-C)	3.938	(N ≡ N)	20.380
(H-C)	7.224	(C=C)	9.790	(N-O)	15.796
(H-N)	8.244	(C ≡C)	15.022	(O=O)	21.290
(H-O)	8.758	(C-N)	5.080	(S-H)	4.844
		(C-O)	6.168	(S-C)	1.617
		(C=O)	13.926	(S-F)	8.132
		(C-F)	10.998		
		(C-Cl)	3.713		

" ≡ " indicates triple bonds.

Figure 5.6: Core and Bond stopping values. Those are the stopping powers associated with various cores and bonds using stopping units of $\frac{eV}{10^{15} atoms\, cm^2}$.

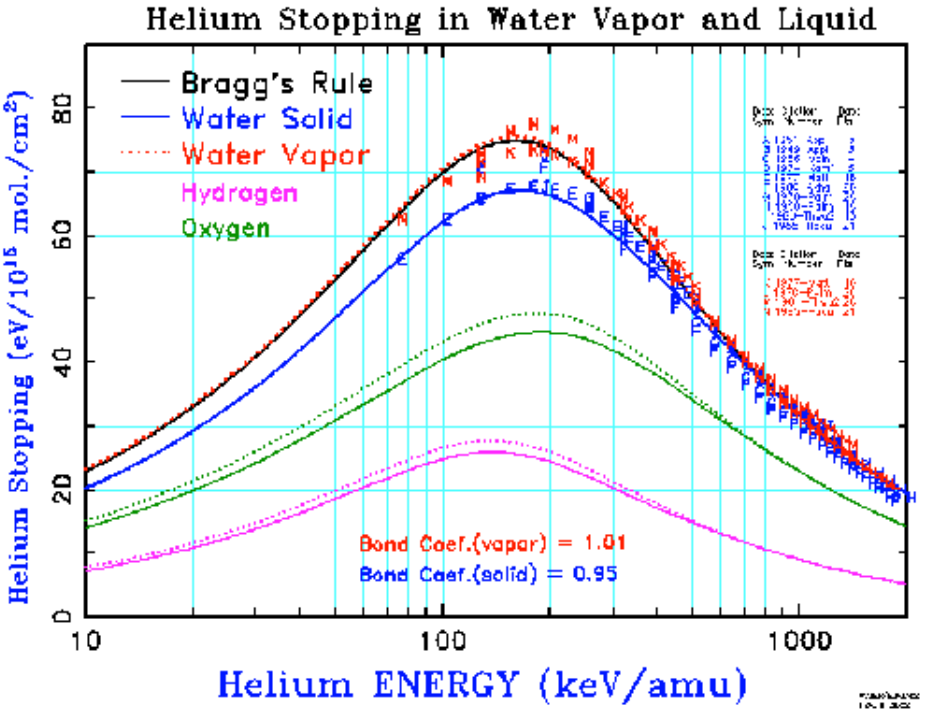

Figure 5.7: The plots shows He ions in water, this data clearly shows the "phase effect" for water in gaseous phase and for water in solid phase. All the solid lines are SRIM calculations for H, O or H_2O in either gaseous or solid state.

Compound	Deviation from Bragg's rule	Compound	Deviation from Bragg's rule	Compound	Deviation from Bragg's rule
Al_2O_3	< 1%	$HfSi_2$	< 2%	Si_3N_4	< 2%
Au-Ag alloys	< 1%	NbC	< 2%	Ta_2O_5	< 1%
Au-Cu alloys	< 2%	NbN	< 2%	TiO_2	< 1 %
$BaCl_2$	< 2%	Nb_2O_5	< 1%	W_2N_3	< 2%
BaF_2	< 2%	RhSi	< 2%	WO_3	< 2%
Fe_2O_3	< 1%	SiC	< 2%	ZnO	< 1%
Fe_3O_4	< 1%				

Figure 5.8: Bragg's Rule Accuracy in Heavy Compounds.

TRIM.DAT: TRIM - various Incident Ion Energies/Angles and Depths

Comment: ***Top 10 lines*** are user comments, with line #8 describing experiment.
Comment: ***Line #8*** will be written into all TRIM output files (various files: *.txt).
Comment: **Data Table** line consist of: EventName(5 char.) + 8 numbers separated by spaces.
Comment: The Event Name consists of any 5 characters to identify that line.
Comment: Typical Data File is shown below, with a variety of numerical formats, all acceptable.
Comment: Note: cos(X) = 1 for normal incidence; cos(X) = -1 for back towards the target surface.

Ar Plasma Ions into Si (1000A thick) (Energies 20-80 keV, Various Angles)

Event	Atom	Energy	Depth	-Lateral-Position-		------- Atom Direction -------		
Name	Numb	(eV)	X (Å)	Y (Å)	Z (Å)	Cos(X)	Cos(Y)	Cos(Z)
A-1	18	12345	0	0	0	1.00000	.000000	-.000000
abcde	18	54321	0	0	0	0.62344	-.295513	.003415
AA#1	18	1.31E4	123	0	-154	0.34234	-.336437	-.017437
C-3	18	123.55	1230	432	12.3E2	-0.23258	-.543453	.443483
AA-1	18	0.123E2	0	-10	-12	0.99998	.000012	-.000017

Figure 5.9: TRIM.DAT - Sample File for Varying Energy/ Angle/ Depth.

code, which defines for each particle (proton, alpha and lithium ions) the energy, the position and the direction cosines. Moreover, to make the simulation more efficient and refined, the ions are extracted following the experimental results of chapter 3

Charged particles transport in the analyzed samples

SRIM was used to transport the charged particles arisen during the neutron irradiation of the liquid and tissue samples to be analyzed by QNCR. The goal is to know the energy and the stopping power of the particles transmitted across the sample and reaching the SSNTD, in order to study the effect of the stopping power on the counted tracks. The transport was simulated in water, because the tissue stopping power is not too different from the stopping power in water, and the results obtained for water can be extended to tissue.

The TRIM.DAT file was created with a ROOT Monte Carlo code written on purpose. This code generates: the atomic number of the transported ion and its energy, the starting position and the direction of the ion. The ions were extracted accordingly with the type of simulation. The simulation calculates the transmitted stopping power distribution of all the particle together (protons, alpha and lithium ions). Accordingly to the experimental neutron fluence and the cross section for neutron capture on boron and nitrogen a defined quantity of protons, alpha and lithium ions are extracted.

Atom	N_{atoms}	σ (barn)	$N_{interactions}$
^{14}N	2.6×10^{18}	1.8	2.4×10^{5}
^{10}B	6×10^{15}	3842	6×10^{5}

Table 5.1: Number of particles that have to be simulated.

After the extraction of the particle, the code generates the particles energy following a uniform distribution of the *Branching Ratio*. The next step is the extraction of the starting position of the particle inside the sample layer. Here the depth of the layer should be carefully selected, it should not be too large otherwise the efficiency of the calculation would be low. Moreover it should not be too small otherwise the "reality" of the simulation would be lost, since the transmitted particles coming from deeper regions inside the sample are not simulated. To choose the proper depth the range of the different ions was considered. The largest range is the one of protons (12 μm). Therefore the code extracts the depth following a uniform distribution going from 0 till 20 μm. While the lateral distribution aims to reproduce the real conditions of the sample irradiation, which has a lateral thickness of 1 cm in both z and y directions, therefore a uniform distribution was selected to generate the y and z points. Finally the direction cosines were generated following a uniform distribution over a spherical surface.

Accordingly to the simulation parameters specified in the above paragraph, the number of ions to simulate was calculated by using the following equation:

$$N_{interactions} = N_{atoms} \cdot \sigma \cdot \Phi \tag{5.3.1}$$

where $N_{interactions}$ are the number of interactions from the neutron capture reaction, N_{atoms} are the number of atoms present in the previously defined volume (2×10^{-3}cm^3), σ is the cross section of the reaction and Φ is the neutron fluence during the irradiation (5.2×10^{10}cm^{-2}). By simulating a sample with 50ppm of ^{10}B and 3% of the total mass composed by ^{14}N, the number of particles that have to be generated are shown in Table (5.1).

In conclusion three TRIM.DAT files were generated, one for each simulated particle type. These files were used to generate a TRIM simulation, where the particles were transported in liquid water. The result of the simulation are stored in an output file, where all the transmitted ions are registered, together with their energy, exit position and flight direction. These data were processed as described in section (5.4).

TRIM output file structure is very similar to the input TRIM.DAT file one. The first 12

lines describe the content of the file and the TRIM simulation. Subsequently the data starts at line 13, here only the particles that are transmitted are stored. The data associated with each particle are in order : Ion Number[1], Atomic Number, Energy in eV, the (x,y,z) position of the transmitted particle and its flight direction specified by the direction cosines.

Comparison between tissue and liquid sample simulations.

For both liquid and tissue samples it is important to compare the experimental and simulation results. Since the atomic composition of the tissue is not known with high precision, the ions were transported in water. This approximation is justified by the fact that the stopping power difference in liquid and tissue is small. To make this comparison the SRIM stopping power tables were used, for the stopping of hydrogen, helium and lithium ions in water and a normal composition of dry tissue [2]. For the purpose of the simulation the stopping power of each transmitted particle is needed. Therefore the SRIM stopping tables for protons, alpha and lithium ions in water were used. A graphical representation of those tables can be seen in Figure (5.10). The selected Stopping Power tables are in the range between 1 eV and 2 MeV. Higher energies are of no interest since the highest energy of the simulated particles is 1.78 MeV of helium ion coming from the neutron capture in boron.

From the calculated stopping power tables, the percentage difference between liquid and tissue can be obtained[3]. Figure (5.11) shows the difference for protons, alpha and lithium ions. As shown, the stopping in tissue for the alpha particles can be up to 11% less than in water for energies around 400 keV. Taking into account that the maximum energy of helium ions is $\approx$ 1.8 MeV, the mean difference in stopping power for this ion is $\approx$ 8 %. This means that the simulation results for the alpha particles in tissue has a relative error of $\approx$ 8 %. The same considerations hold for protons and lithium ions. Figure (5.11) shows that the stopping in tissue is always less than in water, and the difference is $\approx$ 10 % for the protons and $\approx$ 8 % for the lithium ions.

The experimental results have a relative error of $\approx$ 10 %, this means that simulating the tissue like a water sample is a valid approximation for the QNCR working conditions.

[1] The Ion Number specifies to which ion in the TRIM.DAT file the transmitted data corresponds to.

[2] A dry tissue is needed since the sample of tissue dries up when exposed to the air. To obtain its composition a normal muscle tissue defined in the SRIM compound tables was used. Since the loss of weight is known and supposing that all the loss is due to the evaporation of water, the compound stoichiometry has been redefined, obtaining the composition of dry tissue.

[3] To calculate the percentage difference, the stopping power in tissue was subtracted to the stopping power in water and the percentage refers to the stopping in water.

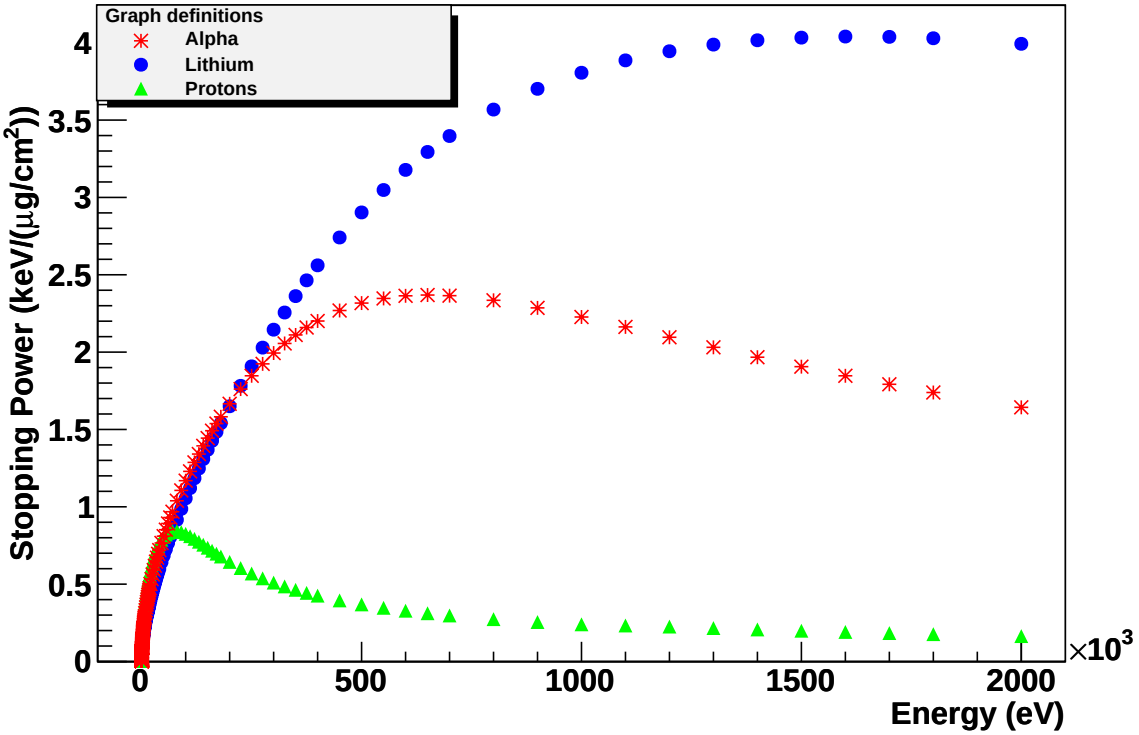

Figure 5.10: The Stopping Power of protons, alpha and lithium ions at variable energies in liquid water.

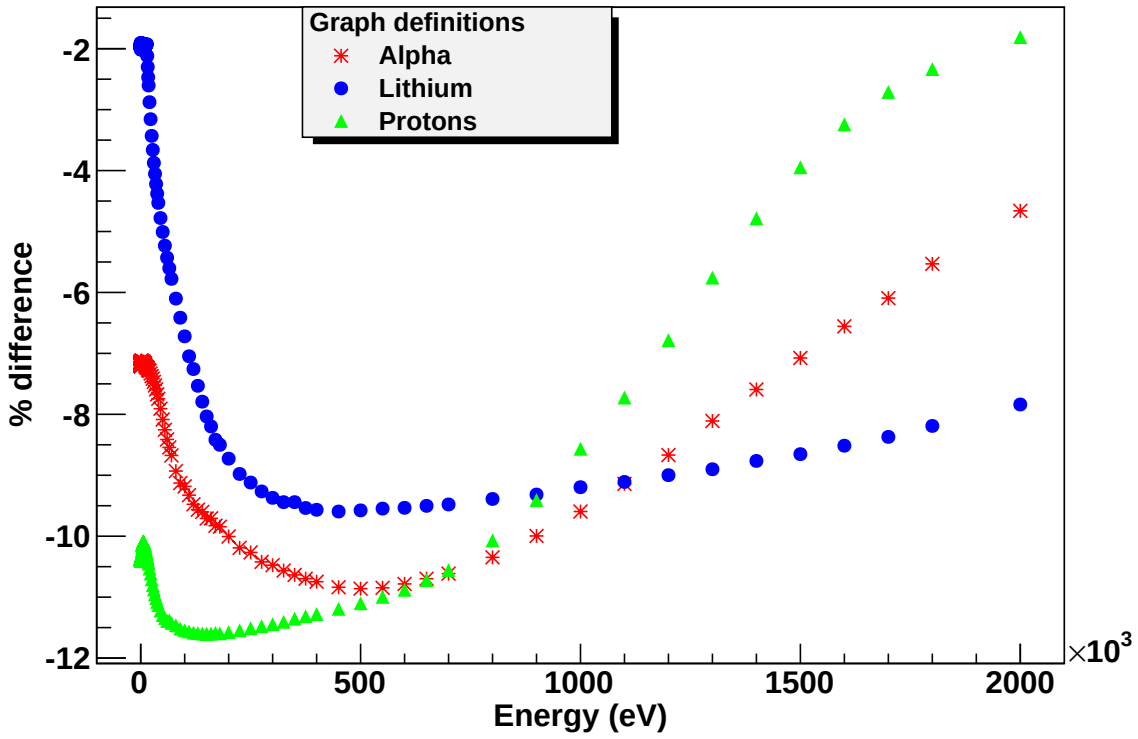

Figure 5.11: Percentage difference between the stopping power in water and dry Tissue.

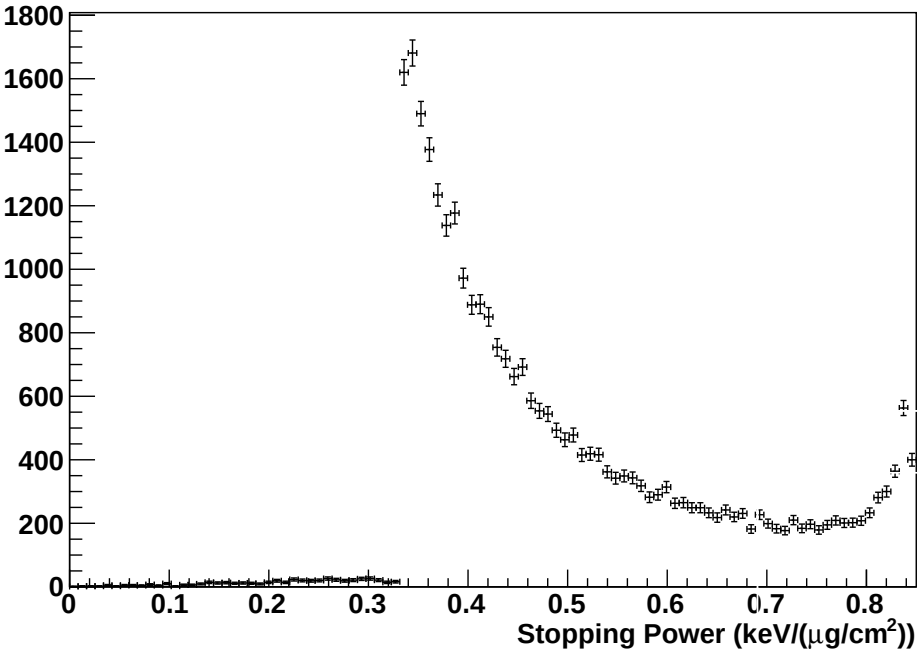

Figure 5.12: The Stopping Power distribution of transmitted protons.

Therefore the results obtained from the transport of ions in water can be used to compare both tissue and liquid data obtained from the experiments.

5.4 Results and conclusion

To analyze the TRIM output files, a C++ program in ROOT environment was created. This code starts with reading the output file and storing in arrays: the energy, the (y,z) position of the transmitted ions and the angle that the flight direction forms with the normal to the y-z plane. The next step is to determine the stopping power of each transmitted particle from its energy. This is achieved by taking two adjacent points in the stopping power table, which defines an energy range. If the transmitted particle energy falls in this range, a linear interpolation of the two stopping power points is taken. From this interpolation the stopping power of the transmitted particle is computed. Finally, the stopping power is stored in an array, where the index of all the generated arrays uniquely defines one transmitted particle. It is then possible to plot the stopping power distribution of the transmitted ions, shown in Figure (5.12) for protons, in Figure (5.13) for alpha particles and in Figure (5.14) for lithium ions.

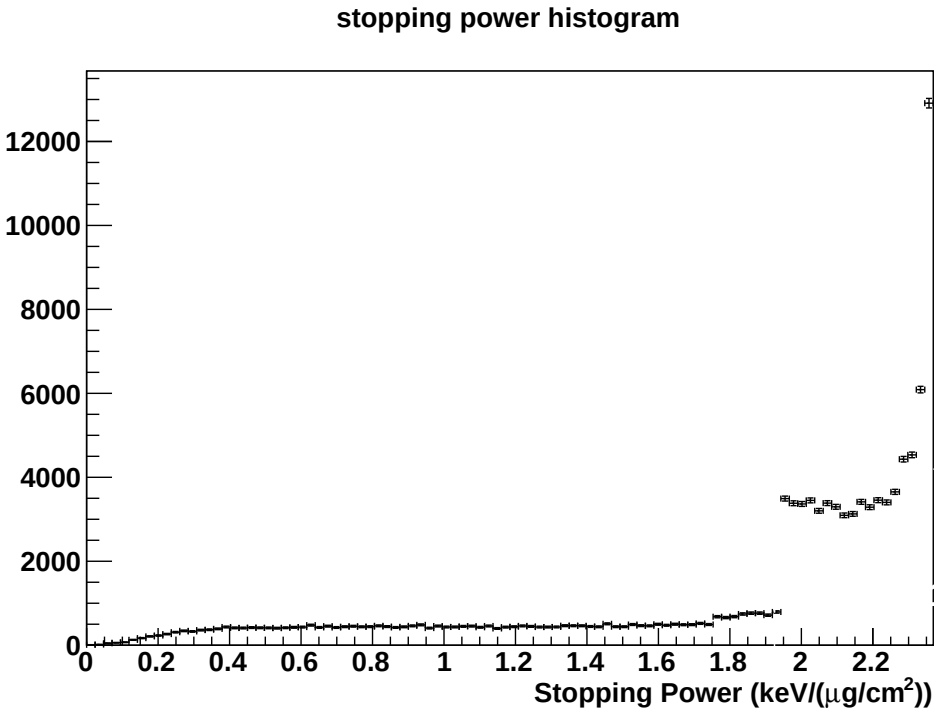

Figure 5.13: The Stopping Power distribution of transmitted alpha particles.

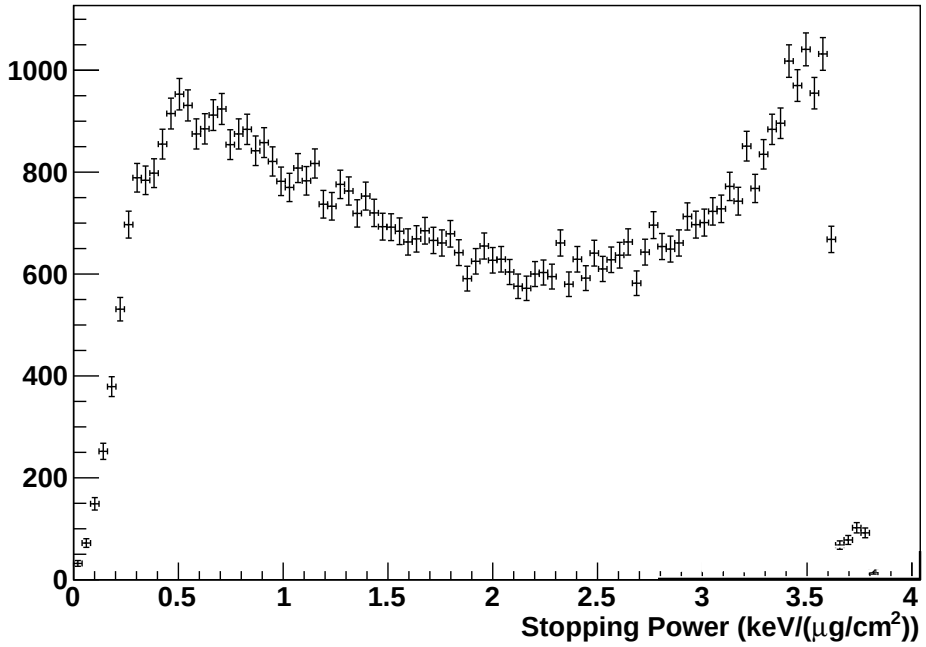

Figure 5.14: The Stopping Power distribution of transmitted lithium particles.

The ion with the highest stopping power is the lithium particle, it is approximately uniformly distributed between 0.5 and 3.5 $keV/(\mu g/cm^2)$. The alpha particles have a peak of stopping power between 2 and 2.3 $keV/(\mu g/cm^2)$, while about 20% of those particles have a stopping less than 2 $keV/(\mu g/cm^2)$. Protons contribute to the stopping power only in the low region, between 0.35 and 0.9 $keV/(\mu g/cm^2)$.

It is interesting to see how the stopping power distributes when all the simulated particles are considered together and to compare this result with the experimental outcomes. For this purpose the tissue and liquid samples with 50 ppm of boron were considered. Figure (5.15) represents the simulated stopping power distribution of the transmitted particles in liquid samples with 50 ppm of boron. Figure (5.16) shows the experimental distribution of the area of the counted tracks. Although the relation between stopping power of the ionizing particle and track evolution is not presently known, there is a correlation between the stopping power of the particle and the area of the track. In particular, the higher is the stopping power of the particle, the larger the track will become. Moreover, comparing the two distribution, it is clear that the response of the SSNTD is not linear with the stopping power of the particle. Although the two histograms have similar behavior, in the simulated stopping power distribution there is an initial plateau before reaching a peak of events followed by another plateau with less events. Anyhow there is a difference in the number of detected events: the number of transmitted particles in the simulation is 42515 ± 210, while the counted tracks in the experimental conditions are 24325 ± 160. This means that ≈ 43 % of the transmitted particles are not detected. This might be due to the critical angle θ_c: particles are detectable when the track etch rate V_t is higher than the bulk etch rate V_b following the relation:

$$V_b < V_t \cos(\theta) \tag{5.4.1}$$

where θ is the angle between the particles trajectory and the bulk etch direction. The critical angle condition corresponds to $V_b = V_t \cos(\theta_c)$. The angle of incidence may not be the only reasons of event loss, the etching removes ≈ 3.3 μm of the SSNTD. As discussed in chapter 3, taking pictures in the same place at different etching time did not evidence any track loss, with etching times up to 240 min. Therefore, the loss given by the etching can be neglected in comparison to the loss given by the angle of incidence of the damaging ionizing particle.

For the 50ppm tissue sample also the proton contribution to the total stopping power distribution must be considered, since 3% of the total mass of an organic sample is com-

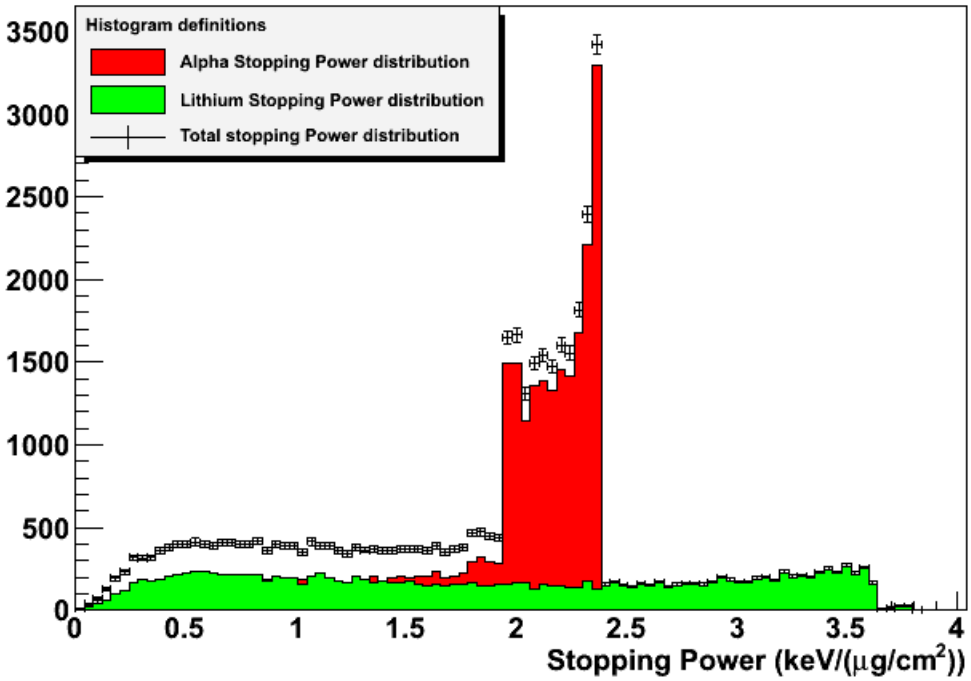

Figure 5.15: The total Stopping Power distribution of transmitted particles in a simulated 50ppm liquid sample. The simulated area is equivalent to 82 pictures of the experimental data.

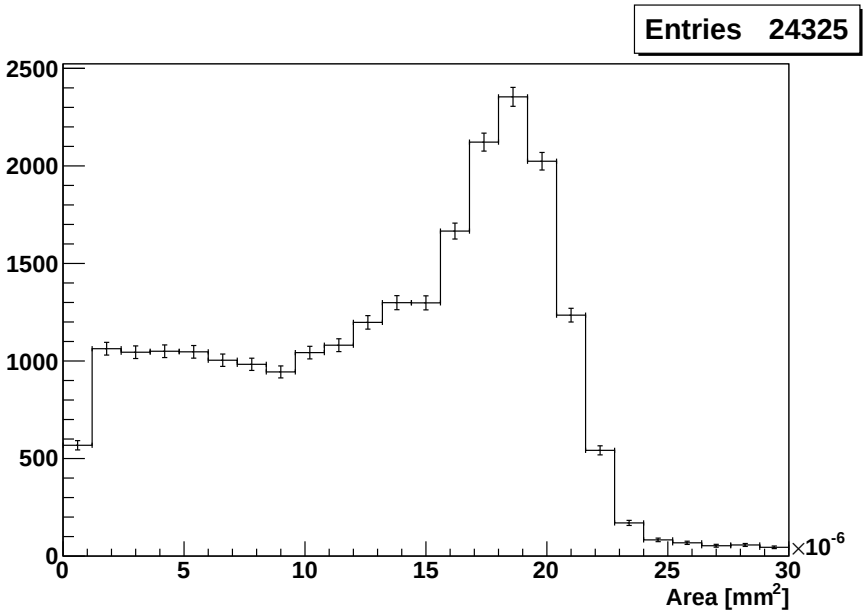

Figure 5.16: The area distribution of counted tracks, coming from 82 pictures of a 50ppm liquid sample.

posed by nitrogen. Figure (5.17) represents the simulated stopping power distribution of the transmitted particles in tissue samples with 50 ppm of boron[4]. The resulting stopping power distribution differs from the liquid sample for the peak at stopping powers between 0.25 and 0.75 $keV/(\mu g/cm^2)$. This difference is due to energy deposition by the protons. The experimental results of the area distribution of the counted tracks can be see in Figure (5.18). As in the case of the liquid samples, there are similarities between the stopping power distribution and the distribution of the track area. Two peaks can be distinguished, one between 1.5 and 3 $\times 10^{-5} mm^2$ which should be given by the contribution of alpha and lithium particles, and the second between 0 and 1 $\times 10^{-5} mm^2$, that should be due to the overlap of protons, lithium and alpha particles tracks. To compare the simulated number of tracks with the experimental tracks, the simulated outcome must be normalized by the corresponding number of pictures and by a calculated fluence used for the simulation, while the experimental value must be normalized over the number of pictures and multiplied by the dry to fresh mass ratio.

As discussed in Chapter 3, the calibration was obtained considering a threshold on the area of the counted tracks. This threshold was set to 1.4 $\times 10^{-5} mm^2$, a value between the two peaks for the tissue samples, and before the high peak in the liquid sample. Comparing these conditions with the simulated ones, the high peak should contain $\approx$ 70 % of alpha particle tracks and $\approx$ 30 % of lithium tracks[5]. For area values below the threshold, the simulations tells that $\approx$ 30 % of the tracks come from lithium ions, another $\approx$ 30 % comes from the alpha particles and $\approx$ 40 % of the tracks are due to protons[6]. To conclude, the simulation of the irradiation conditions demonstrated that the imposed threshold value is a valid method to select only the events coming from the neutron capture in boron. Even more, it showed that for tissue samples there is the possibility to count the number of protons. This can become an interesting parameter, since it could be a way to keep track of the amount of material seen by the SSNTD. This is important when comparing organic materials with different thickness. Till now a mere comparison of the stopping power and area distribution was shown, in the last section an attempt was done to establish the stopping power dependence from the track etch rate, in order to simulate the area distribution

[4]The ions have been transported in water, since the real tissue composition is not known with great accuracy. This approximation is valid up till a few % as discussed in section (5.3).

[5]This result is true for both liquid and tissue samples, since protons contribute to the area distribution only in the low region, $< 10 \times 10^{-4} mm^2$

[6]for the liquid sample this result is different, since there is no contribution to the area distribution by the protons. Therefore in this region 50% of the tracks are given by alpha and an other 50 % are give by lithium ions.

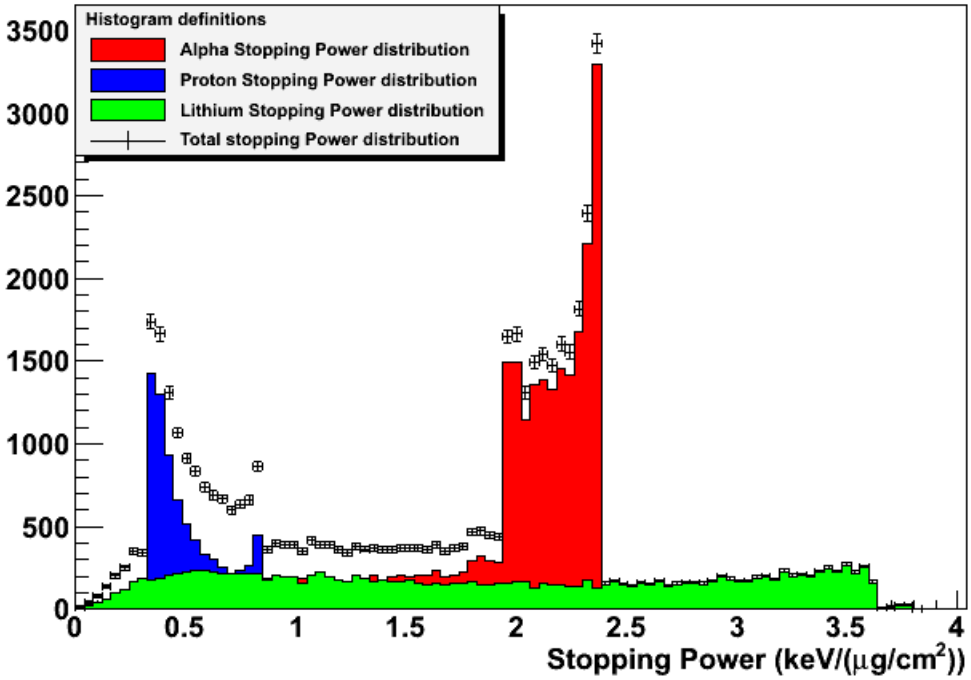

Figure 5.17: The total Stopping Power distribution of transmitted particles in a 50ppm tissue sample. The simulated area is equivalent to 82 pictures of the experimental data.

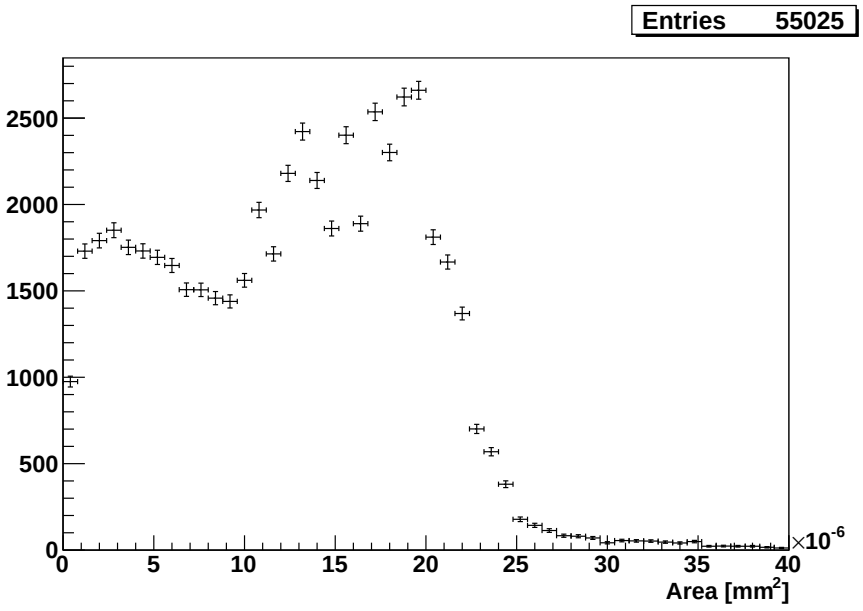

Figure 5.18: The area distribution of counted tracks, coming from 100 pictures of a 50ppm tissue sample.

from the simulated stopping power data.

Track etch rate V_t as a function of the Stopping Power

In literature the stopping power dependence from the track etch rate can be found for high energy ionizing particles [31], while the ions considered for BNCT have energies $\ll$ 1 MeV/amu. This means that the stopping power of those particles can vary along their trajectory, as shown in the previous section. Moreover the angle of incidence of the particles is uniformly distributed along all the solid angle seen by the detector, consequently the tracks on the CR-39 are not perfect circles. Anyhow from the area distribution of the tracks (Figure (5.16)) and the stopping power distribution (Figure (5.15)) for liquids, it can be seen that before the peak at high areas/stopping powers there is a plateau in both histograms. From this observation a relation between the stopping power of the particles and the effect on the CR-39 was extrapolated, knowing that for normal incidence the area A goes as:

$$A = \pi \cdot h^2 \frac{V-1}{V+1} \tag{5.4.2}$$

where h is the amount of etched CR-39 and V is the ratio between the track etch rate and bulk etch rate, as explained in Chapter (1).

The ratio V depends from the stopping power E_s and it is usually expressed as a polynomial expansion of E_s. To obtain this quantity, the experimental area distribution was linearly fitted in the plateau range. The fit parameters were then used to fit the linear range of the stopping power by substituting the area variable of the first fit with Eq. (5.4.2), were V was replaced by a polynomial expansion of E_s, the resulting fitted V equation is:

$$V = 1.4 - 4 \times 10^2 E_s + 7 \times 10^{-4} E_s^2 - 4.6 \times 10^{-7} E_s^3 + 1.1 \times 10^{-8} E_s^4 \tag{5.4.3}$$

By using Eq (5.4.3) the liquid stopping power distribution shown in Figure (5.15) was used to generate the simulated track area distribution, This result is shown in figure (5.19). It can be seen that the experimental and simulated curves are in agreement for the plateau region of the area distribution, while the simulation presents a peak at low areas and an its peak at $2 \times 10{-}5\text{mm}^2$ is higher. This result was obtained using many approximations. Refining the simulation, for example by taking into account a homogeneous angle of incidence and a better parameter for the local energy deposition like the *restricted energy loss*[7] (REL), an accurate dependence of the track etch rate from the stopping power may

[7]The restricted energy loss is a quantity that wants to estimate the amount of energy deposited by the

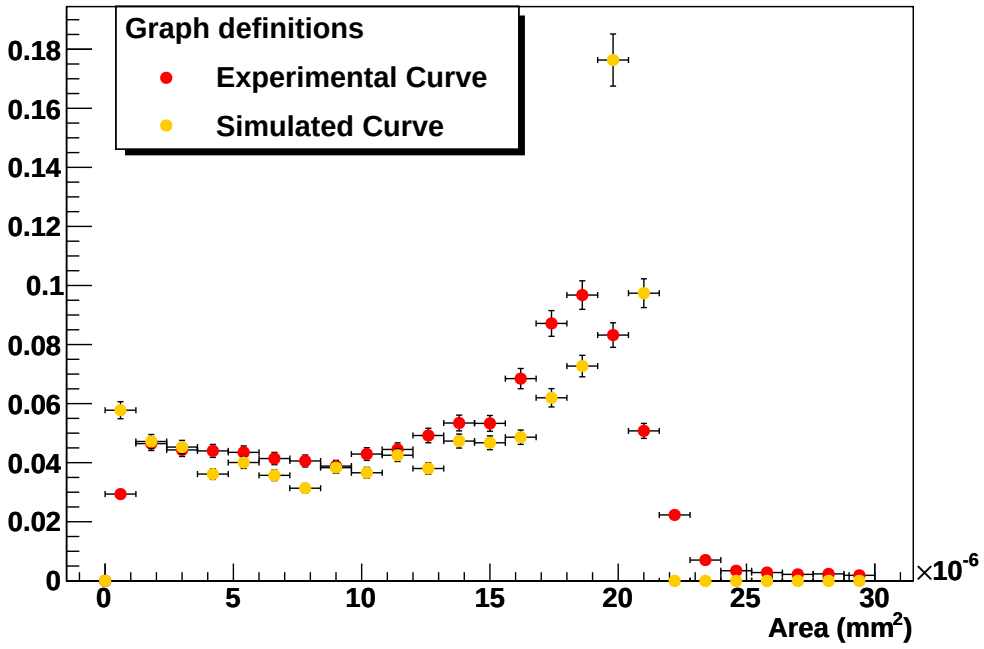

Figure 5.19: Relative number of tracks with a certain area. Comparison between experimental and simulated area distribution.

be calculated.

ionizing particle along the track, therefore not considering δrays that deposit energy far away from the particle. The REL is defined by a threshold value on the transferred energy for a single collision, therefore energy transfers greater that this threshold are not taken into account for the REL evaluation.

Chapter 6

Conclusions

The purpose of this thesis was to provide a method to determine boron concentration in liquid and tissue samples by neutron autoradiography. This technique was optimized by a study of its parameters as the irradiation time and the etching conditions, and it was made more efficient by implementing an automatized system to take the images. The images were analyzed by classifying the tracks according to their area and their radius ratio. The calibration curve obtained using standard samples with known boron concentration is satisfactory since the relative error of the slope is lower than the error affecting the measurement of each sample. Anyhow, the calibration curve for tissue could be further improved by increasing the number of known standard ^{10}B concentration, therefore increasing the number of points and decreasing the error of the fit.

This method was applied to measure cell cultures samples, that had been treated with boron. In particular, UMR-106 Osteosarcoma cells were cultured in presence of BPA and new boronated formulations provided by University of Florence.

In the present work, the autoradiography results were compared to the one of alpha spectrometry, which is another technique for ^{10}B concentration measurement used in Pavia. The results proved that the techniques are in good agreement, supporting that they are both suitable for the determination of boron concentration in biological samples, although liquid samples cannot be measured by spectrometry because they cannot be irradiated under vacuum. A difference between the two techniques lies in the information retrieved: from this point of view, autoradiography is particularly interesting for BNCT because it can determine the micro-distribution of boron in tissues, both in patients and in animal models. In the past few years it has been highlighted that a homogeneous distribution of boron in tissue might play an important role for the positive outcome of BNCT.

Therefore, it is important not only to develop a new drug ensuring higher tumor to tissue boron concentration ratio, but also a low intra-tissue variability of ^{10}B content within the tumor mass and healthy tissue.

To date, no noninvasive online methodology to estimate boron concentration in patients during BNCT has been set-up, apart from PET mediated by fluorinated BPA. This technique has still the limitation that cannot provide precise concentration measurements, but it only gives information on gross boron concentration ratios between tumor and healthy tissues. Thus, the clinical trials are based on the assumption that the tissue boron values for a particular patient can be directly extrapolated from blood boron concentration. Waiting for the development of new in-vivo boron measurement techniques as MRI guided boron imaging, neutron autoradiography allows obtaining more precise results and it could be useful also in clinical BNCT because bioptic samples could be analyzed. On the other hand, also concentration in blood represent an important knowledge for external BNCT irradiation, because neutron capture in boron could damage the blood vessels. For this reason, the autoradiography technique was employed to measure samples of boron mixed with BPA at known concentrations, prepared by forming strips on the CR-39 surface, the result of this first attempt are still under analysis.

Further improvements in the autoradiography could come from a deeper understanding of the energy deposition of the ionizing particles in the SSNTD, in order to gain a better knowledge of the track formation due to particles at energy between 1 keV and 2 MeV. By these means, the histograms of the track area can be connected to the stopping power distribution of the incident ionizing particles, thus refining the separation of protons from lithium ions and alpha particles. This could be achieved by a more performing microscope, which can also be used to increase the resolution of the ^{10}B micro distribution in the tissue samples. An interesting feature of autoradiography is the possibility to develop a technique to calculate the *dose to volume histogram* (DVH) in small volumes of the tread organs, which can be used to compare BNCT with conventional radiotherapy and hadrotherapy. Moreover the autoradiography could be employed for DVH calculation in these sub-volumes, reaching resolutions of $\approx 10^{-2}$ mm^3, which can be interesting for the quantification of micro-metastases around the tumor, particularly important for the application of BNCT on osteosarcoma. A consequence of an improved DVH calculation with autoradiography can be to better interpret the radiobiologic outcome of BNCT.

The preliminary experiments performed in this thesis work, show that osteosarcoma cells uptake boron if exposed to some of the new boronated formulations tested, in particular, the most promising values were obtained with liposomes loaded by LCBO. Further

experiment are needed in order to confirm the observed cell behavior. Neutron autoradiography was proved to be a powerful tool to analyze both liquid and solid biological samples and will be routinely employed by BNCT research group working at University of Pavia.

Bibliography

[1] Wittig A, Michel J, Moss R., Stecher-Rasmussen F., Arlinghaus H., Bendel P., Mauri P., Altieri S., Hilger R., Salvadori P., Menichetti L., Zamenhof R., and Sauerwein W. Boron analysis and boron imaging in biological materials for boron neutron capture therapy (bnct). *Crit Rev Oncol Hematol*, 68, 2008.

[2] S. Altieri, M. Balzi, S. Bortolussi, P. Bruschi, L. Ciani, A. M. Clerici, P. Faraoni, C. Ferrari, M. A. Gadan, L. Panza, D. Pietrangeli, G. Ricciardi, and S. Ristori. Carborane derivaties loaded into liposomes as efficient delivery systems for boron neutron capture therapy. *J. Med. Chem*, 52:7829–7832, 2009.

[3] R. Barillon, M. Fromm, A. Chambaudet, R. Katz, J.P. Stoquert, and A. Pape. Bond scission cross sections for alpha particles in cellulose nitrate. *Radiat. Meas.*, 31:71–75, 1999.

[4] RF Barth, JA Coderre, Vincente MGH, and Blue TE. Boron neutron capture therapy of cancer: current status and future prospects. *Clin Cancer Res*, 11:3987–4002, 2005.

[5] H. Bethe. Zur theorie des durchgangs schneller korpuskularstrahlen durch materie. *Annalen der Physik*, 3:325–400, 1930.

[6] F. Bloch. Bremsvermogen von atomen mit mehreren elektronen. *Zeitshrift fur Physik a Hadrons and nuclei*, 81:363–376, 1933.

[7] N. Bohr. On the constitution of atoms and molecules. i. *Phil. Mag.*, 26:1, 1913.

[8] Silva Bortolussi. *Boron Neutron Capture Therapy of Dissiminated Tumors*. PhD thesis, Universitá degli studi di pavia Dottorato di ricerca in fisica, 2008.

[9] Andrea Braj. Autoradiografia con neutroni applicata alla terapia per cattura neutronica (tcn) di tumori epatici. Master's thesis, Universitá degli studi di Pavia, 1996.

[10] Rovelli C. Effetti della borofenilalanina-fruttosio (bpa-f), agente radiosensibilizzante per la boron neutron capture therapy (bnct), su cellule di astrocitoma umano. *Universitá degli studi di Pavia*, 2010-2011.

[11] B.G. Cartwright, E.K. Shirk, and P.B. Price. A nuclear-track-recording polymer of unique sensitivity and resolution. *Nuclear Instruments and Methods*, 153:457–460, 1978.

[12] Westcott C.H., Walker W.H., and Alexander T.K. Effective cross section and cadmium ratios for the neutron spectra of thermal reactors, proceedings of the international conference on the peaceful uses of atomic energy. *Geneva,1958, P/202 70, USA, New York,*, 1959.

[13] B Cherrier, F Gouin, M-F Heymann, JP Thiery, F Redini, D Heymann, and F Duteille. A new experimental rat model of osteosarcoma established by intrafemoral tumor cell inoculation, useful for biology and therapy investigations. *Tumor Biol*, pages 121–130, 2005.

[14] L. Ciani, S. Bortolussi, S. Altieri, S. Ristori, C. Ferrari, A. Zonta, P. Baglioni, and G. Martini. La boron neutron capture therapy : ricerca e applicazione clinica. *La Chimic e l'Industria*, pages 83–86, 2010.

[15] Chiaraviglio D., Grazia F., Zonta A., Altieri S., Braghieri A., Fossati F., Pedroni P., Pinelli T., Specchairello A., Perlini G., and Rief H. Evaluation of selective boron absorption in liver tumors. *Strahlenther. Onkol.*, 165, 1989.

[16] C. Ferrari, C. Zonta, L. Cansolino, A.M. Clerici, A. Gaspari, S. Altieri, S. Bortolussi, S. Stella, P. Bruschi, P. Dionigi, and A. Zonta. Selective uptake of p-boronophenylalanine by osteosarcoma cells for boron neutron capture therapy. *Applied Radiation and Isotopes*, 67(7-8):341 – 344, 2009.

[17] S Ferrari, Palmerini E, Staals E. L., Mercuri M, Franco B, Picci P, and Bacci G. The treatment of nonmetastatic high grade osteosarcoma of the extremity: Review of the italian rizzoli experience. impact on the future. *Cancer Treatment and Research*, 152:275–287, 2010.

[18] Attix F.H. *Introduction to Radiological Physics and Radiation Dosimetry*. Wiley-VCH, 1986.

[19] R.L. Fleisher, P.B. Prince, and R.M. Walker. Nuclear tracks in solids: principles and applications. *University of California Press*, 1975.

[20] M.A Gadan, S Bortolussi, I Postuma, F Ballarini, P Bruschi, N Protti, D Santoro, S Stella, L Cansolino, A Clerici, C Ferrari, A Zonta, C Zonta, and S Altieri. Set-up and calibration of a method to measure 10b concentration in biological samples by neutron autoradiography. *Nuclear Instruments and Methods*, pages 51–56, 2012.

[21] G.M Gutierrez, E Kong, Y Sabbagh, N.E. Brown, J.S. Lee, M.B. Demay, D.M. Thomas, and P.W. Hinds. Impaired bone development and increased mesenchymal progenitor cells in calvaria of rb1-/- mice. *Proceedings of the National Academy of Sciences of the United States of America*, pages 18402–18407, 2008.

[22] Bruni J. Calcolo del burn-up degli elementi di combustibile del reattore triga mark ii del l.e.n.a. *Universitá degli studi di Pavia*, 2009.

[23] Matthias D. Ziegler James F. Ziegler, Jochen P. Biersack. *SRIM - The Stopping and Range of Ions in Matter*. Pergamon Pr, 2008.

[24] M Klein and G Siegal. Osteosarcoma: Anatomic and histologic variants. *American Journal of Clinical Pathology*, 125:555–581, 2006.

[25] Ciani L. *Liposomes for Gene Delivery and Cell Membranes: a physico-chemical study*. PhD thesis, University of Florence, 2004.

[26] G.L. Locher. Biological effects and therapeutic possibilities of neutrons. *Am. J. Roentgenol. Radium Ther.*, 36:1–13, 1936.

[27] RC Marcove, V Miké, JV Hajek, AG Levin, and RV Hutter. Osteogenic sarcoma under the age of twenty-one a review of one hundred and forty-five operative cases. *J Bone Joint Surg Am.*, 1970.

[28] S Martini, S Ristori, A Pucci, C Bonechi, A Becciolini, G Martini, and C Rossi. Borophenylalanine insertion in cationic liposomes for boron neutron capture therapy. *Biophysical Chemistry*, 111:27–34, 2004.

[29] Jaffe N, Bruland S, and Bielack S. *Pediatric and Adoleschent Osteosarcoma*. Springer, 2009.

[30] S. Nievaart, K. Appelman, F. Stecher-Rasmussen, W. Sauerwein, A. Wittig, and R. Moss. Extension of the calibration curve for the pgra facility in petten. *Applied Radiation and Isotopes*, 67(7, Supplement):S362 – S364, 2009.

[31] D Nikezic and K.N. Yu. Formation and growth of tracks in nuclear track materials. *Material Science and Engineering*, 46:51–123, 2004.

[32] Hundsdoerfer P., Albrecht M, Ruhl U., Fengler R., Kulozik A.E., and Henze G. Long-term outcome after polychemotherapy and intensive local radiation therapy of high-grade osteosarcoma. *European journal of cancer*, 45, 2009.

[33] D. M. Parkin, C. A. Stiller, G. J. Draper, and C. A. Bieber. The international incidence of childhood cancer. *International Journal of Cancer*, 42(4):511–520, 1998.

[34] Piero Picci. Osteosarcoma (osteogenic sarcoma). *Orphanet Journal of Rare Diseases*, page 6, 2007.

[35] J P Pignol, H Oudart, P Chauvel, W Sauerwein, D Gabel, and G Prevot. Selective delivery of 10b to soft tissue sarcoma using 10b-l-borophenylalanine for boron neutron capture therapy. *British Journal of Radiology*, 71:320–323, 1998.

[36] T.U. Probst. Method for born analysis in boron neutron capture therapy (bnct) a review. *Fresenius J Anal Chem*, 364:391–403, 1999.

[37] Brun Rene and Rademakers Fons. Root – an object oriented data analysis framework,. *Proceedings AIHENP'96 Workshop, Lausanne, Sep. 1996, Nucl. Inst. Meth. Phys. Res., See also <http://.root.cern.ch/>*, 1997.

[38] LAG Ries, MA Smith, JG Gurney, M Linet, T Tamra, JL Young, and GR Bunin. *Cancer Incidence and Survival among Children and Adolescents: United States SEER Program 1975-1995*. National Cancer Institute, Bethesda, MD, 1999. SEER Program. NIH Pub. No. 99-4649.

[39] Kent J Riley and Otto K Harling. An improved prompt gamma neutron activation analysis facility using a focused diffracted neutron beam. *Nuclear Instruments and Methods in Physics Research Section B: Beam Interactions with Materials and Atoms*, 143(3):414 – 421, 1998.

[40] Griffith R.V. and Tommasino L. Etch track detectors in radiation dosimetry. *in: K. Kase, B.B. Bjargard, F.H. Attix (Eds.)*, 1991.

[41] Altieri S., Bortolussi S., Bruschi P., Fossati F., Vittor K., Nano R., Facoetti A., Chiari P., Bakeine J., Clerici A., Ferrari C., and Salvucci O. Boron absorption imaging in rat lung colon adenocarcinoma metastases. *J. Phys. Conf. Series*, 41, 2006.

[42] Altieri S., Bortolussi S., Bruschi P., Chiari P., Fossati F., Stella S., Prati U., Roveda L., Zonta A., Zonta C., Ferrari C., Clerici A., Nano R., and Pinelli T. Neutron autoradiography imaging of selective boron uptake in human metastatic tumours. *Appl. Rad. Isotopes*, 66, 2008.

[43] Bortolussi S. and Altieri S. Thermal neutron irradiation field design for boron neutron capture therapy of human explanted liver. *Med. Phys.*, 34, 2007.

[44] Chandra S. Sims ion microscopy as a novel, practical tool for subcellular chemical imaging in cancer research. *Appl. Surf*, 2003.

[45] IB Sivae and VI Bregadze. L-4-boronophenylalanine (all around the one molecule). *J Neurooncol*, pages 49–60, 2008.

[46] A Stiller, C, S Bielack, S, G Jundt, and E Steliarova-Foucher. *Bone Tumours in European children and adolescents, 1978-1997. Report from Automated Childhood Cancer Information System project*, volume 42. 2006.

[47] Tsuboyama T., Tobuchida J., Kotoura Y., Kasahara K., Hiraoka M., and Nakamura T. Intra-operative radiation therapy for osteosarcoma in the extremities. *Int. Orthop.*, 24(4):202–207, 2000.

[48] Josef Uher. 3d neutron detectors. Master's thesis, Mid Sweden University, 2007.

[49] Lothar Weissfloch, Michael Bremer, Peter Lemmen, Thomas Probst, Matthias Wagner, Michael Peller, Thomas Auberger, Reingard Senekowitsch-Schmidtke, Karlheinz Tempel, and Michael Molls. New drugs for bnct: An experimental approach. *Strahlentherapie und Onkologie*, 175:118–120, 1999.

[50] R. Kleeman W.H. Bragg. Xxxix. on the α particles of radium, and their loss of range in passing through various atoms and molecules. *Philosophical Magazine*, 10(57), 1905.

[51] Leo W.R. *Technique for Nuclear and Particle Physics Experiments*. Springer-Verlag, 1994.

[52] T Yamamoto, N Nakai, and A Matsumura. Boron neutron capture therapy for glioblastoma. *J Neurooncol*, 262:143–152, 2008.

[53] D.A. Young. Etching of radiation damage in lithium fluoride. *Nature*, 182:375–7, 1958.

[54] J. F. Ziegler. The stopping of energetic light ions in elemental matter. *J. Appl. Phys / Rev. Appl. Phys.*, 85:1249–1272, 1999.

[55] J.F. Ziegler, J.P. Biersack, and U. Littmark. The stopping and range of ions in solids, 1985. Pergamon Press, Oxford, the code is available on http://www.srim.org.

Acknowledgements

Uscito dalla triennale ero spiazzato, non sapevo che percorso intraprendere. Quindi il primo anno di specialistica l'ho passato cercando e dando poca importanza ai corsi che stavo seguendo. Tutto è cambiato quel giorno quando ho bussato alla porta del gruppo della BNCT a Pavia. Per questo mi sento di dire, grazie Silva e grazie Saverio per avermi accolto subito a braccia aperte; grazie per avermi trasmesso la passione che avete per quello che fate; grazie per avermi dato la voglia di affrontare gli studi con più grinta e dedizione e grazie d'avermi dato la possibilità di sviluppare questa tesi assieme a voi!

Del gruppo BNCT ringrazio le neo dottore Nico e Sabry, per avermi aiutato a risolvere problemi e imprevisti, vi ricordate quella volta che si è rotto il porta campioni con la soda caustica nel bollitore? Un sentito grazie va a Piero Bruschi per i suoi preziosi consigli, e a Francesca per avermi supportato nei momenti di "collera". Ringrazio tutti gli operati del LENA, in particolare Michele per essere sempre stato paziente e per la preziosa acqua distillata, e Daniele per le divertenti comunicazioni a distanza dalla finestra del laboratorio. Inoltre non avrei potuto sviluppare questa tesi senza la collaborazione con il gruppo di Firenze, di cui ringrazio Sandra Ristori e Laura Ciani. Sempre per lo stesso motivo tiro in ballo il gruppo Argentino, Mario e Ruben siete delle persone fantastiche sia al lavoro che fuori, grazie per la vostra disponibilità e simpatia, e un grazie anche a Dr. Agustina in Portu che, con i suoi campioni, ha aiutato a rendere più interessante questa tesi. Non posso poi non ringraziare il gruppo di biologia dell'università di Pavia che ha preparato tutti i campioni cellulari analizzati durante il lavoro che ho svolto, quindi un sentito grazie al gruppo della prof.ssa Cinzia Ferrari. Per finire mi sento di dire grazie anche a Dr. James Bakeine per essere sempre stato disposto a rispondere alle mie domande!

Rimanendo in università un grazie a tutti gli amici che hanno reso il pranzo in cravino una cosa degna d'essere chiamata pranzo. Quindi grazie Claudio per condividere il numero infinito di dolci che porti da ogni angolo del mondo, grazie Ale per le ottime discussioni di qualsiasi genere, e colgo l'occasione per fare gli auguri a te e ad Anna per la

nuova vita che sta arrivando! Grazie AndreaZ (non te la prendere, la Z l'ho aggiunta per distinguere gli omonimi) per essere sempre simpatico e socievole nonostante tu sia interista :p Cosa che non posso dire di Jacopo quando si mette il completo nero-azzurro (calze, mutande, maglietta, guanti, sciarpa...), che tra l'altro non lava dalla lontanissima vittoria della champions. A parte gli scherzi, Jack adoro te e la tua infinita pazienza, in 5 anni non ti ho mai visto alterato, ma guai a toccarti le tartine!!! Poi devo ringraziare la tua morosa CryM (scusa per lo storpiamento) per tutti i bei momenti (anche se pochini) passati assieme. Per finire la carrellata di colleghi universitari saluto anche Fabio e ti prometto che quando sarai orfano di Jack passerò in studio a farti compagnia!

Guido, spero tu sia arrivato a leggere fino a qui, dovrei ringraziarti per così tante cose che potrei scrivere una tesi solo su questo. Ti ringrazio per essere sempre presente quando ho bisogno di te e per i fantastici momenti che abbiamo passato e passeremo, un grazie anche alla tua meravigliosa famiglia: Silvia, Giampaolo e Ciccio. Poi ti ricordi questa estate il tuffo nel mare del nord ? ecco ho sofferto molto e in silenzio :p con la Elo che per infierire faceva delle foto in cui sembravo un ciccio bomba :p a parte questo grazie Elo per gli spassosi momenti che abbiamo condiviso!

Se continuo così finisce che allungo la tesi di altre N pagine quindi ringrazio: i vogheresi Pietro, Buce e Marta; i fisici AndreaF, Sergio e Cesare, gli amanti&biologi Giacomo e Silvia; gli amici di Mirabello Francesca, Eleonora, Valentina, Manuel e Alberto; e per finire anche Rouge, e i miei futuri coinquilini Matteo, Vero e Artina; Grazie per le N birre sorseggiate e gli N aperitivi che abbiamo condiviso.

Un enorme grazie va alla mia famiglia! Grazie mamma per sostenermi in qualsiasi cosa faccio e per essere sempre pronta ad aiutarmi :) Grazie papà per tutto il sostegno che mi hai dato, vorrei vederti più spesso e mi dispiace che siamo sempre separati tu la mamma ed io. Grazie Lele , Vero ,Oscar e Cate perchè è sempre bello stare con voi :) Grazie Zia, Giagia, Baby e Luca perchè Ferriere senza di voi non sarebbe così bello :) Grazie anche a Raffy, Margherita e Jose mi dispiace non venirvi a trovare spesso! Un altro grande grazie va anche alla mia seconda famiglia di Pavia: Anna, Luciano e Bennazza (muahahaha). Een bedankt ook voor mijn Nederlandse familie, Opa & Oma bedankt dat jullie deur altijd voor mij open is.

E poi GRAZIE Cri, per trasformare ogni giorno che passa nel meraviglioso concerto rock che è la nostra vita!!! Ti amo!!!